DRESDNER BEITRÄGE
ZUR SENSORIK

Band 66
Herausgegeben von Gerald Gerlach

Markus Klemm

Acoustic Simulation and Characterization of Capacitive Micromachined Ultrasonic Transducers

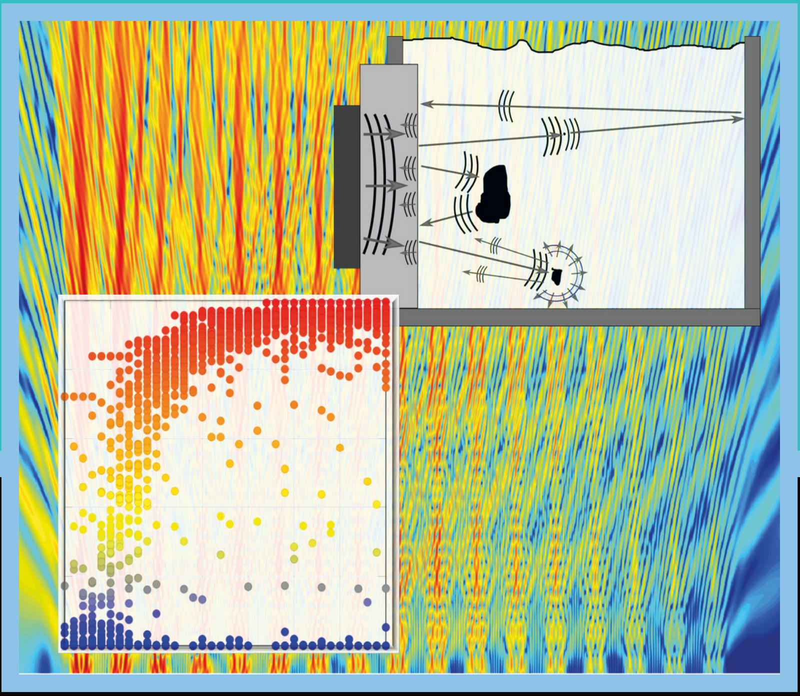

TUDpress

Markus Klemm
Acoustic Simulation and Characterization of Capacitive
Micromachined Ultrasonic Transducers

TUDpress

DRESDNER BEITRÄGE
ZUR SENSORIK

Herausgegeben von
Gerald Gerlach

Band 66

Markus Klemm

Acoustic Simulation and Characterization of Capacitive Micromachined Ultrasonic Transducers

TUD*press*
2017

Die vorliegende Arbeit wurde unter dem Titel „Acoustic Simulation and Characterization of Capacitive Micromachined Ultrasonic Transducers“ am 19.08.2016 als Dissertation an der Fakultät Elektrotechnik und Informationstechnik der Technischen Universität Dresden eingereicht und am 10.04.2017 verteidigt.

Vorsitzender:	Prof. Dr.-Ing. habil. Ercan Altinsoy (TU Dresden)
Gutachter:	Prof. Dr.-Ing. habil. Gerald Gerlach (TU Dresden)
	Prof. Dr. mont. Mario Kupnik (TU Darmstadt)

Bibliografische Information der Deutschen Nationalbibliothek
Die Deutsche Nationalbibliothek verzeichnet diese Publikation in der Deutschen
Nationalbibliografie; detaillierte bibliografische Daten sind im Internet über
http://dnb.d-nb.de abrufbar.

Bibliographic information published by the Deutsche Nationalbibliothek
The Deutsche Nationalbibliothek lists this publication in the Deutsche Nationalbibliografie;
detailed bibliographic data are available in the Internet at http://dnb.d-nb.de.

ISBN 978-3-95908-100-9

Thelem Universitätsverlag &
Buchhandel GmbH & Co. KG
Bergstr. 70 | D-01069 Dresden
Tel.: 0351/47 96 97 20 | Fax: 0351/47 96 08 19
http://www.tudpress.de

TUDpress ist ein Imprint von Thelem.

Gesetzt vom Autor.
Printed in Germany.

Editor’s Preface

Currently, ultrasonic (US) transducers are gaining more and more importance in many fields of technology, in particular in biomedical engineering and non-destructive evaluation. However, they still show some disadvantages. For example, it is difficult to monolithically integrate them with CMOS integrated circuits for control and read-out purposes. They often utilize environmentally unfriendly, lead-containing PZT (lead zirconate titanate) and the fabrication is expensive and complex.

Capacitive micromachined US transducers (CMUTs) seem to be a promising alternative because they can easily be manufactured with silicon CMOS process technology by using sacrificial-layer techniques. By that, it is possible to fabricate US arrays with large numbers of elements. However, even though CMUTs have been proposed already 20 years ago, they could not make the commercial breakthrough yet. Besides the development of appropriate fabrication technologies, this is mainly caused by deficits in the design process, the determination of optimum design parameters and the still lacking wafer-level characterization of CMUT arrays.

This work now turns towards these deficits by analyzing the whole product development process of CMUTs and by developing solutions for critical steps. This regards, for instance, (a) the design, simulation and optimization of CMUT elements, (b) the evaluation of relevant acoustic parameters already in the fabrication process, and (c) the development of an efficient end-of-line test procedure.

In this way, the present work does not only deal with demanding scientific and technological issues but provides important contributions for a possible future commercialization. For that reason, I feel confident that this volume of the book series ‘Dresden Contributions to Sensor Technology’ will earn that amount of kind attention it really deserves.

Dresden, April 2017 Gerald Gerlach

Abstract

In this thesis, simulation and characterization methods for capacitive micromachined ultrasonic transducers (CMUT) useable for application development are shown. A nonlinear simulation model for CMUT cells is implemented, which allows to find the best CMUT design by a genetic optimization procedure. For the verification of fabricated CMUTs against simulation results and specification sheets, acoustic measurement procedures for the characterization of CMUT cell designs are developed. They are based on decoupling the sound field from the individual cell characteristics to measure the send- and receive sensitivity of CMUTs. Another possibility to assess the acoustic characteristics is the electrical impedance measurement. A nonlinear analytic model for the electrical impedance of CMUT is invented and used for design evaluation. A wafer level test procedure for an end-of-line quality assurance based on electrical impedance measurements closes the loop from simulation to fabricated CMUT. The thesis finished with further ideas for improving the CMUT technology and measurement procedures.

Contents

List of Symbols

Symbol	Unit	Description
A	m^2	Area (of the free standing plate)
a_c	m	CMUT cell diameter
a_s	m	Edge length of squared CMUT plate
B	Hz	Bandwidth
c	$\mathrm{m/s}$	Speed of sound
C_{CMUT}	F	Capacity between the CMUT electrodes
C_p	F	Parasitic capacity
D	$\mathrm{N\,m}^2$	Flexural rigidity
d_g	m	CMUT gap height (excluding insulation layers)
D_p	m	Length of a one dimensional piston
d_p	m	CMUT plate thickness
D_A	-	Damping coefficient
d_{eff}	m	Effective gap height (including insulation layers)
E	Pa	Young’s modulus
F	N	Electrostatic or mechanical force
f_0	Hz	Eigenfrequency of CMUT plate without load
f_{-6dB}	$\mathrm{m/s}$	-6 dB cut-off frequency of a signal
f_m	$\mathrm{m/s}$	Center frequency of the CMUT
f_{O1}, f_{O1}	$\mathrm{m/s}$	Lower and upper frequency for CMUT optimization
GBP	V Hz	Gain bandwidth product
H_r	$\mathrm{V/Pa}$	Receive sensitivity
H_s	$\mathrm{Pa/V}$	Send sensitivity
IL_{sr}	-	Insertion loss between send and receive

i	A	Electrical current
K	N/m	Stiffness
k	1/m	Wavenumber
K_p	-	Sound field correction factor
k_T	-	Electromechanical coupling coefficient
L	-	Amplitude loss matrix
R	-	Radiation matrix
L_a	-	Amplitude loss factor
M	N m	Moment
p	Pa	Sound pressure
q	-	Quality indicator
q_0	m/s^3	Acoustic source strength
$\vec{r}$	m	Distance vector
T	-	Acoustic transfer function
U_s	V	Potential difference between CMUT electrodes
U_{AC}	V	Time-dependent part of the CMUT drive voltage
U_{DC}	V	Static bias voltage applied to the CMUT
U_{PI}	V	Pull-in voltage
v	m/s	Sound velocity
w	m	Normal deflection of the plate
Z	Ω	Electrical impedance
$\mathcal{D}$	N s/m	Damping matrix
$\mathcal{K}$	N/m	Stiffness matrix
$\mathcal{M}$	kg	Mass matrix
ε	-	Absolute permittivity
γ	-	Coherence of two signals
Γ_{el}	-	Elevational directivity
ν	-	Poisson’s ratio
ϱ	kg/m	Mass density
σ	Pa	Mechanic stress
θ_0	°	(Acoustic) opening angle

List of Abbreviations

AC	Alternating current
Al_2O_3	Aluminium(III)oxide
ALD	Atomic layer deposition
ASIC	Application-specific integrated circuit
BvD	Butterworth-van Dyke (equivalent circuit)
CMP	Chemical mechanical polishing
CVD	Chemical vapor deposition
CMUT	Capacitive micromachined ultrasonic transducer
DC	Direct current
DHM	Digital holographic microscopy
DUT	Device under test
FE	Finite element
FEM	Finite element method
FIR	Finite impulse response (filter)
IC	Integrated circuit
IPMS	(Fraunhofer) Institute for Photonic Microsystems
IVUS	Intravascular ultrasound
MEMS	Microelectromechanical system
NDT	Nondestructive testing
PCB	Printed circuit board
PECVD	Plasma-enhanced chemical vapor deposition
PZT	Lead zirconate titanate
SEM	Scanning electron microscopy
SiO_2	Silicon dioxide
SPICE	Simulation program with integrated circuit emphasis
TiAl	Titanium aluminide
WLI	White light lnterferometry

Chapter 1

Introduction

THE development of ultrasonic transducers has over 100 years of history initiated by Paul Langevin in 1914 with the US patent application [CP23]. Langevin described a mechanical pistonphone to generate and a hydrophone to sense ultrasonic waves to detect obstacles under water. Nowadays, the use of ultrasound has become an established technology in various applications in industry and medicine as well as in everyday life. Nondestructive testing (NDT), medical sonography or parking aids are just a few examples for systems based on ultrasonic transducers. The optimal transducer technology and design depends on the specific application case and ranges from large single elements for ultrasonic welding or distance measurement to array transducers including hundreds of individually controllable elements with a total size of less than $1\,\mathrm{mm}^2$ for intravascular ultrasound (IVUS).

The construction of array transducers enables the use of beamforming technologies, which allows to electrically steer and focus the ultrasonic beam generated. This is the basis for ultrasonic image acquisition as it is used in medical sonography or NDT. The attainable spatial resolution is increased by reducing the wavelength of the acoustic waves and at the same time reducing the pitch of the transducers' array pattern.

The fabrication of such devices is challenging. Commonly, they are built from piezo ceramic or piezocomposite materials which require a very high effort in cutting and assembling the individual array elements. With this technology based on piezoelectricity, it is possible to assemble probes for operation frequencies up to $25\,\mathrm{MHz}$ using bulk technology. However, in spite of already being medical sonography probes a mass product and available from several manufacturers, its price is in the range of 10,000 $ per unit [Hit13]. This fact can be transferred to other applications as well.

The development of microelectromechanical systems (MEMS) started in the second half of the 20th century. In the meantime, many commercial MEMS sensors are available and sold as mass products. Honeywell Inc. introduced a MEMS microphone in 1986 [Roy+83], which is further advanced and became a successful MEMS sensor sold by several big suppliers today. A MEMS microphone is a capacitive sensor, which is based on two electrodes facing each other. One of the electrodes is constructed as a thin moveable membrane, which can be deflected quasi-statically by an incident sound pressure wave. The displacement induces a change of the sensor's electrical capacity, which can be converted into a voltage signal.

This principle was adopted by Haller in 1994 with a difference in design of the moveable electrode [HK94]. The idea of actuating the movable electrode in its mechanical eigenmode allows to realize a capacitive micromachined ultrasonic transducer (CMUT). This method of fabricating ultrasonic transducers offers the generation of high-resolution array elements as cheap mass product.

In comparison to transducers based on piezoelectricity, with its 20 years of development, the CMUT technology is still young and waiting for its break-through. Therefore, not only a stable and reliable fabrication technology, but also the efficient acoustic simulation and an advanced (end-of-line) testing of CMUT devices are key factors for the successful commercialization in products. Within this thesis, methods and tools have been developed, which support the full process from an initial CMUT design to an end-of-line check before product delivery. The aim is also to reduce the gap between CMUT manufacturing in an academic research center and line production in a commercial MEMS foundry.

1.1 Structure of this Thesis

The aim of this thesis is the advancing of acoustic simulation and characterization procedures for CMUT, which are essential for product development and fabrication. This comprises three main topics addressed within this dissertation:

1. Design simulation and optimization prior fabrication
2. Acoustic characterization and validation of processed CMUT chips
3. Quality assurance by end-of-line testing in production

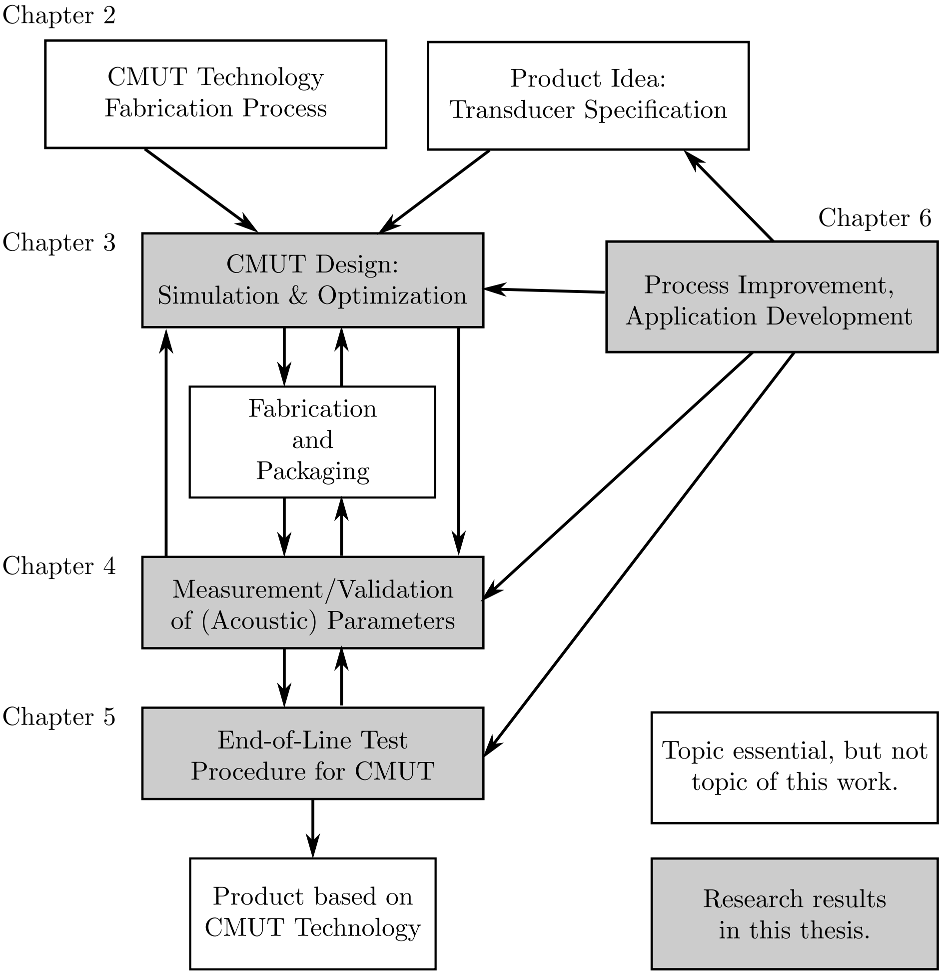

Figure 1.1: General procedure of the CMUT product development process and assignment of contributions within this thesis.

In figure 1.1 these steps are mapped to the full product development process. Before addressing these topics in detail, the thesis concludes chapter one with an overview on the recent state of the art (section 1.2).

In the Chapter 2, a detailed explanation of the operation principle of a CMUT is provided. It describes all effects, which are necessary to understand the content of the further chapters. Additionally, the underlying CMUT fabrication technology is introduced, because all simulations and measurements are performed on CMUTs fabricated in this process.

Chapter 3 briefly explains models for the acoustic simulation of CMUTs and its usability in the CMUT design process. Especially for the desired use-case of finding the best CMUT cell design for a given application and fabrication process, a hybrid simulation model is developed. It allows the nonlinear electro-mechano-acoustic simulation in conjunction with an appropriate optimization algorithm.

The send- and receive sensitivity are identified in chapter 3 as the decisive parameters to describe the transfer characteristics of a CMUT cell. However, no measurement procedure is available for the exact measurement of both parameters for a single CMUT cell (design) independent from the arrangement of multiple CMUTs. Chapter 4 shows a method to separate the send- and receive characteristics of a single cell from the sound field using a correction factor. Based on this approach, measurement procedures and results for the send- and receive sensitivity of CMUTs are shown. Based on the measurement results, suggestions for the optimum drive and receive signals of the analyzed CMUTs are derived. Also, the equality of the CMUTs within a transducer is analyzed based on sound field measurements.

Acoustic measurements (in immersion) allow the determination of the characteristics of a CMUT in an application related manner. However, they are very time-consuming and only applicable if the CMUT is already packaged. Chapter 5 presents a novel nonlinear analytic model for the electrical impedance of CMUT (measured in air), which allows to investigate the characteristics of a CMUT cell and compare its acoustic performance. The model is also utilized to the measurement setup, as the impedance of a CMUT strongly depends on the measurement procedure and parameters. For an end-of-line check in fabrication with the ability to test every CMUT array element, a wafer level test procedure is developed. The result is a quality factor assigned to each CMUT element using a design independent methodology based on a correlation matrix.

In chapter 6, ways to further improve CMUT transducers are demonstrated. They include the construction of mechanically interconnected CMUTs to improve the acoustic performance of individual cells, a novel acoustic test procedure on wafer level, a combination of CMUT and piezoelectric based transducers for using the advantages of both technologies and a CMUT transducer designed especially for acoustic spectroscopy.

Finally, an outlook and a conclusion completes the thesis in the last chapter 7.

1.2 State of the Art

1.2.1 CMUT Technology and Product Development

In 1994, the first functional CMUT device has been presented by the group of Khuri-Yakub in Stanford [HK94] using surface micromachining techniques. The same group also introduced a way of fabricating CMUT by wafer bonding [Yon+03]. Both technologies differ significantly in the fabrication processes and materials used, but result in the same basic type of MEMS structure.

Since the first device has been shown in 1994 [HK94], research activities on CMUT started at many other places in the world. 2D CMUT arrays including a CMOS drive and receive amplifiers form the recent state of the art. In 2013, the team of Khuri-Yakub presented a 32×32 2D CMUT array for volumetric imaging including drive and receive electronics as integrated circuits [Bhu+13]. The CMUTs are fabricated using a sacrificial release process and operate at $5\,\mathrm{MHz}$ center frequency. Researchers at Technical University Denmark in cooperation with BK Medical are recently working on volumetric imaging using row-column-addressed CMUT arrays [Chr+15]. The group of Degertekin from Georgia Tech demonstrated a single-chip CMUT-on-CMOS for volumetric intravascular ultrasound [Gur+14] with two annular CMUT arrays: one with 56 elements for transmit and a second with 48 elements for receive operation.

Besides from academic research, Vermon [Tes+06] and Samsung [Kim+12] are two exemplary companies currently working on CMUT technology. Nevertheless, the step to commercially available products based on CMUT is still to go. Hitachi developed a probe called ‘Mappie’ in 2009 [Hit09]. However, it is not sold on the international market. Hitachi did continue the development and recently announced a novel CMUT probe for cardiovascular use in [Mas15].

In conclusion, CMUT technology has not overcome the gap from research labs to commercial products up to now. The main key steps to bridge this gap are a stable fabrication process in line with efficient CMUT simulation and design tools, end-of-line testing, application-specific packaging, system characterization and electronic development.

1.2.2 Modeling and Simulation

The simulation of the behavior of a CMUT with a given design is essential for a successful transducer fabrication, as the throughput time for a full wafer run can be several months. In addition, a new design goes along with a new set of fabrication masks, which rises material and labor costs. Therefore, the number of prototypes needs to be minimized. This requires the use of simulations prior processing the devices.

In 1994, Haller used Mason's model [Mas58] for a capacitive resonator to describe the first fabricated CMUT cell [HK94]. This linear equivalent circuit model is based on lumped parameters and has been used for piezoelectric plate transducers for decades [Rhy78]. Lohfink presented several improvements of this model especially for CMUT [Loh05]. Within the past ten years, the group of Koymen at Bilkent University further advanced the lumped element circuit models to include the nonlinear characteristics of a CMUT [Köy+07; Köy+12] as well as the interaction of many single CMUT cells within an array. Also, CMUTs in collapsed-mode have been modeled using equivalent circuits [Olc+10].

Starting in 2001, finite element (FE) models have been increasingly used to simulate CMUT transducers. [Bay+01] presented the first FE model to calculate the static displacement of a CMUT plate depending on the electrode size and location. With increasing computing power and the development of FE analysis packages for coupled partial differential equations, CMUT simulation models became more complex and powerful. This inherits multiphysics analysis of electrical, mechanical and acoustical interactions for CMUT. A recent example is published in [Lei+14] investigating the acoustic parameters of a CMUT cell using Comsol. In [Ras+15], the sound field of a row-column-addressed CMUT array is simulated using the software Field II.

However, the simulation of a full sound field generated by many CMUTs and optimization runs in the CMUT design process still require approaches, which are computational less expensive and easier to handle than full 3D FE models. Examples are given by [CTP05], where the plate deflection is derived from a FE model and the sound radiation is represented by the acoustic impedance of a piston. Another lumped model was recently presented by Satir and is based on Matlab/Simulink [SZD13; SD14]. Here, the electrostatic interaction is implemented as look-up table and the mechano-acoustic interaction is solved using a boundary element based method. According to [SD14], this model needs $30\,\mathrm{min}$ to compute the stiffness matrix and then only a few seconds to minutes to simulate the plate bending and sound pressure emission of the CMUT, which makes it still not useable for design optimization runs in a big parameter space.

1.2.3 Measurement and Characterization

The experimental characterization of CMUT can be divided into electrical, mechanical and acoustical methods. They represent the analysis of the electrical input voltage and current, the mechanic displacement of the CMUT plate and the sound pressure radiated into space.

The electrical impedance allows to extract basic information such as resonance frequency and pull in voltage. The open and short circuit resonant frequencies and the electrodynamic coupling coefficient are further parameters derived from the impedance curve. These parameters are adopted from piezo and quartz characterization. Carnonti [CCP03] and Yaralioglu [Yar+03] published approaches, how to denote coupling coefficient k_T to evaluate the efficiency of a CMUT cell design. However, this methodology does not cover the transfer function from the mechanical displacement to the acoustic sound pressure. For a transducer with high impedance (such as PZT bulk transducers) this fact is of less importance. In case of a CMUT, its characteristics alters significantly, when the acoustic impedance of the medium changes. This fact makes a comparison of parameters such as the coupling coefficient k_T measured in air unsuitable for a comparison of immersed CMUT to other transducers or even against different CMUT designs. In conclusion, the measurement of the electrical impedance is state of the art, but not all information available in the impedance curve can be extracted with existing models.

The mechanical characterization is based on optical measurements using white light interferometry (WLI), laser Doppler interferometry (vibrometry) or digital holographic microscopy (DHM) [Sen+09]. These technologies allow to measure the displacement of the CMUT plate statically, dynamically in axial direction and dynamically in 3D. With special lenses, the measurements can also be performed in immersion. A conclusion on the radiated sound pressure is possible by special measurements based on focusing on a thin foil, which is placed in front of the CMUT and moves according to the sound velocity.

Acoustic measurements usually include the investigation of the transducer's sound field. Therefore, a microphone or hydrophone is placed in front of the CMUT transducer and the emitted sound pressure is measured. By scanning the area in front of the CMUT, the sound field of the transducer can be studied [Chr+14; Hof+13]. An important parameter is the send sensitivity, which denotes the fraction between the sound pressure measured in the focus point and the applied AC drive signal. The send sensitivity can be investigated using the sound field scanning setup and is a method to compare the efficiency of different ultrasonic transducers. The measurement of the receive sensitivity is explored less, than the investigation of the send sensitivity. A requisite for quantitative measuring a receive sensitivity is the knowledge of the incident sound pressure at the CMUTs' surface. It is difficult or even impossible to find calibrated transducers which are able to send ultrasonic signals which cover the whole frequency bandwidth of the CMUT [Olc+10]. Still, the receive sensitivity is a parameter, which is valuable in application development and transducer design.

An often ignored point in acoustic measurements is the fact that the attained signals are always created by a large ensemble of CMUT cells transmitting in parallel. The individual CMUT cells are mechanically independent, but affect each other by acoustic crosstalk. However, an even more important fact is, that the sound pressure measured by a hydrophone is the result of a superposition of the sound pressure waves emitted by many individual CMUTs. This means that no clear conclusions on the acoustic parameters of a CMUT cell (design) can be derived, but only on the full ensemble of CMUTs probed.

1.3 Achievements of this Work

The primary objective of this thesis is to develop tools necessary for product development based on CMUT technology. Starting from this premise, the analysis of the state of the art and the availability of a stable fabrication process, the following achievements have been obtained within this work:

- Nonlinear simulation model for design optimization of CMUT cells
  - Simplified but still accurate model to create a numerical CMUT representation (FE) fast (within seconds)
  - Time step integration including an efficient structure-fluid interaction algorithm
  - Genetic optimization run for design optimization of CMUT

- Acoustic measurement procedures for the characterization of CMUT cell designs
  - Procedure for decoupling the sound field from the individual cell characteristics
  - Send sensitivity measurements and recommendations on the optimal drive signal
  - Quantitative receive sensitivity measurement based on pitch catch principle
  - Equality study of array elements by sound field analysis

- Nonlinear analytic model for the electrical impedance of CMUT
  - Nonlinear model based on a factual mechanical representation of a CMUT cell
  - Analysis of the influence of the impedance measurement procedure and measurement parameters on the impedance curve
  - Extraction of acoustic characteristics from the electrical impedance using the new analytic modeling approach

- Wafer level test procedure based on electrical impedance
  - Methodology for quality assessment based on a coherence criterion
  - Procedure for a valid and fast acoustic end-of-line check available for CMUT

Chapter 2

CMUT Operation and Fabrication

2.1 Working Principle of CMUT

2.1.1 Basic Operation

CMUTs are ultrasonic transducers based on a resonant vibrating plate, that can transfer acoustic into electric energy and vice versa. This requires very small structures which can be fabricated using micromachining technology. Thus, CMUTs consist of two electrodes separated by an air or vacuum gap as shown in figure 2.1. One electrode is fixed on the wafer substrate whereas the second electrode is designed as a thin bendable plate. Applying an alternating electrical potential difference U_s between both electrodes creates an time-dependent attractive force between the bottom electrode and the thin plate. This induces a dynamic displacement of the bendable plate and ultrasound is radiated into the adjacent fluid. CMUTs can not only act as acoustic sound source, but also operate as sensor for ultrasound. In this case, incident ultrasonic waves induce a bending of the top plate which leads to a change of the electric capacity of the CMUT cell. The application of a DC bias voltage between both plates leads to a displacement current, when the capacity changes. This current is measured as direct indicator for the sound pressure change at the CMUT's surface.

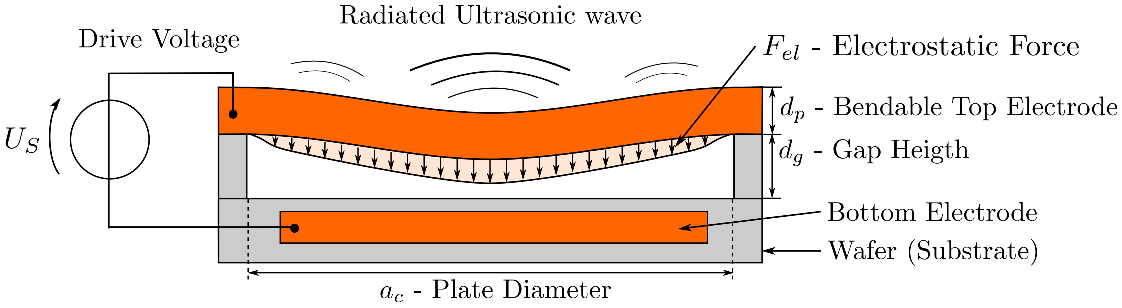

Figure 2.1: Schematic cross section of a CMUT in transmit operation (dimensions not in scale)

2.1.2 Physical Classification of a CMUT

The mechanical structure of a CMUT defines its acoustic characteristics as well as the requirement for subsequent drive and receive circuitry. Therefore, a basic physical model is necessary to understand, simulate CMUTs and compare them to other types of (acoustic) transducers.

The lateral dimension a_c and thickness of the top electrode d_p are the major parameters to define the resonant frequency of the CMUT plate. The gap size d_g has major influence on the capacity of the CMUT and therefore the electrical voltage U_S. Usually, the gap size d_g, the thickness of the top electrode d_p and the lateral dimension a_c of a CMUT cell show the following relation

$$d_g \ll d_p \ll a_c.$$

The scanning electron microscopy (SEM) picture of the cross section of a CMUT cell shown in figure 2.2 conveys an impression of the real dimensions, which are similar for most of the CMUT designs utilized.

Figure 2.2: Scanning electron microscopy (SEM) image of the cross section of a CMUT cell with $a_s = 20$ µm

The maximum deflection of the top electrode w is limited by the gap size d_g. From the geometric dimensions of a CMUT cell, this implies an elastic deformation of the free-standing CMUT plate. To access the main characteristics of the CMUT cell, the top electrode can be considered as bendable plate, which fulfills the Kirchhoff hypotheses [VK01] as shown in table 2.1. This allows to calculate the (static and dynamic) deflection w of the top electrode based on its thickness d_p, mass density ϱ and flexural rigidity at the coordinate $(x, y) \in \mathbb{R}$:

$$D\left(\frac{\partial^4}{\partial x^4} + 2\frac{\partial^4}{\partial x^2 \partial y^2} + \frac{\partial^4}{\partial y^4}\right) w(x,y,t) = \varrho\, d_p\, \frac{\partial^2}{\partial t^2} w(x,y,t). \tag{2.1}$$

Table 2.1: Kirchhoff hypotheses [VK01] applied on the top electrode of a CMUT cell

	HYPOTHESIS	CMUT
1	The plate material is elastic, homogenous and isotropic.	CMUT plates as used here are made from amorphous metal, which meets these requirements.
2	The plate is initially flat.	The plate deflection w due to fabrication inaccuracies amounts less than 1/1000 of the lateral plate dimension a_c.
3	The plate deflection is small compared to the thickness.	The gap height d_g limits the deflection, which is small in comparison to the plate thickness d_p.
4	The vertical shear strains and normal strain is negligible.	After fabrication, no vertical strains or normal strains remain.
5	The stress in the middle plane is negligible.	The stress due to atmospheric pressure does not create a significant strain of the plate.
6	The surface remains unstrained after bending.	Only for very thick CMUT plates in conjunction with a small plate size a_c, shear transformations appear. For all other CMUTs, this hypothesis is fulfilled.

A CMUT is a resonant transducer in both send- and receive operation. This means that the plate is bent in its first eigenmode, where even a small force creates a comparably large dynamic displacement. Based on equation (2.1), the first eigenfrequency f_0 for a clamped circular plate can be calculated analytically [Lei69] and indicates the operation frequency of a circular CMUT cell

$$f_0 = \frac{10.22}{a_d}\sqrt{\frac{D}{\varrho\, d_p}}. \tag{2.2}$$

This operation of CMUTs in its eigenmode distinguishes them for example from MEMS microphones, where the electrode is moved quasi-statically by the incident acoustic signal. In conclusion, a CMUT is a capacitive transducer, which can receive or send ultrasonic signals due to the resonant bending of a plate. This plate can be described by the Kirchhoff–Love plate theory [VK01]. In case of extremely thick, small CMUT plates the Mindlin–Reissner plate theory delivers more accurate results, because also shear transformations are included into this model.

2.1.3 CMUT Transmit and Receive Operation

In the following section, the basic operation principle of a CMUT for sending and receiving ultrasonic waves will be explained.

To use a CMUT as ultrasonic source, an AC drive signal has to be applied between both electrodes. The voltage U_s causes an electrostatic force F_{el} between both electrodes, which can be approximated by assuming both electrodes to represent a plate capacitor. The electrostatic force

$$F_{el} = \frac{\varepsilon A}{2} \frac{U_s^2}{d_g - w_{avg}} \tag{2.3}$$

is proportional to the area of the electrodes A and the permittivity ε of the diaphragm in the gap. d_g represents the initial gap height, and w_{avg} the mean deflection of the top plate towards the bottom electrode.

For CMUTs with a circular shape of a diameter a_c and a flexural rigidity D, the average deflection of the plate w_{avg} can be solved analytical from equation (2.3) [WKK08]:

$$w_{avg} = F_{el} \frac{d_a^2}{192 \pi D}. \tag{2.4}$$

Combining equation (2.3) and (2.4) leads to two important conclusions: The electrostatic force depends on the current deflection of the plate and shows a quadratic relation to the applied drive voltage. Both facts make a CMUT being a nonlinear transducer. This can be counteracted by applying an additional DC voltage U_{DC}:

$$U_s = U_{AC} + U_{DC}. \tag{2.5}$$

Then the electrostatic force becomes

$$F_{el} = \frac{1}{2}\frac{\varepsilon A}{d_g - w_{avg}}\left(U_{AC}^2 + 2U_{AC}U_{DC} + U_{DC}^2\right). \tag{2.6}$$

The DC bias voltage $_{DC}$ has two beneficial effects. It creates an attractive force and hence a static deflection of the plate, which reduces the effective gap. This allows to generate the same dynamic electrostatic force with reduced AC drive signal. Additionally, the AC voltage U_{AC} an electrostatic force is generated, which is proportional to the AC drive voltage. In practice, a bias tee is used for adding the DC voltage to the AC signal as shown in figure 2.3.

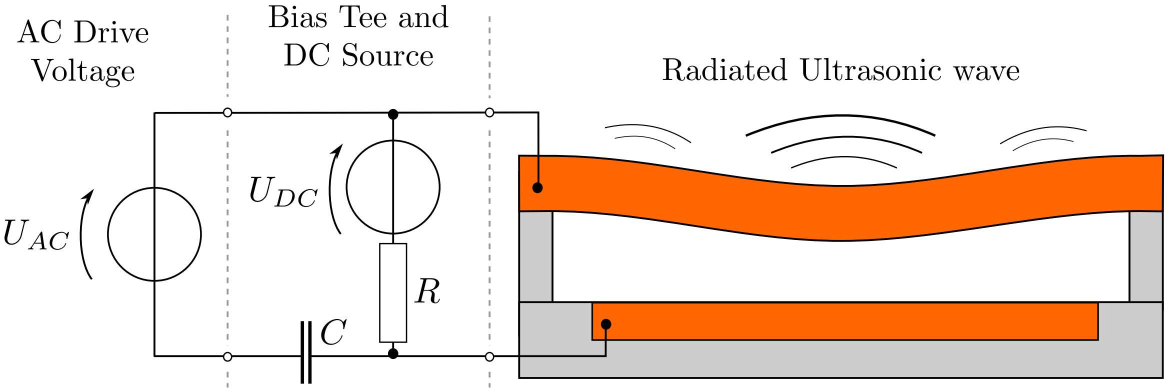

Figure 2.3: Schematic of a CMUT in send operation

In receive operation, an incident ultrasonic wave deflects the CMUT plate. The time-dependent displacement $w_{avg}(t)$ causes a change of the capacity $C_{CMUT}(t)$ between both electrodes:

$$C_{CMUT}(t) = \frac{\varepsilon A}{d_g - w_{avg}(t)}. \tag{2.7}$$

It is not possible to measure the capacity of the CMUT directly. Therefore, a DC bias voltage U_{DC} is applied to the CMUT which creates a displacement current $i_{\Delta C}$, when the capacity of the CMUT C_{CMUT} changes:

$$i_{\Delta C}(t) = U_{DC}\frac{\mathrm{d}C_{CMUT}(t)}{\mathrm{d}t} = U_{DC}\cdot\varepsilon A\frac{\mathrm{d}}{\mathrm{d}t}\frac{1}{d_g - w_{avg}(t)}. \tag{2.8}$$

Additionally, the electrostatic force bends the CMUT plate and decreases the residual gap. This raises the capacity change for the same dynamic displacement.

The displacement current $i_{\Delta C}$ is in direct relation to the dynamic deflection $w_{avg}(t)$ of the CMUT and therefore a direct indicator for the sound pressure at the surface of the CMUT.

Also in receive operation, a CMUT is a nonlinear system with memory, because its output strongly depends on the initial plate deflection and velocity.

The displacement current has to be amplified and converted into a voltage signal, which can be digitized and processed further. In CMOS receive circuits for an already defined CMUT design, a transimpedance amplifier the first choice. This configuration is shown in figure 2.4. Alternatives are linear voltage amplifiers and charge amplifiers. More information about the advantages and drawbacks of the different technologies are provided in table 2.2.

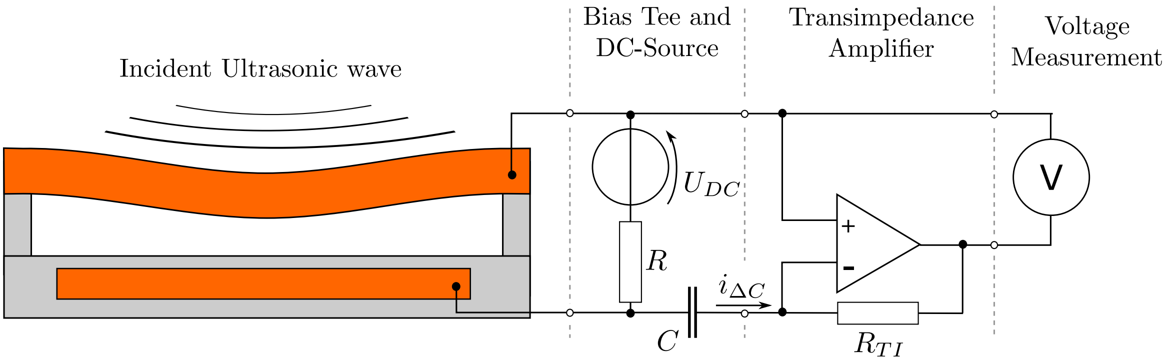

Figure 2.4: Schematic of a CMUT in Receive-Operation

Table 2.2: Comparison of technologies for CMUT receive amplifiers

TECHNOLOGY	CHARACTERISTICS
Transimpedance Amplifier	+ Zero input resistance (ideal) - Frequency characteristic depends on sensor capacity.
Charge amplifier	+ Zero input resistance (ideal) + Feedback capacitor desensitizes amplifier characteristics from the sensor capacity. - Difficult to realize for frequencies greater 1 MHz
Linear amplifier	+ Amplification independent from sensor capacity - The input impedance $>0\,\Omega$ creates a voltage drop over the CMUT, which induces an electrostatic force counteracting the plate velocity.

2.2 CMUT Fabrication and Packaging

Both, fabrication and packaging have a major influence on the characteristics and performance of the CMUT transducer. For that reason, they have to be considered in design generation. In the following, the CMUT fabrication process, wafer design and packaging will be shown for the CMUTs used in this work.

2.2.1 CMUT Fabrication Process

To manufacture the CMUT arrays used in this thesis, a surface micromachining process has been used, which is available at Fraunhofer IPMS. The specialty of this process is the fact, that the CMUT plate is made from amorphous metal, covered with a thin insulating layer [Els+15; Kle+15a]. It comprises the following steps:

1. A polished 6 inch wafer is covered with a thermally grown oxide (figure 2.5a).
2. An aluminum layer for the interconnects of the CMUT is deposited and patterned by dry etching.
3. To insulate the vias from the bottom electrode the aluminum layer is covered with SiO_2 by plasma-enhanced chemical vapor deposition (PECVD) and planarized by chemical-mechanical polishing (CMP).
4. Vias are etched into the SiO_2 and the bottom electrode and the interconnects for the top electrode are deposited by sputtering TiAl (figure 2.5b). From now on, every step affects the mechanical and acoustical characteristics of the CMUT.
5. The subsequent patterning of the TiAl layer defines size and shape of the bottom electrode.
6. A thin layer of SiO_2 is deposited by a CVD to cover the bottom electrode and prevent against electrical breakdowns in case of a pull in (figure 2.1c).
7. A thin layer of amorphous silicon (a-Si) is deposited and a SiO_2 layer are deposited. The a-Si layer is used as etching stop and is necessary to open the release channels later on.
8. The CMUT cavity as well as the release holes are etched into the SiO_2 (figure 2.5c) and filled up with a-Si, which is the sacrificial material for the release etch.
9. Now the cavity height is defined by polishing the a-Si and SiO_2 down to the desired value.

10. After annealing, the TiAl plate is patterned and a XeF_2 release etch through the release holes dissolves the a-Si (figure 2.5e).
11. The cavity is hermetically sealed by atomic layer deposition (ALD) of Al_2O_3 under vacuum atmosphere at a temperature below 200 °C (figure 2.5f).
12. After bond pad opening (figure 2.5g), the CMUT wafer fabrication is finished.

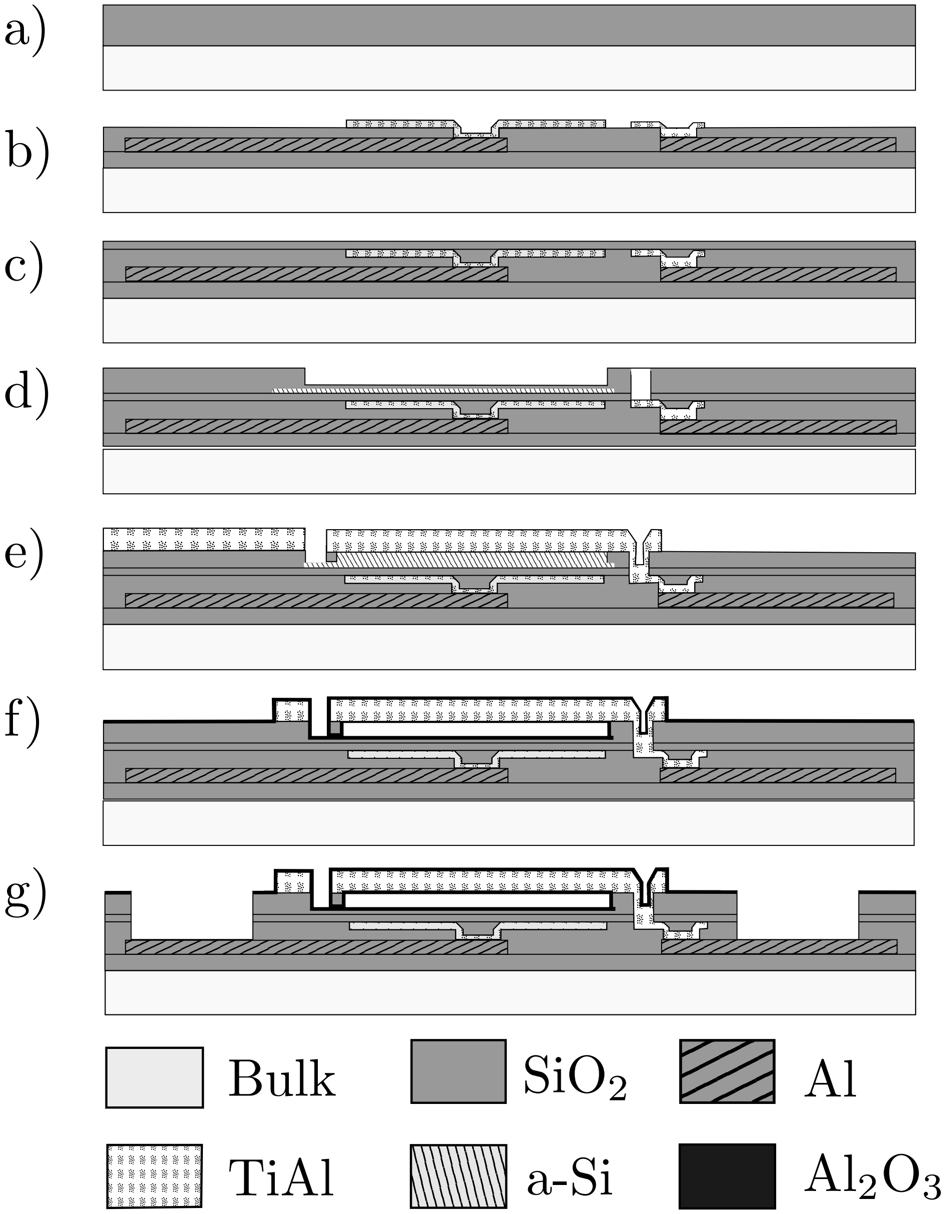

Figure 2.5: CMUT fabrication process [Kle+15a] (further details are described in the text)

Amorphous TiAl is used for the top plate of the CMUT, which is deposited by PECVD. One of the main advantages of TiAl against other materials such as silicon nitride is the controllable stress of the plate, which can be adjusted by annealing [Els+15]. After deposition, the plate is under compressive stress. Annealing the plate shifts the stress from compressive to tensile. An optimal stress within the plate is decisive for a successful CMUT fabrication. If the stress is too low, the plate would stick on the bottom of the cavity or would buckle after the release etch. Too large stress values would reduce the acoustic sensitivity of the CMUT, the wafer curvature gets difficult to handle in further process steps and the risk of plate delamination increases.

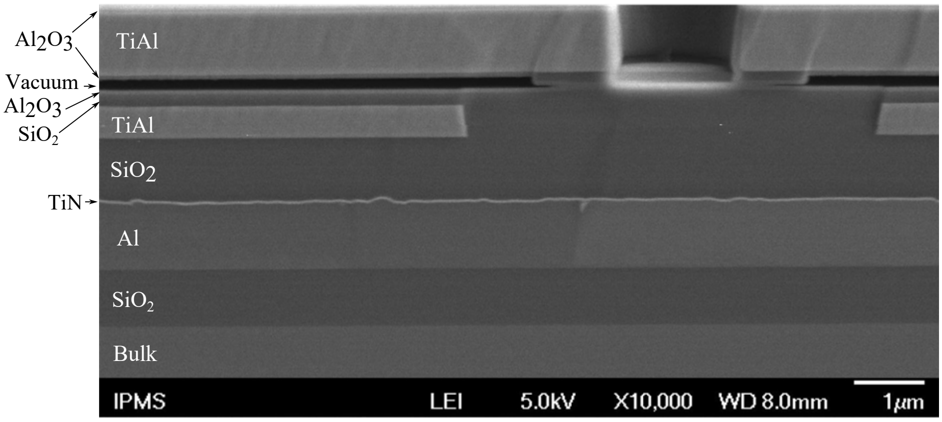

Figure 2.6: Scanning electron microscope picture of cross section of a CMUT cell [Kle+15a]

2.2.2 Sensor Layout

The sensor design used in this work is a test layout for different types of CMUT cells. It contains 113 fully populated 1D arrays within one wafer of 150 mm diameter (figure 2.7).

Each CMUT array contains 128 individual array elements with a lateral array element pitch of 256 µm. The elevational array element size is 1 mm. Within this area, as many CMUTs as possible are placed to maximize the acoustic active area. One wafer contains 10 to 14 different types of arrays.

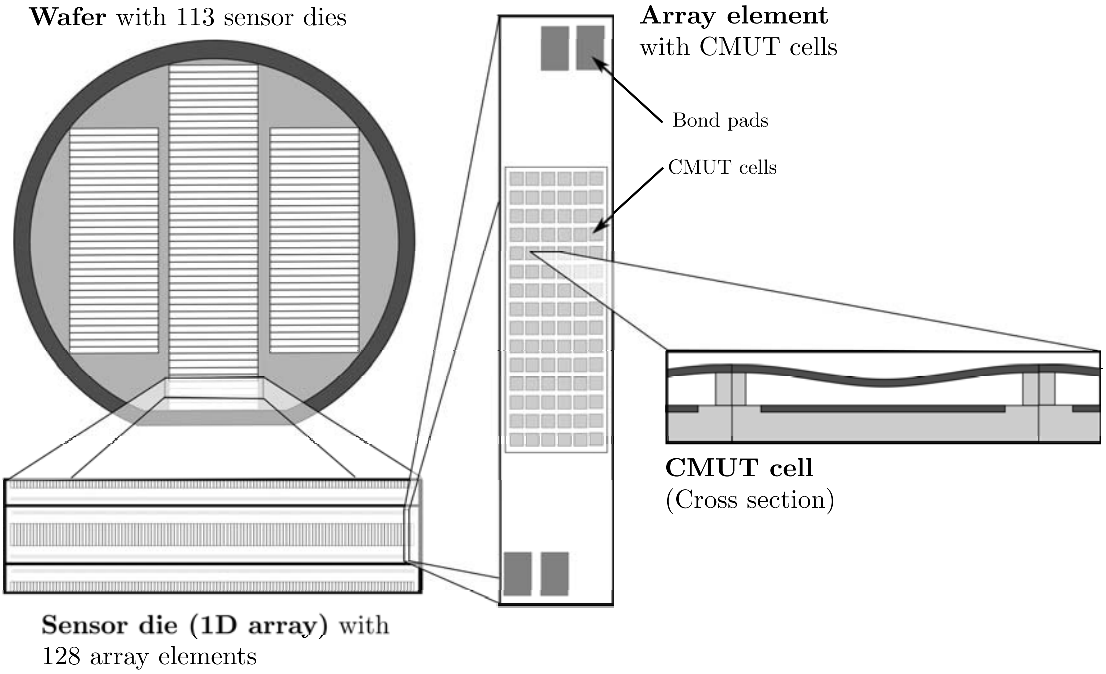

Figure 2.7: Wafer layout of the CMUT sensor dies [Kle+15a]

Three different main purposes are addressed with this layout:

1. Investigation of technical reproducibility of the CMUT elements, both within the array and on the entire wafer
2. Influence of geometrical design variations for the sensor element
3. Investigation of the influence of the following design parameters of the CMUT cell on its acoustic properties:
    - size (10...50 µm)
    - shape (squared, circular)
    - plate thickness (500...2000 nm)
    - gap height (50...200 nm)
    - sealing (ALD-Al_2O_3) thickness (25...50 nm)

2.2.3 Packaging

The operation of the CMUT devices requires a packaging that withstands high electrical drive voltages and currents. For the characterization performed in this work, the packaging should also enable an easy exchange the transducer within the test setups.

For bonding the chips, the high current density has to be taken into account. One array element has a capacity of approximately $30\,\mathrm{pF}$ (including parasitic capacities). Assuming a worst-case scenario, where the array element is driven with a $30\,\mathrm{V}$ sine signal at $30\,\mathrm{MHz}$, a blind current of

$$i_s = 2\pi f(C_{CMUT} + C_p)U_s \approx 170\,\mathrm{mA} \tag{2.9}$$

flows into the CMUT.

All signal connections are wire-bonded from the bond pad on the chip to a pad on the carrier, which is directly connected to a contact pin on the bottom. For each array element, there is one bond via from the chip to the metalized ground plate of the carrier. All 64 remaining pins, which are not used as signal path are via bonds to the metal plate of the carrier in order to withstand the high current density, when all CMUT cells of the entire array are driven.

To use the CMUT array in immersion, the metal plate is covered with insulating varnish and the bond vias are protected with glob top, which is applied by 3D printing (figure 2.8).

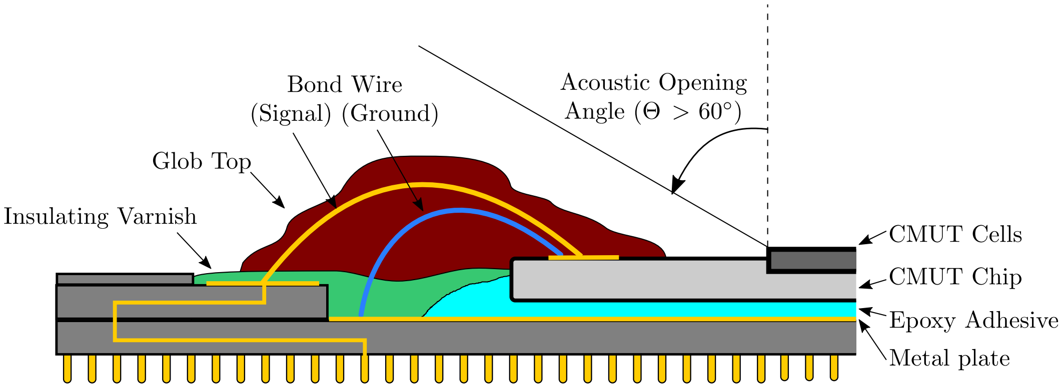

Figure 2.8: Cross section of CMUT array in its package

The radiated ultrasonic signal must not be influenced by the surrounding structures. If these structures are too large, they reflect the acoustic waves and change the sound field of the transducer accordingly. Starting from the directivity of the transducers, requirements for the maximum size of waterproof sealing of the electric contacts is derived.

Therefore, a short analysis of the directivity of the CMUT array shall be proposed. The elevational directivity Γ_{el} of a one-dimensional piston with length D_p can be calculated analytically [Mös07, equ. (3.39)]:

$$\Gamma_{el}(\theta) = \frac{p(\Theta)}{\max(p(\Theta))} = \frac{\sin(k\frac{D_p}{2}\sin\theta)}{k\frac{D_p}{2}\sin\theta}. \tag{2.10}$$

This approximation is valid, if the elevation element size and the wavelength are larger, than the lateral element dimension.

Figure 2.9 shows the elevational directivity Γ for a transducer with a diameter $D_p = 1\,\mathrm{mm}$ using equation (2.10) and a numerical simulation based on the rectangular array geometry. The opening angle[1] Θ_0 can be calculated from the elevational directivity: $\Gamma(\Theta_0) = 0.5$.

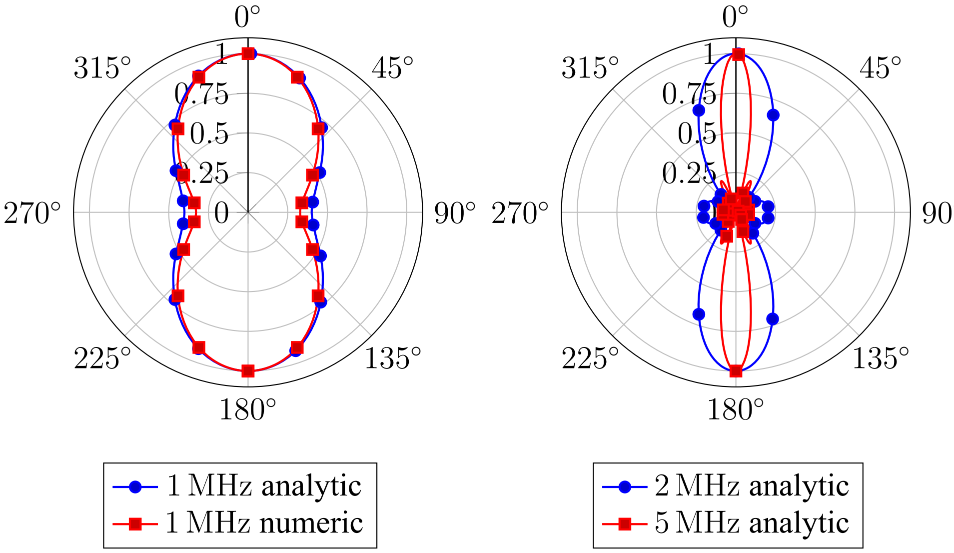

Figure 2.9: Elevational directivity of the array at different frequencies, calculated analytical according equation (2.10) and numerical using a sound field simulation based on point source representation for the complete rectangular CMUT array in water

At $1\,\mathrm{MHz}$, which is the lowest frequency used for CMUT in immersion in this thesis, the maximum opening angle $\Theta_{0,max}$ is calculated and becomes circa $60°$. The glob top (see figure 2.8) is deposited about $200\,\mu\mathrm{m}$ away from the CMUT and its shape is chosen in order to not extend into the acoustic main lobe created by the array element as shown in figure 2.8. Due to this requirement, the influence of the glob top on the sound field is minimized. The following figure 2.10 shows the final package in a ceramic carrier with 320 pins. The carrier

---

[1] The opening angle Θ_0 is defined as the angle Θ to the acoustic axis of a sound source, where the sound pressure amplitude of the main lobe is $6\,\mathrm{dB}$ lower than the maximum sound pressure amplitude in the same distance from the sound source.

allows to incorporate up to two chips (see figure 2.10) which are glued with a non-conductive epoxy adhesive into the carrier.

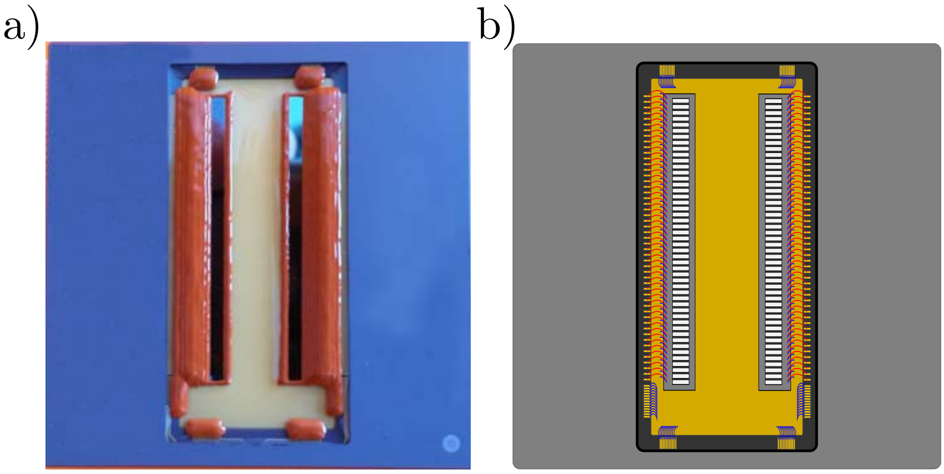

Figure 2.10: Two 1D arrays in a ceramic carrier: photo (a) and bond schema (b)

Chapter 3

Modeling of CMUT Cells in the Design Process

DUE to the complicated fabrication process, the simulation of CMUT cells is essential to estimate the prospective characteristics of the resulting sensor. Here, linear lumped element models as well as finite element based models can be used. In this chapter, both approaches are analyzed and requirements for a new-developed hybrid CMUT model are derived (section 3.1). Section 3.2 describes the CMUT design procedure based on a lumped element model. With such a model, it is possible to derive a design estimation very fast and a basic understanding of the electro-mechano-acoustic effects is provided. Subsequently, the development and implementation of a hybrid simulation model combining the advantages of lumped linear models and finite element models is shown in section 3.3.

3.1 Simulation Models for CMUT Cells

3.1.1 Linear Lumped Circuit Models

Haller presented the first CMUT and adapted a modeling approach based on Mason's model [Mas58] - a linear equivalent-circuit description [HK96]. This approach offers a very fast and computing-inexpensive method to achieve a CMUT cell design. An exemplary design procedure is shown in section 3.2. However, linear circuit models show several limitations as shown in table 3.1.

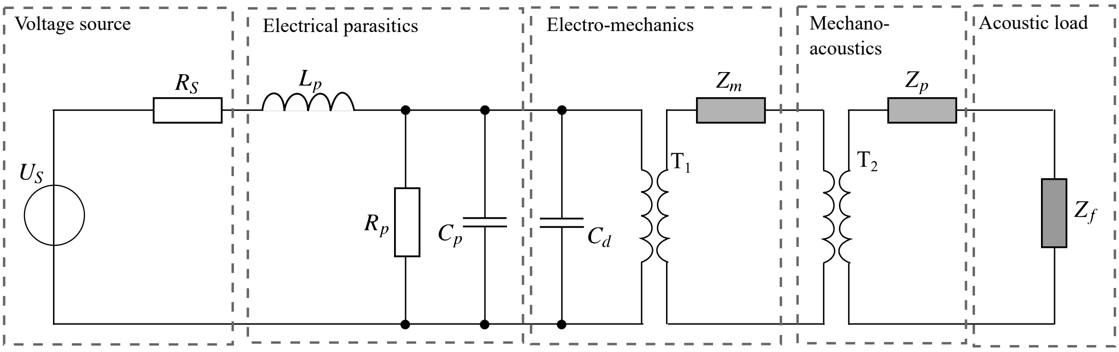

U_S - Drive voltage
R_S - Source resistance
L_p - Parasitic inductance
R_p - Parasitic resistance
C_p - Parasitic capacity
C_d - Static capacity of CMUT

T_1 - Electro-mechanical transducer
Z_m - Mechanical impedance of the plate
T_2 - Mechano-acoustic transformer
Z_p - Parasitic acoustic load
Z_f - Characteristic acoustic impedance of the fluid

Figure 3.1: Linear equivalent circuit for a CMUT as transmitter according to [HK96]

Table 3.1: Limitations of the linear lumped circuit model from figure 3.1

ELEMENT	LIMITATION	USED IN SECTION 3.2
Plate geometry	Analytical solution only for circular shape, rectangular shape possible by using numeric correction factors	Circular shape
Plate structure	Homogenous plate material	Monolayer TiAl plate[1]
Nonlinearity	Nonlinear behavior not included	Small signal excitation (sine sweep $U_{AC} = 1\,\mathrm{V}$)
Acoustic impedance	Only piston or far-field approximation possible	Far-field approximation $Z_f + Z_p = \rho_{fluid} \cdot c_{fluid}$
Capacity change	Not included, effective gap height at given bias voltage can be used	Large displacement in relation to gap height

3.1.2 Finite Element based Models

To overcome the limitations of linear circuit models, finite element models have to be used, as they allow the simulation of any plate shape and material. The effect of the fluidic load has to be included in the FE simulation as well by coupling the mechanic differential equation for the motion of the elements with the acoustic wave equation. Especially for soft CMUTs, which already show large displacements in relation to the gap height at low voltage, it is necessary to simulate the plate movement in time domain. In consequence, a 3D FE model solved by using finite difference methods for a given voltage drive signal is the only possibility to access the plate displacement and sound pressure on top of a CMUT without further approximations apart from numerical uncertainty.

3.1.3 Hybrid Model

The linear lumped circuit model and the full 3D-FE model are two extremes used for CMUT simulation and can be utilized at different states within the design process. Linear equivalent models are first choice to roughly determine an initial CMUT design and provide a starting point for a more detailed analysis. The 3D FE model can be used in the final state of the design process as it is time-consuming to both, set up and solve. However, it offers a very

---

[1] See material properties in table A.1

precise prediction for the real device. The aim is to build a model for CMUT, which is capable of running design optimization loops and allows to find the best CMUT cell design for a given application. This model shall fill the gap between the full 3D representation and linear lumped approaches.

A CMUT is a nonlinear device with a transfer function depending on the input signal and the recent state of the CMUT. Thus, only a simulation in time domain allows to include this effect. Additionally, the displacement of the bendable plate relies on both, the acoustic and the electric load applied to the CMUT. Therefore, the interaction with the surrounding fluid must be implemented and the electronic circuitry has to be added as well.

As a result, this increases the number of parameters, which have to be predetermined or calculated. This includes knowledge about the properties of the surrounding fluid, the connected electrical circuitry, the drive signal applied, the displacement, the surface velocity and the radiated sound pressure. To additionally analyze the electrical characteristics of the CMUT such as its electrical impedance, also the voltage drop over the CMUT and the current flow into the CMUT have to be included.

All the requirements and the derived modeling approaches are summarized in table 3.2. The resulting model can be classified as a hybrid simulation model implementing characteristics from both, lumped circuit models and 3D-FE models. The structure of the model and its individual components are shown in detail in section 3.3.

Table 3.2: Requirements on CMUT simulation models for optimization of the cell design and drive signal

FEATURE	CHOSEN MODELING APPROACH
Any plate geometry possible	Use of a plate model based on finite elements
Nonlinearity of CMUT	Solve model in time domain using finite difference methods
Impedance of connected electronics	Inclusion of electronics as state-space model
Realistic radiation model	Use of a self-developed model for acoustic wave propagation on the CMUTs’ surface
Accurate calculation of current flow	Dynamic equivalent-circuit model with CMUT as current source
Low computational cost	Reduction from 3D mesh to 2D mesh and implementation of a fast-solved structure-fluid interaction

3.2 General CMUT Design Procedure

An optimal design for a CMUT cell has to take the application requirements, the available electronics and its manufacturability into account. This section describes the design process based on an analytical lumped linear circuit model. The aim is to show a general design process as described in figure 3.2. In addition, this section provides an impression on the relation between the design parameters and acoustic characteristics of a CMUT cell.

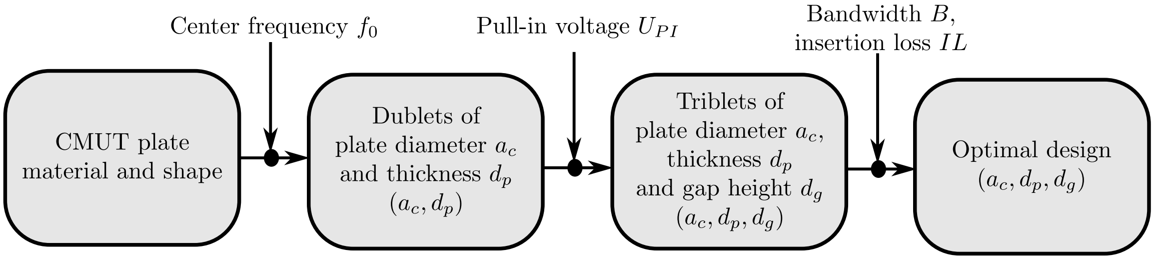

Figure 3.2: Process flow chart for CMUT design generation

Usually, the starting point of the design process is the center frequency of the transducer, which is predetermined by the desired application. For a circular-clamped plate, the eigenfrequency f_0 can be calculated analytically [WKK08, (12)] and represents the resonance frequency of the CMUT cell. Using TiAl as plate material, the corresponding plate diameter a_c for each plate thickness d_p is shown in figure 3.3 to meet the given eigenfrequency f_0. For this estimation, the linear circuit model as shown in figure 3.1 has been used, which allows to consider the impact of the fluid load on the resonance frequency approximately.

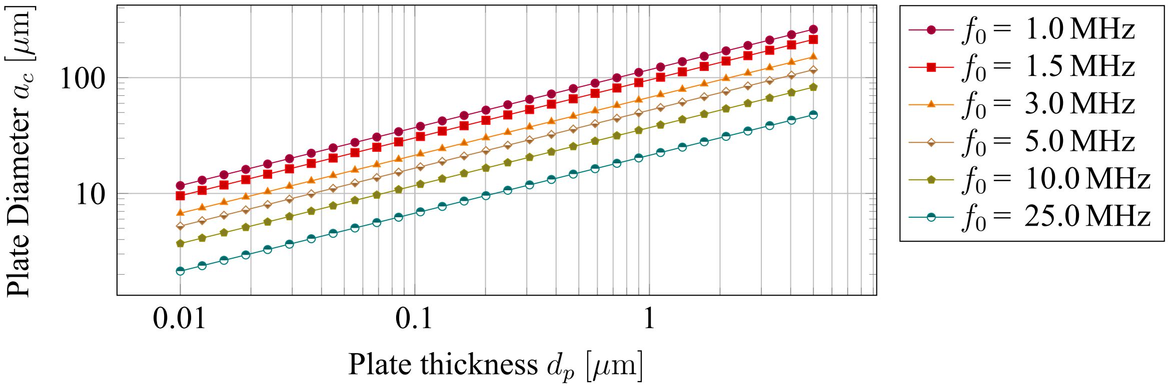

Figure 3.3: Plate diameter a_c vs. plate thickness d_p at a given resonance frequency f_0 for a clamped circular TiAl plate in water.

Before choosing a combination of plate diameter and thickness, also the gap height has to be taken into consideration. The possible send- and receive sensitivity rise, when the vacuum gap d_g of the CMUT is decreased. However, this requires an increase of the necessary bias voltage U_{DC}. A way to proceed is to specify a fixed pull-in voltage U_{PI} and to adjust the gap size accordingly. Figure 3.4 shows the necessary gap height for the plate diameter and thickness pairs of figure 3.3 at a fixed pull-in voltage $U_{PI} = 100\,\mathrm{V}$ [Loh05, equations (3.2),(3.20)].

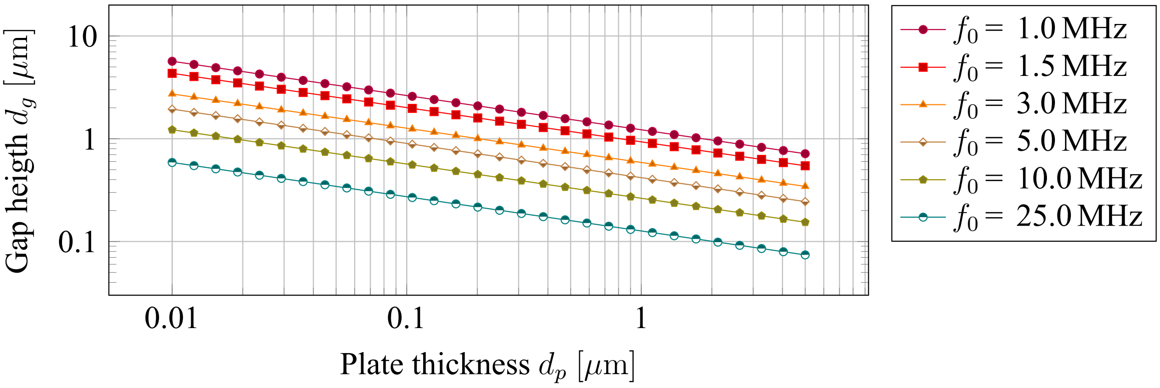

Figure 3.4: Gap height d_g vs. plate thickness d_p for a pull-in voltage $U_{PI} = 100\,\mathrm{V}$. The plate diameter a_c is adjusted according to figure 3.3

Combining both results, any corresponding triplet (a_c, d_p, d_g) fulfills the requirement at a certain given resonance frequency f_0 and a pull-in voltage $U_{PI} = 100\,\mathrm{V}$, but shows a different acoustic characteristic. The triplet is bijective for all parameters: if one value is set, the remaining two values are defined as well.

In the following, an exemplary CMUT working around $10\,\mathrm{MHz}$ center frequency and a pull-in voltage of $100\,\mathrm{V}$ shall be aimed. This type of transducer could potentially be used for medical sonography. To find the best combination of plate size a_c, plate thickness d_p and gap height d_g, a linear lumped element circuit model as shown in [Ahr01] is used. As criterion for evaluating the designs, the send- and receive sensitivity is used. Figure 3.5 shows the sensitivity of the resulting CMUT depending on its plate thickness d_p. The plate diameter a_c and gap height d_g are scaled according to use a valid triplet.

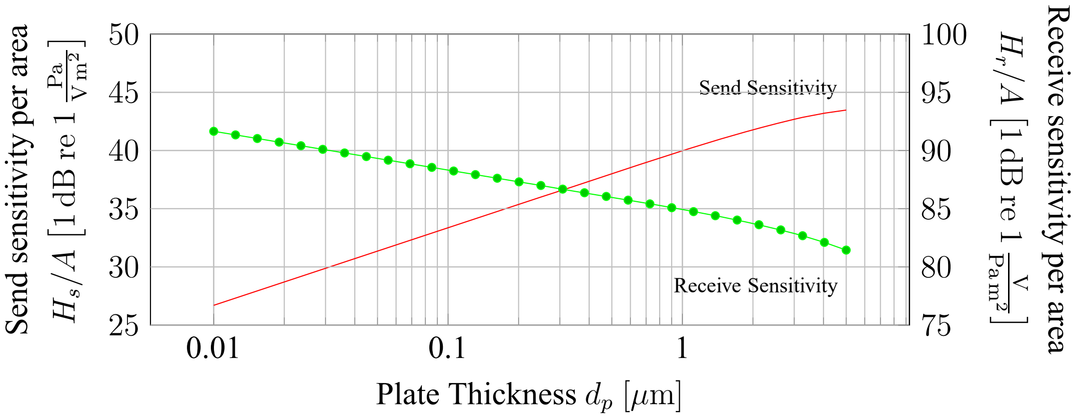

Figure 3.5: Receive sensitivity H_R and send sensitivity H_S normalized to the active area A vs. plate thickness d_p for $f_0 = 10\,\mathrm{MHz}$, $U_{DC} = 0.8U_{PI}$ in water.

If the same CMUT is used as both, source and receiver of ultrasonic signals, the product of send sensitivity H_S and receive sensitivity H_R should be maximal. One commonly used parameter to describe this effect is the two-way insertion loss IL_{sr}.

$$IL_{sr} = 10 \log \left(\frac{1}{H_S \cdot H_R} \right) \tag{3.1}$$

Another important parameter is the bandwidth of the transducer. The bandwidth increases with decreasing plate thickness at the expense of the send sensitivity.

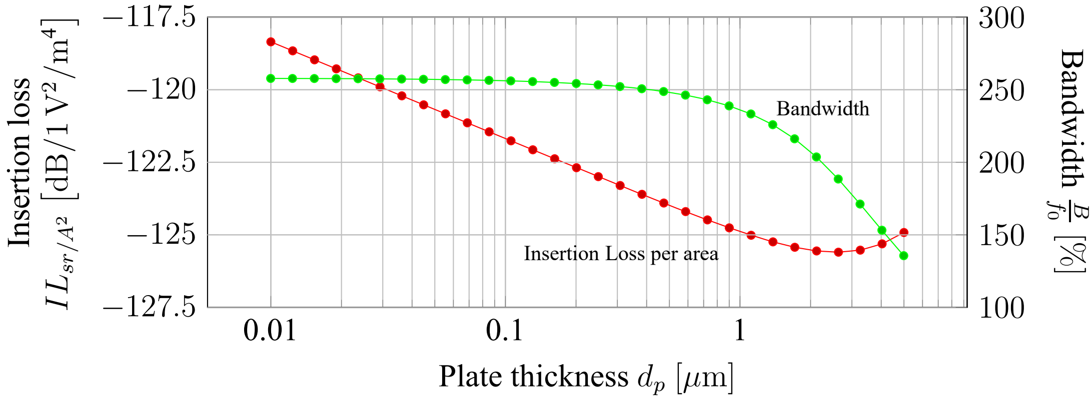

Figure 3.6: Two-way insertion loss in water normalized on the active area A and bandwidth B vs. plate thickness d_p. $f_0 = 10\,\mathrm{MHz}$, $U_{DC} = 0.8U_{PI}$

As result of this study, it is possible to specify a CMUT working at $10\,\mathrm{MHz}$ in water with a pull-in voltage U_{PI} of $100\,\mathrm{V}$. A compromise between bandwidth and insertion loss is attained with a $1\,\mu\mathrm{m}$ thick TiAl plate. The corresponding plate diameter is $35\,\mu\mathrm{m}$ and the vacuum gap height $260\,\mathrm{nm}$ respectively.

This methodology can be used to achieve a CMUT design for a given resonance frequency f_0 and pull-in voltage U_{PI}. It is independent from the model used, but implies a linear behavior of the CMUT. Otherwise, this analysis has to be done for each send- and receive signal individually. Then the exposition of the best design is not as definite and straight forward as given by the procedure introduced here.

3.3 Nonlinear Hybrid CMUT Simulation Model

In the previous section, a method to find the best CMUT cell design was shown, which relays on a linear electro-mechanic-acoustic response of the CMUT cell. In this section, a developed hybrid CMUT model based on a FE-representation of the plate is introduced, which includes the nonlinear behavior of the CMUT and can be used for more complex designs. In addition, the computing time is reduced to a minimum to use the model in optimization loops.

The hybrid model used here is based on a FE representation of the bendable CMUT plate. The structure-fluid interaction is realized using a radiation matrix which can be initialized from the plate's FE-mesh and the specified fluid properties. The electrical circuit is implemented as (time-variant) state-space representation. In transmit operation, any numeric or analytical drive signal (voltage or current) can be used. A full overview on the model is provided in figure 3.7.

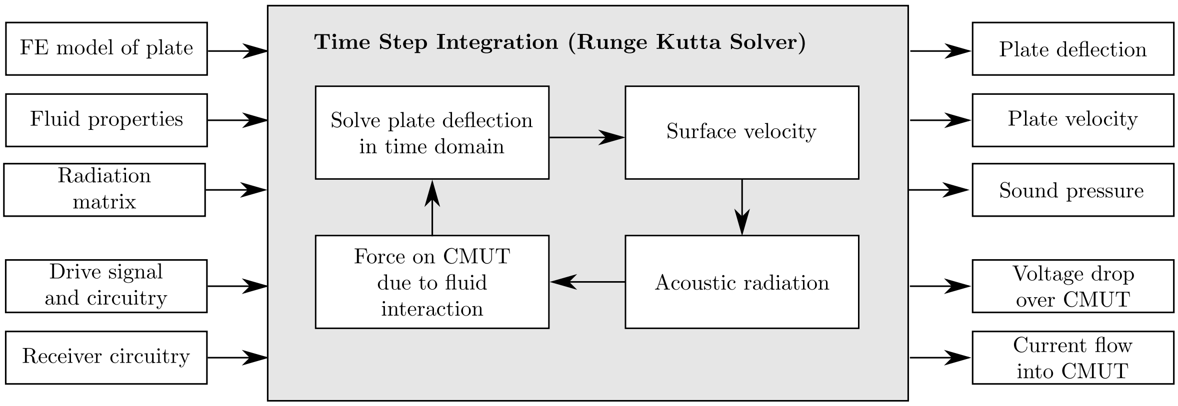

Figure 3.7: Overview on the developed hybrid CMUT model

When the model is solved, first the initial deflection of the plate for a given bias voltage is calculated. For this reason, the model is solved statically at the voltage U_{DC}. Afterwards, a Runge-Kutta solver is used to simulate the movement, the sound pressure for each mesh element of the CMUT as well as the state variables of the electrical circuitry. All three parts of the model - the mechanical plate displacement, the structure-fluid interaction and the electrical circuit influence each other within the same time step. Thus, they are implemented into the same Runge-Kutta algorithm as they cannot be calculated sequentially.

All mechanical, electrical and acoustical state variables are saved during the calculation and can be used for post-processing and evaluation of the CMUT design and drive signal. In the following sections, the individual parts are described in detail.

3.3.1 FE Model of the CMUT Plate

a) CMUT as Reissner-Mindlin plate

As mechanical representation of the CMUT, a FE model of the plate has been implemented in Matlab. The FE representation is created from linear quadliteral elements based on the Reissner-Mindlin plate theory [FG09]. This approach extends the Kirchhoff plate theory to thick plates by adding shear transformation effects [Oña13]. This allows to simulate also very high mechanical displacements as well as very thick plates and provides the opportunity to implement sandwich plates by extending the representation to a 3D FE model. For ordinary CMUT designs and driving conditions the results do not differ from the Kirchhoff-Love plate theory, as the plate thickness of the CMUT is large compared to the deflection and thin compared to the lateral plate dimensions.

The plate of the CMUT considered in this work consists of three material layers, comparable to a sandwich plate (see figure 2.1). The thick core is made from TiAl and surrounded by a thin layer of Al_2O_3 on top and bottom. Even if the Al_2O_3 layers are very thin compared to the TiAl core, these layers have great impact on both the static and the dynamic mechanical characteristics of the plate. It is not possible to model the plate as 3D-FE mesh for this structure, because the thin Al_2O_3 layer requires very small finite elements and would rise the number of nodes dramatically.

When the CMUT plate is covered with a thin insulation material layer, a 3D-FE representation consists of an enormous number of elements. The maximum element size should be in the range of the thickness of the insulation layer. A rough estimation shows, that a squared CMUT plate with $50\,\mu\mathrm{m}$ edge length, $1\,\mu\mathrm{m}$ plate thickness and a $20\,\mathrm{nm}$ insulation layer on bottom and top leads to 6.5 million cubic mesh elements. To avoid the obstacle of corresponding large calculation times, the sandwich plate is transformed into a homogenous plate [CTP05] as shown in figure 3.8.

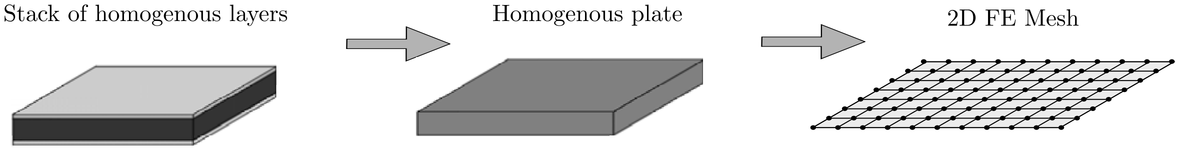

Figure 3.8: Conversion of the Al_2O_3/TiAl/Al_2O_3 sandwich structure to a homogenous plate and a 2D-FE mesh

The flexural rigidity D_c of the homogenous plate can be calculated from the distances of the k-th and $(k-1)$-th layer from the neutral axis of the plate, the Young's modulus E_k and the Poisson ratio ν_k in between those layers [CTP05, equ. (2-3)]:

$$D_c = \frac{1}{3}\sum_k \frac{E_k}{1-\nu_k^2}\left(z_k^3 - z_{k-1}^3\right), \tag{3.2}$$

$$\nu_c = \frac{1}{3D_c}\sum_k \frac{\nu_k E_k}{1-\nu_k^2}\left(z_k^3 - z_{k-1}^3\right). \tag{3.3}$$

From the flexural rigidity D_c, an effective Young's modulus E_c can be calculated assuming, that the plate thickness of the homogenous plate equals the total plate thickness of the sandwich plate:

$$E_c = 12D_c(1-\nu_c^2)\left(\frac{2}{d_c}\right)^3. \tag{3.4}$$

Figure 3.9 illustrates the change of the concentrated Young's modulus E_c for different thickness ratios of a symmetric sandwich plate.

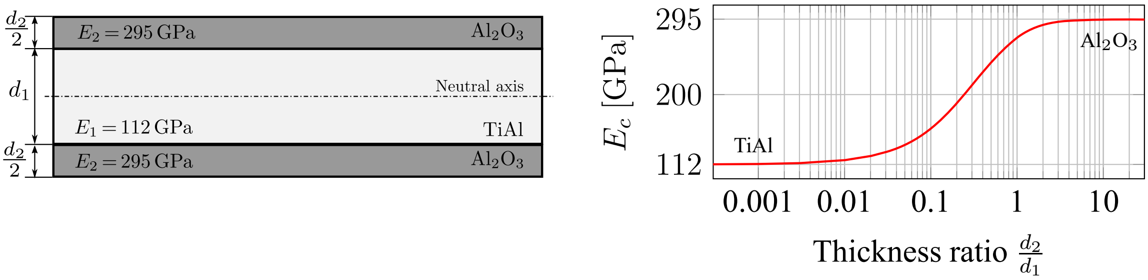

Thickness $^{d_2}/_{d_1}$	0.001	0.01	0.05	0.1	0.5	1.0	2.0
Young's modulus $^{E_c}/_{E_0}$	1.001	1.05	1.22	1.41	2.15	2.43	2.5

Figure 3.9: Resulting effective Young's modulus E_c of the homogenized plate vs. thickness ratio $^{d_1}/_{d_2}$ (Al_2O_3/TiAl/Al_2O_3 plate, $d_1 + d_2 = 1$ µm).

As exemplary indicator for the high impact of the Al_2O_3 layers on the CMUTs characteristics, the eigenfrequencies of a homogenous plate and a sandwich plate are investigated. The eigenfrequency of a clamped circular plate is proportional to the square root of its Young's modulus ($f_0 \sim \sqrt{E_c}$). A 950 nm thick TiAl plate with comparably thin 25 nm Al_2O_3 layers on the top and bottom shows an approximately 10% higher resonance frequency than a 1 µm thick plate from pure TiAl.

b) Boundary conditions

The reduction of the 3D structure to a 2D-FE model implicates, that the clamping of the flexure plate needs to be analyzed further. Most lumped CMUT models assume a fully clamped plate [Tes+06; Loh05; Ayd+14], as it is simple to implement and handle. The comparison of dynamic measurement results and white-light interferometer pictures indicates, that the static deflection of the model with clamped boundaries is too low and the resonance frequency too high especially for high-frequency devices [KU14, Fig. 5]. Therefore, an additional mesh element is added at the boundary of the plate, which defines the stiffness K_b of the boundary (see figure 3.10). The elementary stiffness matrices of these mesh elements have the same structure as the Reissner-Mindlin plate but another absolute value. In addition, the nodes of this matrix are fixed in w-direction. With this approach, the stiffness of the boundary can be adjusted to the actual behavior of the CMUT cells.

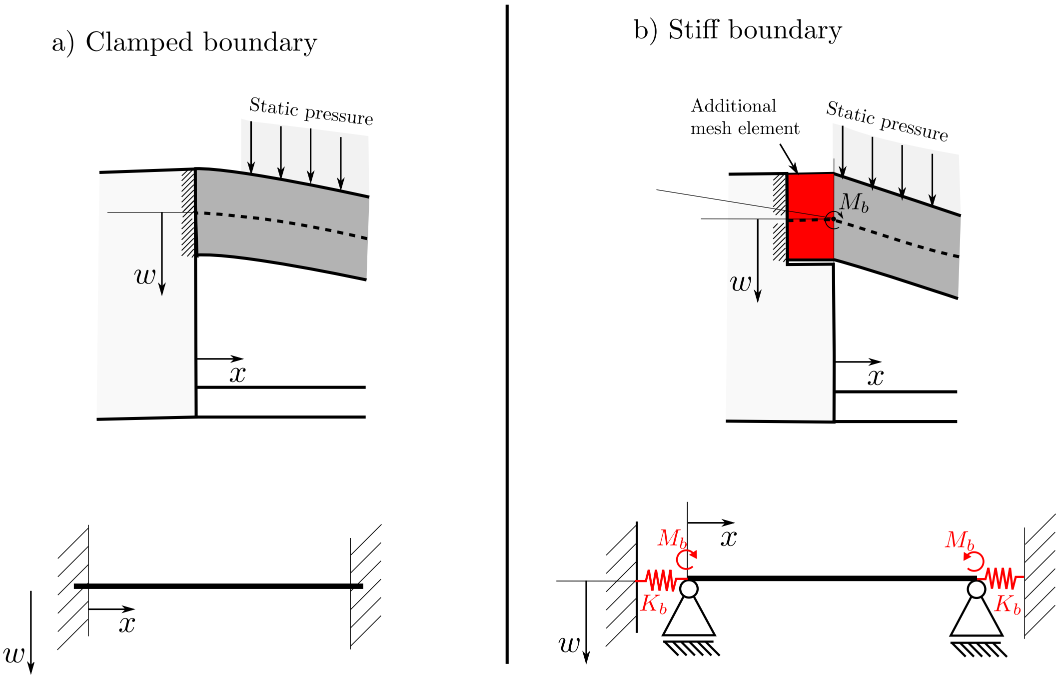

Figure 3.10: Plate model (a) with clamped boundary and (b) with additional mesh element to include the boundary stiffness and initial deformation

Especially for rectangular CMUTs, each border can reveal a different boundary stiffness K_b. White light interferometer pictures of a CMUT array element indicate, that the same CMUT cell type within an array usually show different behavior depending on its location. This effect increases with rising CMUT cell dimension.

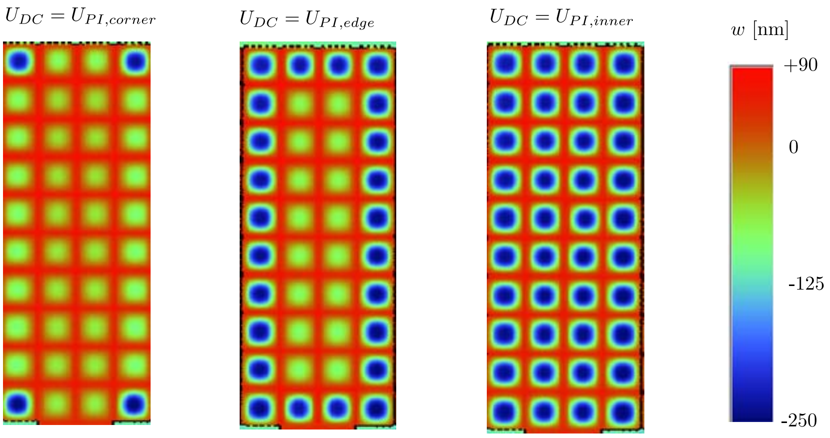

Figure 3.11: White light interferometer picture of an CMUT array element. Depending on the boundary condition, the pull-in voltage of the elements changes.

Within one array element, two different boundary stiffness values appear. K_{in} represents the stiffness of an inner boundary between two adjacent CMUTs. At the borders of the array element, the clamping is less stiff and is represented by the value K_{out}. This leads to three different cell types within the array element: inner CMUT cells, which are surrounded by four other CMUTs, cells at the edge, which are in contact to three CMUTs, and the cells at the four corners of the array element. Figure 3.12 shows the adopted model, replacing the general boundary stiffness K_b by the location-dependent stiffnesses K_{in} and K_{out}.

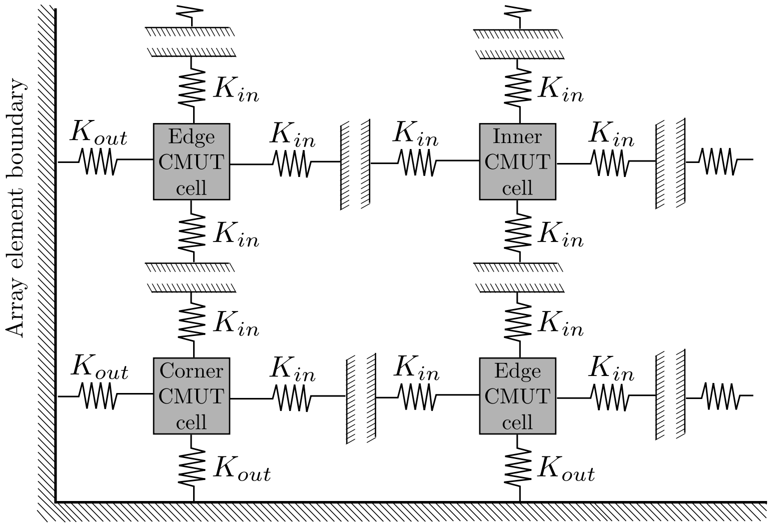

Figure 3.12: Boundary stiffness of CMUTs within an array

Beside the boundary stiffness, also the real shape of the plate has to be taken into account, because the plate is not ideally flat right after deposition. This effect results in an initial deflection already for the pressure- and stress-free plate. As the deflection is small compared to the plate diameter, two options exist to also include this into the model:

- the reduction of the local effective gap height on the deformation of the plate after deposition, or
- adding a static moment M_b to the boundary elements, which deflects the plate. Then, the value for M_b has to be determined, so that the bending of the plate equals the real initial deformation of the plate.

Although both approaches are only an approximation to the reality but offer a sufficiently take this effect into account for simulations in a design process.

In the simulation model used in this work, a moment is applied to the boundary, because only the center deflection of the CMUT either before or after release needs to be applied to the simulation. The value of the static moment M_b can be solved in a pre-processing step prior the dynamic time-step integration. The determination of the stiffness K_b and the moment M_b is explained in detail in section b).

3.3.2 Static Deflection

The static deflection w_0 of a CMUT as shown in figure 3.13 is caused by three parts.

- As discussed in the previous section, an initial displacement w_{fab} exists, because no ideally flat surface is created by the CMP process prior depositing the CMUT plate.
- The CMUT's cavity is sealed and contains vacuum. Thus, the static atmospheric pressure induces a deflection w_{p_0} of the plate towards the bottom electrode.
- To counteract this effect and keep the plate free-standing even for small gap sizes, a controlled intrinsic tensile stress is created in the CMUT fabrication and forms the third deflection component w_σ.

$$w_0 = w_{fab} + w_{p_0} + w_\sigma \tag{3.5}$$

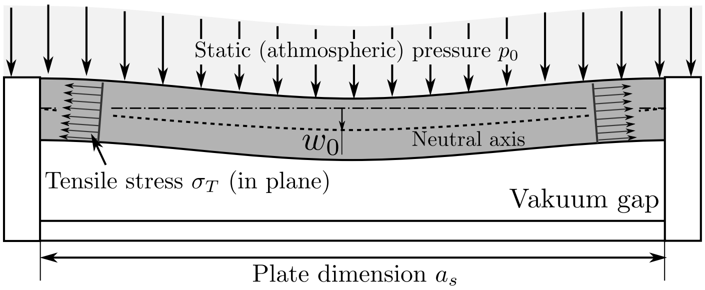

Figure 3.13: Deflection of the plate due to static pressure from fluid, tensile in-plane stress and the fabrication process

a) Static Atmospheric Pressure and Mechanical Stress

At first, the influence of the static atmospheric pressure p_0 and the tensile mechanical stress σ_T are investigated. The parameters w_{fab} and K_b are fabrication- and design specific and therefore ignored first. Here, the plate is assumed to be deposited ideally flat ($w_{fab} = 0$) and is ideally clamped ($K_b = \infty$).

The in-plane tensile stress σ_T and the surrounding static pressure p_0 are applied to the FE model of the CMUT plate and the resulting center deflection w_0 is calculated. Figure 3.14 demonstrates, that the deflection is dominated by the static pressure p_0 and rises dramatically with increasing the plate's edge length a_s. The tensile stress σ_T has a minor impact on the center displacement w_0 of small CMUT cells. However, especially for air-borne transducers with large cell dimensions a_s, it is very important to control the mechanical stress of the CMUT's plate to keep the plate free-standing and achieve the desired gap size accurately.

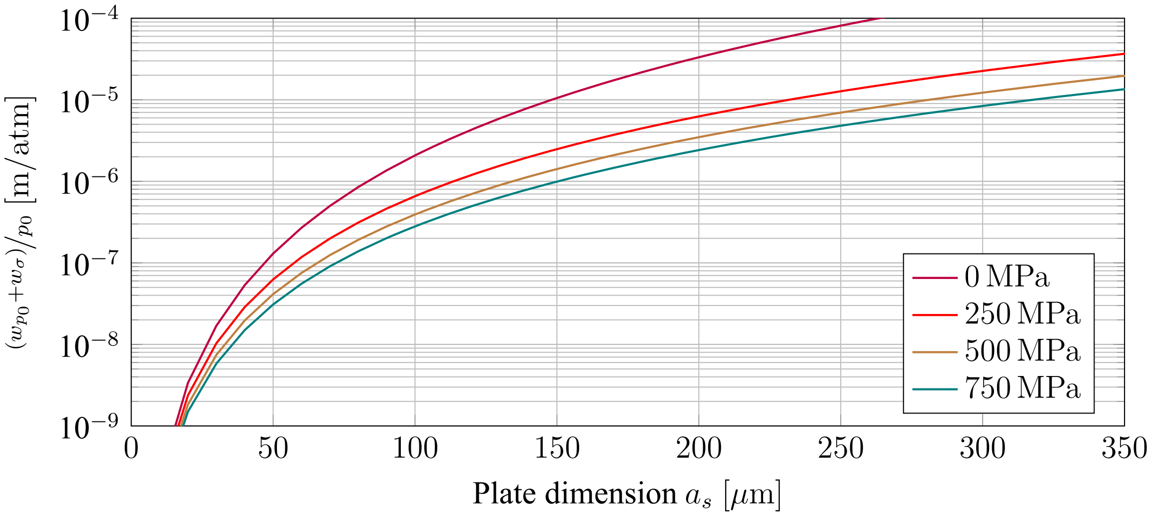

Figure 3.14: Static deflection per applied pressure vs. plate dimension for a rectangular plate under tensile stress (design 1 in table B.3)

Varying stress also changes the dynamic characteristics of the CMUT, such as resonance frequency, pull-in voltage and sensitivity. The effect on in-plane tensile stress σ_T on the eigenfrequency f_0 of the CMUT is shown in figure 3.15.

Especially for devices smaller than $50\,\mathrm{nm}$ figure 3.15 illustrates, that the stress can be used as additional degree of freedom in fabrication to tune the eigenfrequency of small CMUT cells.

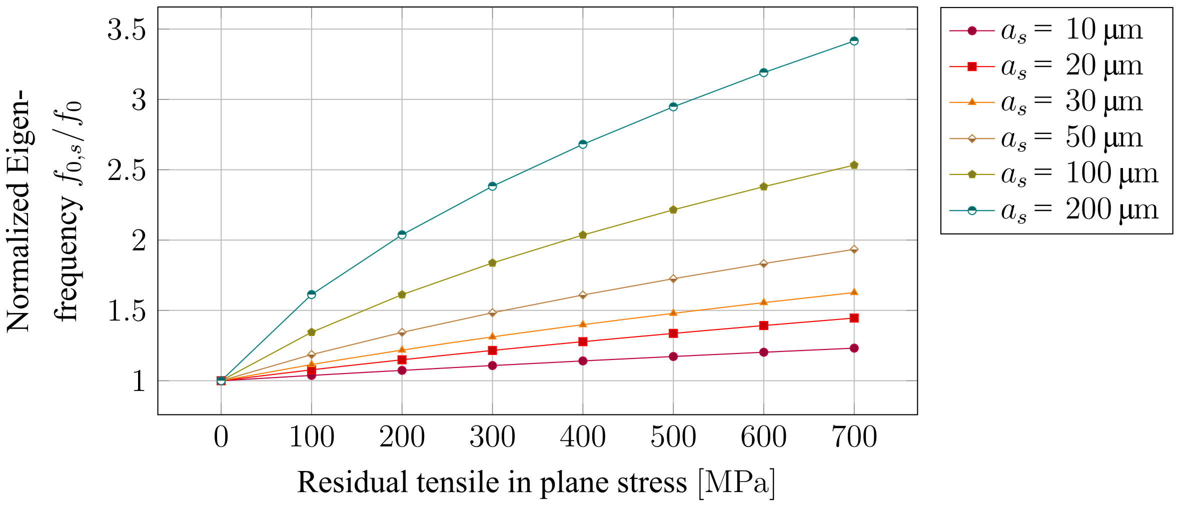

Figure 3.15: Eigenfrequency $f_{0,s}$ of pre-stressed plate normalized to the unstressed plate f_0 for different in-plane stress values and plate dimensions (Design 1 in table B.3)

b) Determination of Stress, Boundary Stiffness and Static moment of Fabricated Devices

The boundary stiffnesses K_{out} and K_{in} and the static moment M_b are three important parameters for the CMUT cell simulation. However, they are not directly accessible from the design and cannot be measured directly. The in-plane stress σ_T is set as fourth unknown parameter, as the measurement of the stress is performed by analyzing the wafer bow. Therefore, the obtained stress value can only be an estimation for the real stress present within the CMUT plate.

For this reason, the parameters σ_T,M_b,K_{out} and K_{in} have to be determined indirectly. Therefore, a procedure based on the static displacement w_0 of the CMUT at different DC bias voltages U_{DC} has been developed. Figure 3.16 shows the center deflection of the CMUT cells within one array element versus the DC bias voltage. The CMUTs are subdivided into inner CMUTs, edge CMUTs and corner CMUTs (see figure 3.12). It turns out, that the deflection of the inner CMUTs smaller than the deflection of the edge elements at the same bias voltage.

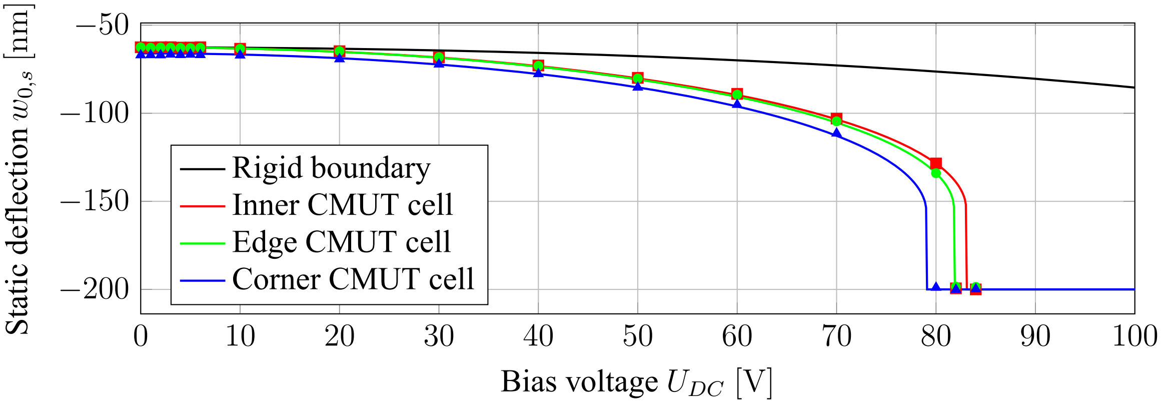

Figure 3.16: Comparison of static deflection between simulation (lines) and measurement (markers) for one CMUT cell type at different boundary conditions (Design 2 in table B.3)

From the displacement measurements, now the parameters $(M_b, K_{in}, K_{out}, \sigma_T)$ have to be identified. Therefore, the FE model is initialized with a triplet $(K_{in}, K_{out}, \sigma_T)$ for each cell type (corner, edge, inner CMUT). Then the center deflection without bias voltage at atmospheric pressure ($p_0 = 1\,\mathrm{atm}$) is calculated for different static moments M_b. Using the Newton–Raphson method, the moment is varied until the difference between measured and simulated displacement is less than $0.1\,\mathrm{nm}$ in the center of the cell. Afterwards, the deflection can be calculated for different DC bias voltages for the parameter quartet $(M_b, K_{in}, K_{out}, \sigma_T)$. The quartet is rated by calculating the mean square error between simulated and measured deflection values. This procedure is run in a Nealder-Mead simplex search algorithm, until a parameter set $(M_b, K_{in}, K_{out}, \sigma_T)$ with minimum mismatch between measured and simulated deflection is achieved for all three types (corner, edge and inner CMUT).

For the best fit achieved (figure 3.16), a maximum difference Δw between measurement and simulation of less than $\pm 1.5\,\mathrm{nm}$ over the full voltage range occurred. This value is within the measurement uncertainty of the interferometer. The best fit was obtained for an in-plane tensile stress value of σ_T=249.8 MPa, which is close to the measured stress of $236\,\mathrm{MPa}$. Thus, the accordance of these stress values is gratifying. The boundary stiffnesses obtained are $K_{in} = 67\,\mathrm{kN/m}$ and $K_{out} = 52\,\mathrm{kN/m}$.

The calculated parameters M_b, K_{in} and K_{out} are design-specific. However, they can be used for simulating similar designs prior fabrication. Thus, a validation and update of those parameters is recommended as final step in the design process or if major changes in the design are done in comparison to the reference design, for which the boundary stiffness has been investigated.

3.3.3 Structure-Fluid Interaction

The plate of the CMUT has a very low mechanical impedance, which means that an in relation small force can create a big displacement of the plate. If the CMUT plate moves a fluid, a surface pressure is created, which is radiated as acoustic wave into space. From this interaction, a restoring force F_{fluid} counteracts the dynamic displacement of the plate and has to be taken into account.

To include this in the simulation model, a fast calculation approach for the structure-fluid interaction in time domain has been developed. Figure 3.17 gives an overview on the model, which will be described within this section.

From the equation of movement, the surface deflection and its higher derivative are solved. These values are the input for the acoustic interaction represented by the equation of continuity. The result is the surface pressure created due to the CMUTs plate deflection. A novel algorithm based on a radiation matrix allows to calculate the absolute sound pressure depending on the wave propagation on the CMUTs surface. The reactive force of the fluid created by the sound pressure is the input for the force vector of the equation of movement in the next time step. In the following, these steps will be described in more detail.

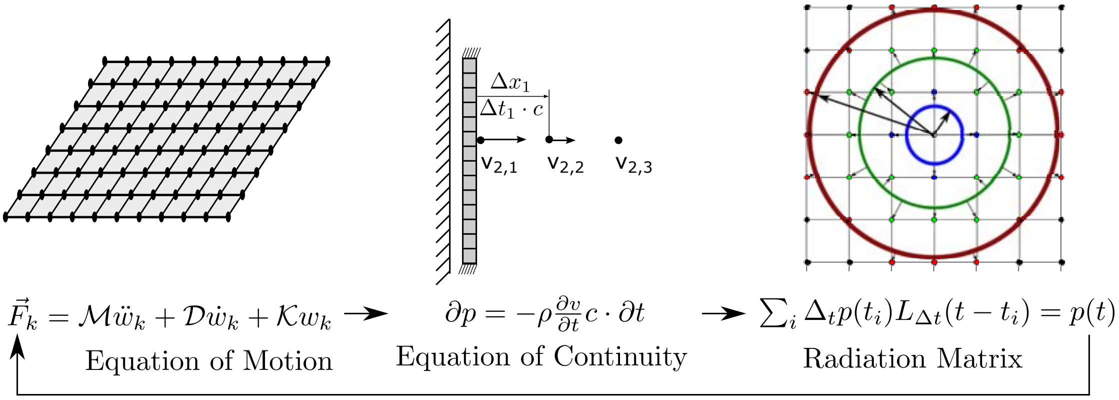

Figure 3.17: Overview on the dynamic structure-fluid interaction model

a) Dynamic Mechanical Displacement

The nonlinearity of the CMUT requires to solve the displacement w of the CMUT plate in time domain. A mathematical formulation as initial value problem allows to calculate the second derivative $\ddot{w}$ of the displacement for the next $(n+1)$-th time step as function of the displacement w and surface velocity $\dot{w}$ of the n-th time step t_n:

$$\ddot{w}_{n+1} = f(t_n, w_n, \dot{w}_n). \tag{3.6}$$

Using the mass matrix $\mathcal{M}$, stiffness matrix $\mathcal{K}$ and damping matrix $\mathcal{D}$ from the FE model and the force vector $\vec{F}$ yields to

$$\ddot{w}_{n+1} = \mathcal{M}^{-1} \cdot (\vec{F}_n - \mathcal{K}w_n - \mathcal{D}\dot{w}_n). \tag{3.7}$$

The integration of $\ddot{w}_{n+1}$ leads to the surface velocity $\dot{w}_{n+1}$ and the displacement w_{n+1} of the CMUT plate in the $(n+1)$-th time step:

$$\dot{w}_{n+1} = \dot{w}_n + \ddot{w}_{n+1} \cdot \Delta t, \tag{3.8}$$

$$w_{n+1} = w_n + \dot{w}_{n+1} \cdot \Delta t. \tag{3.9}$$

The equations (3.7) to (3.9) are solved within a third-order Runge-Kutta algorithm and deliver the time-dependent displacement $w(t)$ of the CMUT plate in vacuum. Any dynamic load such as the coupled fluid, which is moved by the plate is part of the force vector $\vec{F}$.

The force vector $\vec{F}$ itself comprises three components

$$\vec{F} = \vec{F}_0 + \vec{F}_{el,AC}(t) + \vec{F}_{fluid}(t) : \tag{3.10}$$

- the time-independent static force F_0, which contains the static air pressure, the in-plane stress of the plate and the electrostatic force due to the bias voltage.
- the time-dependent electrostatic force $F_{el,AC}(t)$, which is created by the applied AC voltage $F_{el,AC}$ and
- the force due to structure fluid interaction $F_{fluid}(t)$:

b) Calculation of Surface Pressure

In the next steps, the restoring force $F_{fluid}(t)$ of the fluid on the CMUT plate will be calculated from sound pressure p, on the surface of the CMUT. Therefore, the sound pressure p has to be obtained from surface velocity $\dot{w}$. Both parameters are linked by the Euler equation:

$$\rho\frac{\partial v}{\partial t} = -\frac{\partial p}{\partial x}. \tag{3.11}$$

The resulting surface pressure p depends on the speed of sound c in the fluid and the mass density ϱ of the fluid. Within an infinitely small time step ∂t, the wave travels the distance

$$\partial x = c \cdot \partial t. \tag{3.12}$$

This allows to calculate the time-dependent change of the surface pressure

$$\partial p = -\rho\frac{\partial v}{\partial t}c \cdot \partial t. \tag{3.13}$$

For the implementation of equation (3.13) into the Runge-Kutta solver, the time-continuous formulation must be converted into the form of equation (3.6) for discrete time steps:

$$\Delta_{(x,t)}p = -\rho \cdot \dot{v} \cdot c \cdot \Delta t. \tag{3.14}$$

Here $\Delta_{(x,t)}p_k$ describes the change of the sound pressure created by the plate acceleration $\dot{v}$ over the time Δt while the sound propagates the distance Δx. As only the change of the sound pressure directly at the CMUTs' surface is responsible for generating the reacting force of the fluid, $\Delta_{(x,t)}p_k$ has to be subdivided into a time- and a location-dependent component. For this reason, the wave propagation on the CMUTs' surface has to be considered in more detail.

Figure 3.18 shows the sound velocity of the radiated wave for three time steps. In the first time step (figure 3.18 a)), every mesh-element has a velocity $\dot{w}$ and radiates an acoustic elementary wave. Thus, the wave on top of one mesh element has the velocity $v_{1,1}$. As the wave does not reach positions 2 and 3 yet, the sound velocities $v_{1,2}$ and $v_{1,3}$ remain zero. One time step Δt_1 later (figure 3.18 b)), the wave has propagated the distance Δx_1 from position #1 to position #2 and a velocity $v_{2,2} \neq 0$ can be measured at this point. As the plate accelerates further within this time step, an updated surface velocity $v_{2,1}$ is obtained directly on the CMUT at position #1. However, this model is only valid if the mesh elements are small compared to the wavelength of the radiated ultrasonic wave. Only in this case, the individual mesh elements can be modeled as monopolic sound sources.

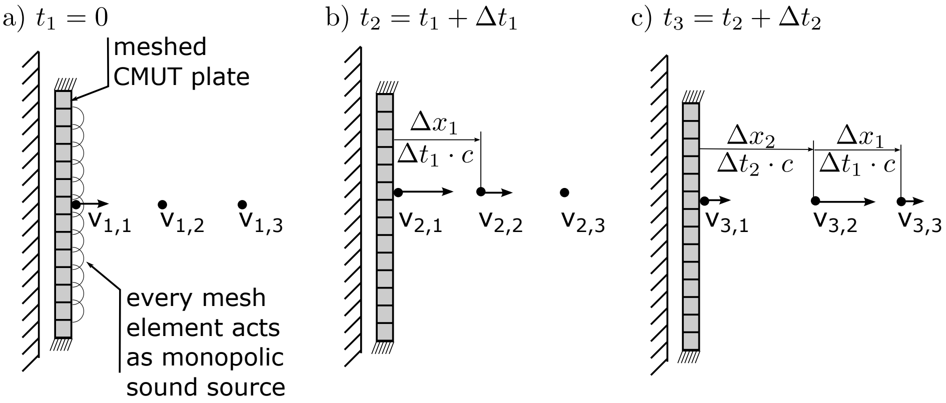

Figure 3.18: Calculation model for the sound pressure on the surface of the CMUT created due to the deflection of the CMUT's plate

The aim is now to calculate the change $\Delta_t p$ of the sound pressure within one time step at the surface:

$$\Delta_t p = \Delta_{(x,t)} p - \Delta_x p, \tag{3.15}$$

$$\Delta_t p = -\rho \cdot \dot{v} \cdot c \cdot \Delta t - \Delta_x p. \tag{3.16}$$

The change of the sound pressure due to propagation $\Delta_x p$ from the surface of the CMUT can be formulated as

$$\Delta_x p = p_{2,2} - p_{2,1}, \tag{3.17}$$

$$\Delta_t p = -\rho \cdot \dot{v} \cdot c \cdot \Delta t - p_{2,2} + p_{2,1}. \tag{3.18}$$

From this point, it is possible to efficiently calculate the surface sound pressure change $\Delta_t p$ from $p_{2,1}$ to $p_{2,1}$. Therefore, the sound pressure drop of the emitted wave propagating a distance Δx has to be evaluated. As discussed before, each element can be abstracted as a monopolic sound source radiating into the semi-infinite space. The sound pressure p_{MS} in the distance r of the center of a monopolic source is can be formulated as equation (3.11) [Mös07, equ. (3.10)]

$$p_{MS}(r) \sim \frac{e^{-jkr}}{r}. \tag{3.19}$$

This equation depends on the frequency and cannot be solved directly in time domain. But for small time steps Δt the distance $r = c \cdot \Delta t$ is small compared to the wavelength of the radiated waves and kr approaches zero. Then the frequency-dependent exponential function disappears:

$$\lim_{kr\to 0} p_{MS}(r) \sim \frac{e^0}{r} = \frac{1}{r}. \tag{3.20}$$

A phenomenological explanation of this effect is, that the phase of the wave does not significantly change within one time step. This is only applicable if the sampling frequency f_s in the time step integration is significantly higher than the largest relevant frequency f_{max} of the CMUT:

$$f_s \gg f_{max}. \tag{3.21}$$

The area $A(x, y)$ of a mesh element with its center at the coordinate (x, y) represents the surface of a radiating semisphere with the radius $r_{0,(x,y)}$:

$$r_{0,(x,y)} = \sqrt{A_{x,y}/(2\pi)}. \tag{3.22}$$

Together with equations (3.17) and (3.18), it is possible to calculate the change of the surface sound pressure $\Delta_t p$.

$$p_{2,1} \cdot \left(r_{0,(x,y)} + \Delta x\right) = p_{2,2} \cdot r_{0,(x,y)} \tag{3.23}$$

$$\underbrace{p_{2,1}}_{\Delta_t p =} = \underbrace{\frac{r_{0,(x,y)} + \Delta x}{r_{0,(x,y)}}}_{L_a} \cdot \underbrace{p_{2,2}}_{\cdot \Delta_{(x,t)} p} \tag{3.24, 3.25}$$

The introduced amplitude scaling factor L_a has to be recalculated for every mesh element at any time, when the time step Δt changes. Finally, inserting equation (3.25) into equation (3.18) allows to calculate the change of the sound pressure $\Delta_t p$:

$$\Delta_t p = -L_a \cdot \rho c \cdot \ddot{w} \cdot \Delta t. \tag{3.26}$$

Equation (3.26) is solved by the Runge-Kutta algorithm and offers a simple method to calculate the pressure change in time domain and can be used in various types of models. The Matlab implementation of the differential equation is provided in appendix A.

c) Self Radiation (Radiation Matrix)

When an elementary wave is emitted from one mesh element, the wave also propagates on the CMUTs' surface laterally, which creates a temporary and spatial reactive force on the plate. This mechanism is called self-radiation.

The amplitude loss of the wave from its source node to any other node in the mesh is calculated by adopting equation (3.24) and stored into an amplitude loss matrix L:

$$L = (L_{ij})_{N\times N}\,, \tag{3.27}$$

$$L_{ij} = \frac{1}{L_a}\Big|_{\Delta x=\|\vec{r_i}-\vec{r_j}\|} = \left(\frac{r_{0,(x_i,y_i)}}{r_{0,(x_i,y_i)}+\|\vec{r_i}-\vec{r_j}\|}\right) \tag{3.28}$$

with	L_{ij}	- the (i,j)-th matrix element of the amplitude loss matrix L,
	$r_{0,(x_i,y_i)}$	- the equivalent source radius of the i-th mesh element (see equation (3.22)),
	N	- the total number of nodes in the FE mesh,
	$\vec{r_i}$	- the position vector to the i-th mesh element (source),
	$\vec{r,j}$	- the position vector to the j-th mesh element (sink).

For a mesh of N nodes, the amplitude loss matrix L contains $N\times N$ elements.

A wave radiated at the time t_0 affects certain nodes after propagating for a time step Δt as shown in figure 3.19. Therefore, a time-dependent amplitude loss matrix $L_{\Delta t}$ is created. $L_{\Delta t}$ is the same matrix as L, with the difference, that any matrix element is replaced by zero, if it corresponds to a node, which is not effected by a wave emitted at t_0.

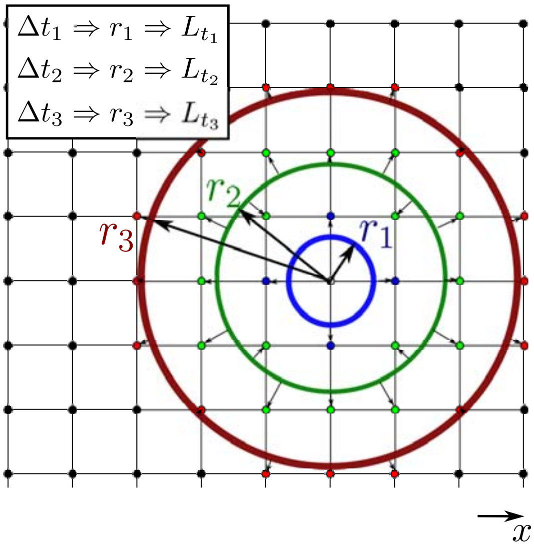

Figure 3.19: Affected nodes by the sound pressure, which is radiated at one specific node for different propagation delays

For the implementation, it is necessary to keep the time-dependent amplitude loss matrix $L_{\Delta t}$ for a defined time interval. Using the maximum distance d_{Max} between two nodes (e.g. the diagonal of a squared CMUT or the diameter of a circular CMUT), $L_{\Delta t}$ has to be kept in the memory for the time $t_{r,max} = d_{Max} \cdot c$. The three-dimensional radiation matrix R represents the collection of the time-dependent amplitude loss matrices:

$$R = \begin{pmatrix} L_{\Delta t}(t0 - t_{r,max}) \\ L_{\Delta t}(t0 - t_{r,max} + \Delta t) \\ L_{\Delta t}(t0 - t_{r,max} + 2\Delta t) \\ \vdots \\ L_{\Delta t}(t) \end{pmatrix}. \tag{3.29}$$

The radiation matrix R has to be updated in any time step, if a non-constant time step is used. However, an implementation based on a lookup-table generated in pre-processing is used, which allows a computational effective realization within the time step integration.

The total sound pressure $p_{res}(t_0)$ at the current time step t_0 is the superposition of all elementary waves. This is calculated multiplying the pressure change $\Delta_t p$ of all previous time steps with the corresponding time-dependent amplitude loss matrix $L_{\Delta t}$. The vector notation in equation (3.30) represents the collection of the scalar sound pressure present at the different nodes of the FE mesh. For a mesh with N nodes, $\vec{p}_{res}$ becomes a vector $\vec{p}_{res} = \mathbb{R}^N$, where the n-th element in represents the scalar sound pressure amplitude at the n-th mesh element.

$$\vec{p}_{res}(t_0) = \sum_i \Delta_t \vec{p}(t_i) L_{\Delta t}(t_0 - t_i) \in \mathbb{R}^N \tag{3.30}$$

d) Model Validation

The dynamic restoring force on the CMUTs surface due to the structure-fluid interaction can be treated as damping effect and has an impact on the resonance frequency. For different CMUT designs, the resonance frequency has been measured in air and compared to the simulation results achieved by the hybrid model.

In the figure 3.20, the measured resonance frequencies in air, the calculated free eigenfrequency of the corresponding FE-model and the simulated resonance frequency using air as fluid load for the CMUT are shown. The deviation $e_{f,r}$ is the relative difference between the measured and simulated eigenfrequency.

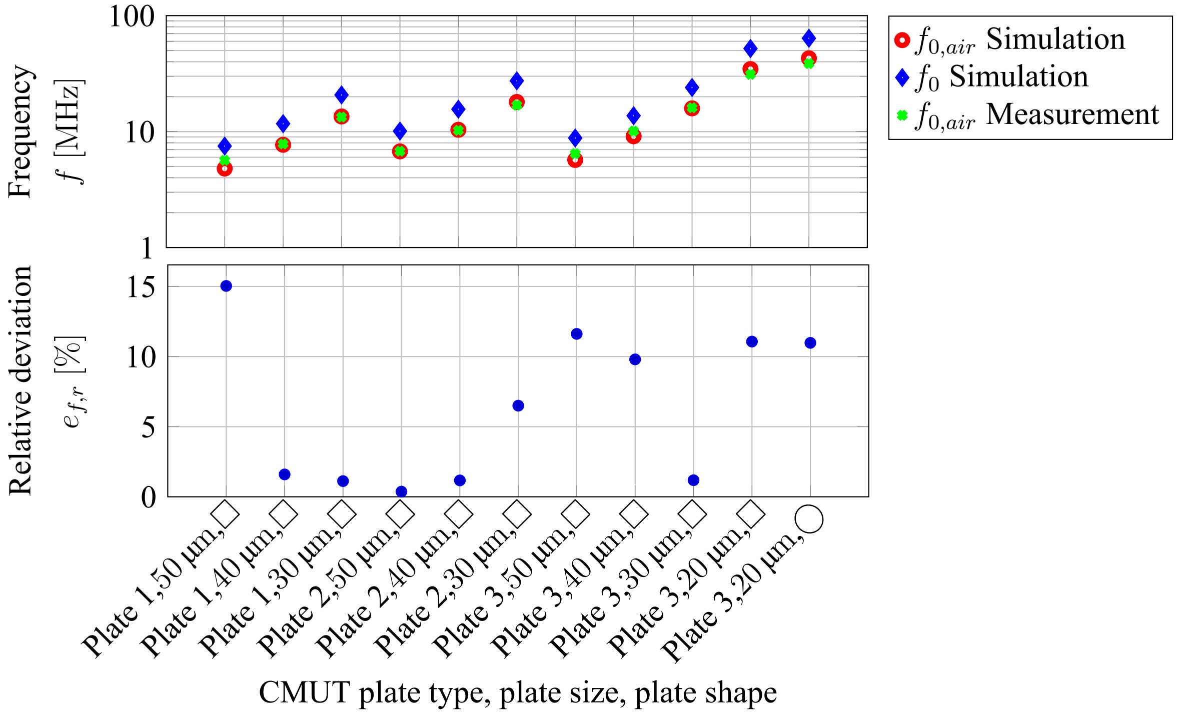

Figure 3.20: Measured and simulated resonance frequencies for different CMUT designs (□ - squared cell design, ◯ - circular cell design; see table A.2).

The maximum deviation between simulated and measured resonance frequency amounts to $15\,\%$. This is a sufficient accuracy, taking the fabrication and measurement uncertainties into account. The best results have been achieved for small plate sizes at low frequencies. Another fact is that for the simulation, the transient response function of the CMUT was calculated, while in the measurement, a stationary sine (sweep) excitation had to be used.

However, the frequency drop between the eigenfrequency of the free plate and the resonance frequency of the damped plate shows the impact of the fluid load and validates the accuracy of the used modeling approach.

3.3.4 Transducer Electronics

The characteristics of a CMUT cell can be simulated by using an ideal voltage source or receive amplifier. However, the displacement of the plate also depends on the connected electronics, because a CMUT is a reversible transducer. This is relevant in both, send and receive operation. The aim is therefore to connect a more realistic circuitry to the CMUT within the time domain simulation. For this work here, an electrical equivalent representation was used.

A CMUT is basically a capacitive load to the connected electrical circuit. Due to the deflection of the CMUT plate, the capacity of the CMUT changes and, depending on the applied voltage, a current flow is created. Thus, the electrical interaction of the CMUT can be described by a time-dependent capacity and a current source as shown in figure 3.21. The voltage drop over the capacitor C_{CMUT} is the voltage creating the electrostatic force within the CMUT cell.

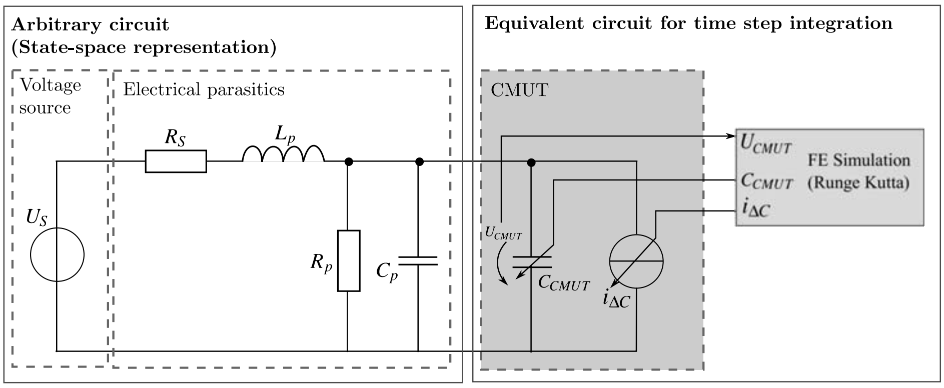

Figure 3.21: Equivalent circuit model of CMUT for time step integration with wave guide circuit and voltage source

To combine the mechanic and electric model of the CMUT, the capacity C_{CMUT} and current source $i_{\Delta C}$ must be formulated as function of the deflection w of the CMUT plate. Therefore, the capacity C_{CMUT} is calculated using the plate capacitor approximation for each mesh element:

$$C_{CMUT}(t) = \varepsilon_0 \sum_i \frac{A_{ij}}{d_{eff} - w_i(t)}. \tag{3.31}$$

L_{ij} - Deflection of the i-th node towards the bottom electrode
w_i - Total number of nodes in the FE mesh
A_i - Corresponding area to the i-th mesh element
d_{eff} - Effective gap height of the CMUT cell

The current flow due to the capacity change depends on the voltage drop U_{CMUT} over the CMUT and on the change of the capacity C_{CMUT}. The capacity change ΔC and the resulting current flow

$$i_{\Delta C}(t) = U_{CMUT}(t)\frac{\Delta C(t)}{\Delta t} \tag{3.32}$$

are calculated within the Runge-Kutta algorithm.

Based on this approach, it is possible in simulation to connect the CMUT to any circuitry, which can be represented by an explicit discrete time-variant state-space circuit, where the CMUT is replaced by a current source and a static capacity.

An example is given in figure 3.21. The CMUT is connected to a voltage source and a wave guide circuit. The corresponding state space equations are derived analytically:

$$\begin{aligned}\begin{pmatrix} i_s(k+1) \\ U_{CMUT}(k+1) \end{pmatrix} &= \begin{pmatrix} -\frac{R_s}{L_p} & -\frac{1}{L_p} \\ -\frac{1}{C_p+C_{CMUT}(k)} & -\frac{1}{R_p(C_p+C_{CMUT}(k))} \end{pmatrix} \cdot \begin{pmatrix} i_s(k) \\ U_{CMUT}(k) \end{pmatrix} \\ &+ \begin{pmatrix} 0 & \frac{1}{L_p} \\ -\frac{1}{C_p+C_{CMUT}(k)} & 0 \end{pmatrix} \cdot \begin{pmatrix} i_{\Delta C}(k) \\ U_S(k) \end{pmatrix}, \end{aligned} \tag{3.33}$$

$$U_{CMUT}(k) = \begin{pmatrix} 0 & 1 \end{pmatrix} \cdot \begin{pmatrix} i_s(k) \\ U_{CMUT}(k) \end{pmatrix} + \begin{pmatrix} 0 & 0 \end{pmatrix} \cdot \begin{pmatrix} i_{\Delta C}(k) \\ U_S(k) \end{pmatrix}. \tag{3.34}$$

In summary, the electrical representation, the structure-fluid interaction including the radiation matrix and the equation of movement are implemented into the Runge-Kutta algorithm and allow a complete physical simulation of a CMUT cell including drive and read-out electronics.

3.4 Design Optimization

It is not possible to derive an optimal CMUT design for a given application by analytical means as described in section 3.3. The reason is the nonlinear characteristic of the CMUT cell discussed in section 3.2. Thus, the simulation model is run within an optimization loop tuning the design parameters until the best cell design is achieved. Within this section, the structure and application of an evolutionary optimization algorithm for CMUTs is described, before the result of an exemplary design optimization run is explained.

3.4.1 Evolutionary Optimization for CMUT

The design optimization is performed using an evolutionary optimization algorithm. This approach can handle local minima due to its stochastic characteristic, what is important because of the nonlinear behavior of the CMUT.

In order to use the evolutionary optimization, the CMUT design parameters (genes) are parametrized and several designs (individuals) are simulated. Thereby, a fitness parameter is calculated for each individual. The genes are optimized by the algorithm in order to create an individual with a maximum fitness, which represents the CMUT design with the best performance.

The design optimization consists of three steps:

1. Parametrization of the CMUT model
2. Definition of a fitness parameter
3. Configuration and running the optimization algorithm

In the first step, the genes, which shall be optimized, have to be specified. The most important variables are plate size, plate thickness and gap height. Other possible genes are material parameters or the fluidic load (matching layers). In order to achieve a result in short time, the design-space has to be limited to a defined range of values. This can be either a continuous range or a number of discrete values. All possible combinations create the gene pool. The smaller the gene pool is, the faster an optimization result is achieved.

To evaluate the performance of an individual, a scalar fitness parameter must be introduced. The higher the fitness is, the better matches the corresponding individual to the aimed target. In case of a CMUT, it is reasonable to extend the algorithm to use hard and soft fitness indicators. A soft indicator could be for instance the gain-bandwidth product, the send sensitivity, the receive sensitivity, the fractional bandwidth or the peak sound pressure. Soft fitness indicators always result in a fitness parameter greater than zero and thus a valid individual. Especially for CMUTs, it is useful to also implement hard fitness parameters. They represent cases, where the fitness of an individual degrades to zero. An example for such a hard indicator is, when the device is already pulled in at atmospheric pressure without any bias voltage.

After defining the genes and fitness parameters, the optimization algorithm needs to be configured. The main parameters are the number of individuals within a generation and the amount of generations to process. The more individuals are given within a generation, the lower is the risk of not finding the global maximum for the fitness, but the higher is the computation time to obtain the fittest individual.

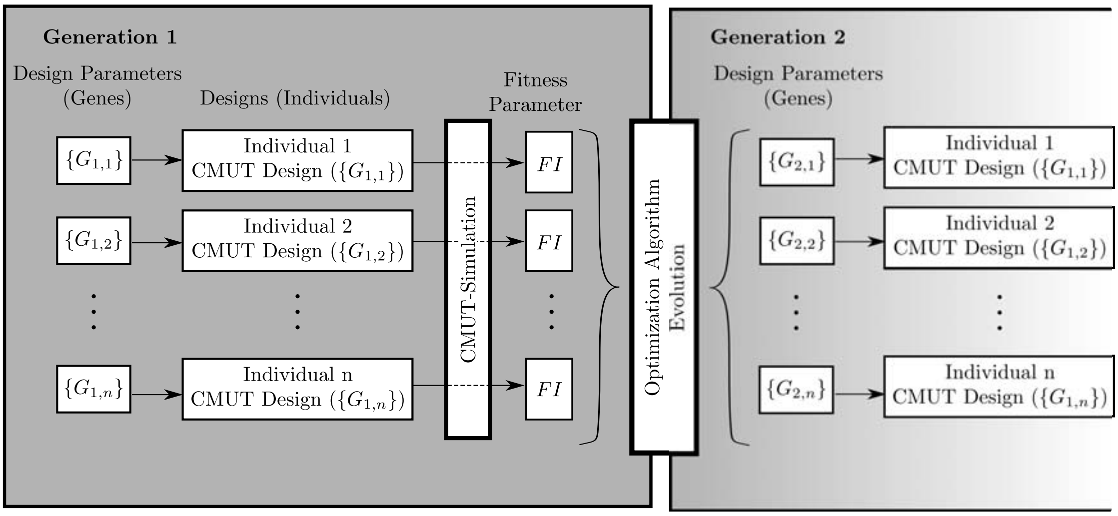

Figure 3.22: Structure of the implemented evolutionary optimization algorithm

3.4.2 Exemplary Optimization Result

As an example for such an optimization procedure, the search for the best CMUT cell design for a high frequency medical sonography application will be presented. The operating range is predetermined by the application from $f_{O1} = 5\,\mathrm{MHz}$ to $f_{O2} = 15\,\mathrm{MHz}$. The AC drive voltage is limited due to present CMOS driver specifications and have to be rectangular pulses with a predetermined amplitude of $U_{AC} \leq 30\,\mathrm{V}$. The maximum DC bias voltage is set to $U_{DC} = 100\,\mathrm{V}$. The target of the optimization run is a CMUT design, which allows to generate the highest possible signal-to-noise ratio for the acquired sonography picture. The input signal for the CMUT is predetermined and the resulting sound field of the transducer is only affected by the arrangement of the individual cells. So, the receive signal amplitude remains as the only optimization parameter. The higher the resulting receive signal amplitude is, the better is the signal to noise ratio and accordingly image quality and penetration depth. Thus, the aim is to find an optimized CMUT design, which provides the highest spectral receive signal amplitude over the operation frequency range for the preset excitation voltage signal.

In order to achieve a CMUT design operating within the whole specified frequency range (see figure 3.23 a)), two restrictions are used: The center frequency f_m of the CMUT in immersion has to lay within the desired operating frequency range (figure 3.23 b)):

$$f_{O1} \leq f_m \leq f_{O2}. \tag{3.35}$$

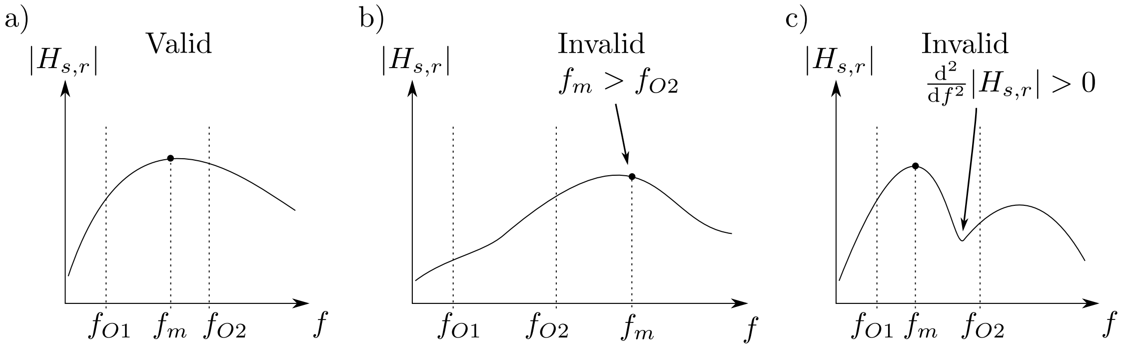

Figure 3.23: Effect of the restrictions (hard indicators) for the send-receive transfer function on the individual fitness within an optimization run.

If the condition for f_m in equation (3.35) is not fulfilled, the CMUT will either vibrate in a higher eigenmode or operate as static actuator. Both modes are inefficient for generating and sensing ultrasonic signals in relation to an excitation of the first resonant eigenmode. The corresponding designs are declared as invalid by the first restriction and a fitness value of zero is dedicated (hard indicator).

Antiresonances in the CMUT transfer function within the operation range have to be avoided. At an antiresonance the CMUT cannot generate or detect any ultrasonic signal. This fact results in a local minimum of the magnitude of the send-receive transfer function $|H_{s,r}|$ (figure 3.23 c)):

$$\frac{\mathrm{d}^2}{\mathrm{d}f^2}|H_{s,r}(f_{O1} \leq f \leq f_{O2})| \leq 0. \tag{3.36}$$

Both conditions (equations (3.35) and (3.36)) are used as hard indicator and result in a fitness value of zero, which rejects an individual (CMUT design) completely. Valid individuals have to be compared and rated against each other by a fitness parameter. Here, the receive signal $|\underline{I}_r(f)|$ shall be maximized within the operation frequency range for the preset drive signal amplitude U_{AC}. Therefore, the send sensitivity $\underline{H}_s$ is calculated within the optimization loop by simulating the radiated sound pressure signal $p_s(t)$ in the center of the CMUT using the specified AC drive signal $U_{AC}(t)$.

$$\underline{H}_s(f) = \frac{\mathcal{F}\{p_s(t)\}}{\mathcal{F}\{U_{AC}(t)\}} \tag{3.37}$$

The receive sensitivity $\underline{H}_r(f)$ is derived by simulating the current flow i_{CMUT} at the CMUT for an incoming ultrasonic sound pressure signal $p_r(t)$. To increase the stability of the solver and avoid singularities in the receive sensitivity, the shape of the sound pressure signal was set to a Gaussian pulse instead of using the previous calculated send sound pressure as this ensures a high stability of the time-step integration algorithm.

$$\underline{H}_r(f) = \frac{\mathcal{F}\{i_{CMUT}(t)\}}{\mathcal{F}\{p_r(t)\}} \tag{3.38}$$

The receive signal can now be calculated from the send-receive transfer function $\underline{H}_{s,r}(f)$:

$$\underline{I}_r(f) = \mathcal{F}\{U_{AC}(t)\} \cdot \underline{H}_s(f) \cdot \underline{H}_r(f) = \mathcal{F}\{U_{AC}(t)\} \cdot \underline{H}_{s,r}(f). \tag{3.39}$$

Within the optimization loop, the drive signal was a rectangular pulse with a $-6\,\mathrm{dB}$ cut-off frequency $f_{-6dB} > f_{O2}$. Together with the hard indicator defined by equation (3.36), the minimum of the spectral receive current $\underline{I}_r(f)$ within the operation frequency range is located either at the lower boundary f_{O1} or at the upper boundary f_{O2}. So, the spectral receive current $\underline{I}_r(f)$ needs to be calculated at f_{O1} and f_{O2} only in order to evaluate the worst-case scenario. To additionally consider the increasing ultrasonic attenuation over the frequency in tissue, the receive current was weighted with a factor of 1 at f_{O1} and 0.25 at f_{O2}. Out of this methodology, a fitness indicator FI_1 is created:

$$FI_1 = \min\left\{\frac{|\underline{I}_r(f_{O1})|}{1}, \frac{|\underline{I}_r(f_{O2})|}{4}\right\} \tag{3.40}$$

Within a transducer many CMUTs are arranged to operate in parallel. The resulting receive current $|\underline{I}_r|$ is the superposition of the receive signals of connected CMUT cells. This has to be addressed by involving the CMUT cell area as a second fitness indicator FI_2:

$$FI_2 = \frac{1}{(a_s + d_m)^2}. \tag{3.41}$$

In between the cells, a small margin for the anchor of the plate needs to be considered. In this example, the cell margin d_m is set to 2 µm per cell.

The resulting fitness indicator FI is the product of FI_1 and FI_2 and can be interpreted physically as minimum spectral receive current per transducer area (receive intensity):

$$FI = FI_1 \cdot FI_2 = \min\left\{\frac{|\underline{I}_r(f_{O1})|}{1}, \frac{|\underline{I}_r(f_{O2})|}{4}\right\} \cdot \frac{1}{(a_s + d_m)^2}. \tag{3.42}$$

As design parameters to be optimized by the algorithm (genes), the plate dimension d_s, plate core thickness d_p and gap height d_g were used. These three parameters allow to tune the resonance frequency, the mechanical impedance of the CMUT plate and the pull-in voltage.

The parameter range of all genes was set based on fabrication experience on the CMUT fabrication process (see table A.3).

The optimization loop was run for 51 generations with 50 individuals in each generation. In total 2550 individuals (designs) have been evaluated and 2391 of them fulfill all hard indicators. The average simulation time was $56\,\mathrm{s}$ per individual on a laptop computer[2].

All calculated gene values are shown in figure 3.24 as function of the generation. By analyzing individual gene values (gap height, plate dimension, plate thickness), the convergence of the optimization algorithms can be evaluated. Already after 10 generations, a clear trend towards the final design appears for all genes. The fitness achieved in the 10th generation is $88\,\%$ of the maximum fitness after 51 generations. Figure 3.24 also shows clearly, that all three genes are important and have to be optimized. This is caused by the fact that individuals are present, which have a low fitness value, even if only one gene is not close to the optimal value.

The resulting design parameters achieved for the individual with the highest fitness FI are:

- Plate dimension $d_s\ = 28\,\mu\mathrm{m}$
- Plate core thickness $d_p\ = 694\,\mathrm{nm}$
- Gap height (vacuum) $d_g\ = 83\,\mathrm{nm}$

All signal and simulation parameters are listed in table A.3.

---

[2] Laptop Lenovo Edge E530 (3259a3g), manufactured in 2012, Intel Core i5-53210M, 8GB RAM, Windows 7 x64, MATLAB R2015b x64, without multicore support, without parallelization, without using the graphics processing unit (GPU)

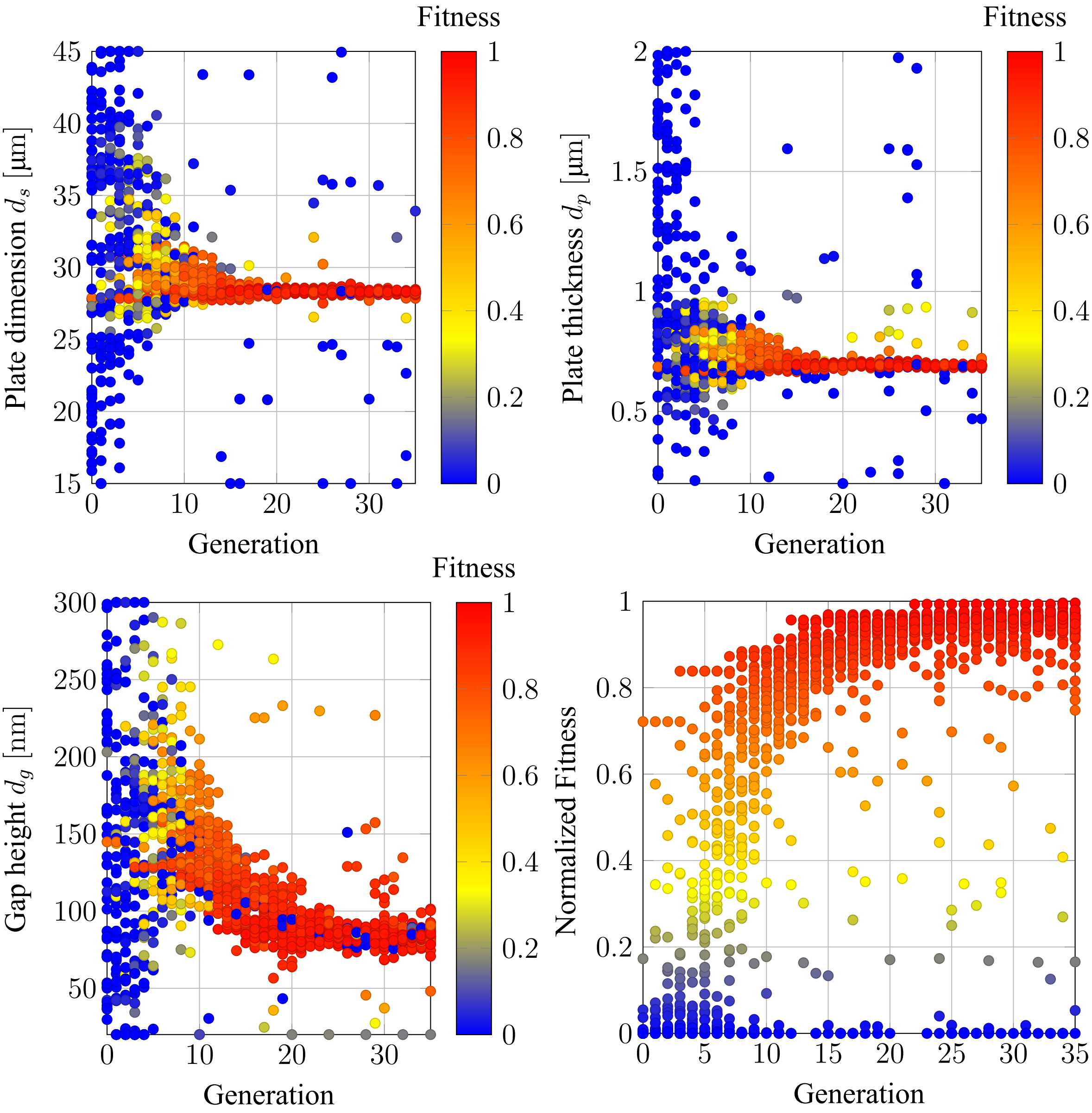

Figure 3.24: Genes (plate dimension, plate core thickness and gap height) vs. generation within the optimization loop. The color indicates the fitness value of the corresponding gene triplet.

Chapter 4

Acoustic CMUT Characterization

4.1 Goal and Methods

The CMUT fabrication process consists of a large number of steps having geometric tolerances and material variances. Both impact the resulting characteristics of the produced transducer. For that reason, the acoustic characteristics of the individual CMUTs have to be determined. Thus, it is recommended to investigate and verify the expected characteristics of the CMUT by acoustic measurements.

As discussed in chapter 3, the send- and receive sensitivity are the most decisive parameters of a CMUT. They can be determined from the drive signal and the emitted sound pressure or the receive signal and the incident sound pressure, respectively. In a CMUT array element, many CMUTs are operating in parallel. In send operation, the created sound field depends on the CMUT cell design and on the arrangement of the individual CMUT cells. To study the effect of the cell design on the acoustic characteristics, the impact of the sound field generated by the cell arrangement has to be removed. Therefore, a procedure has been developed to measure the send and receive sensitivity of a CMUT cell by correcting a measured hydrophone signal based on the present sound field.

For all measurements, a comparable setup was used, which is described in section 4.2. In section 4.3 sound field scanning results are compared to a sound field simulation. Based on the sound field, a frequency-dependent amplitude correction factor is created. This parameter is used to transform the measured signal shape of a full transducer populated with many CMUTs to the signal emitted by a single CMUT cell. Using the determined sound field correction factor, the send sensitivity can be investigated further as shown in section 4.4. Whereas section 4.5 explains the measurement of the receive sensitivity.

4.2 Basic Measurement Setup

4.2.1 Overview on the Setup

All measurements shown in this work used an acoustic setup as it is shown in figure 4.1. The drive signal for the CMUT is created by a signal generator (Agilent 33250A) and amplified using an E&I 325LA power amplifier. To amplify the CMUT receive signal, a linear $40\,\mathrm{dB}$ signal amplifier (Cividec C1) is used. The DC bias voltage for the CMUT is applied from a Keithley K236 source measurement unit. The sound pressure was measured by a needle hydrophone mounted on a $x-y-z$ translation stage. Drive signal, CMUT receive signal and hydrophone receive signal were acquired by an oscilloscope (LeCroy WaveRunner Zi66) and directly transferred to a host computer. A software for controlling all devices and processing the measured signals was implemented in Matlab. A detailed list of the equipment used is provided in table B.1.

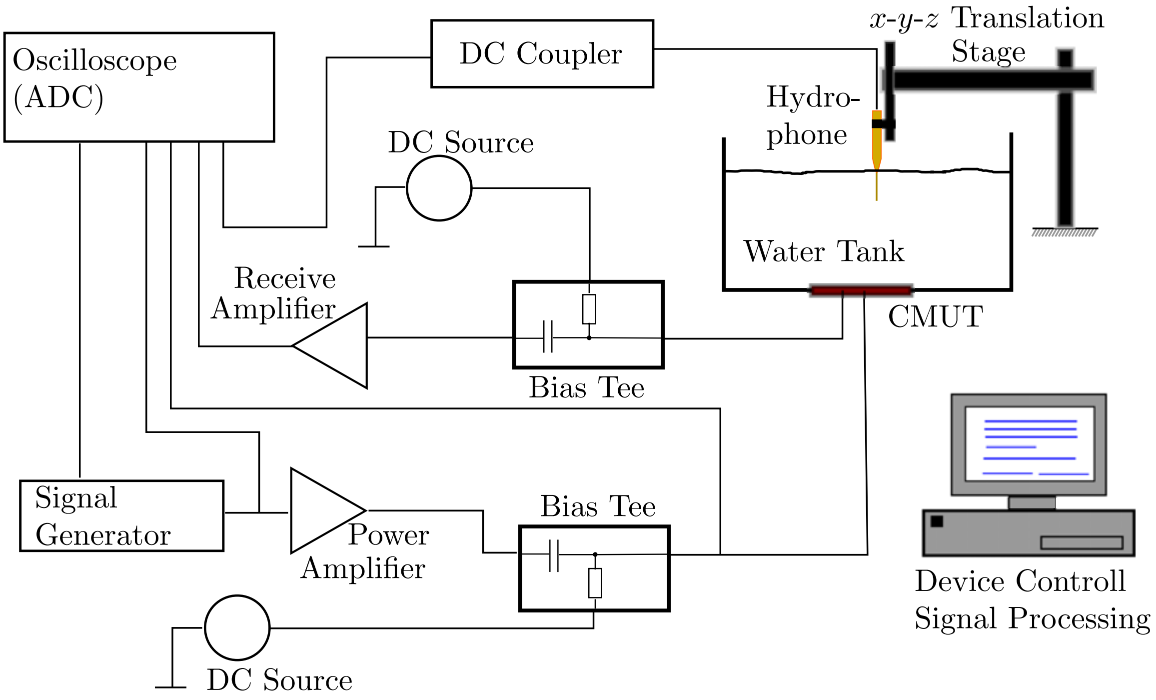

Figure 4.1: Measurement setup for the characterization of CMUT chips

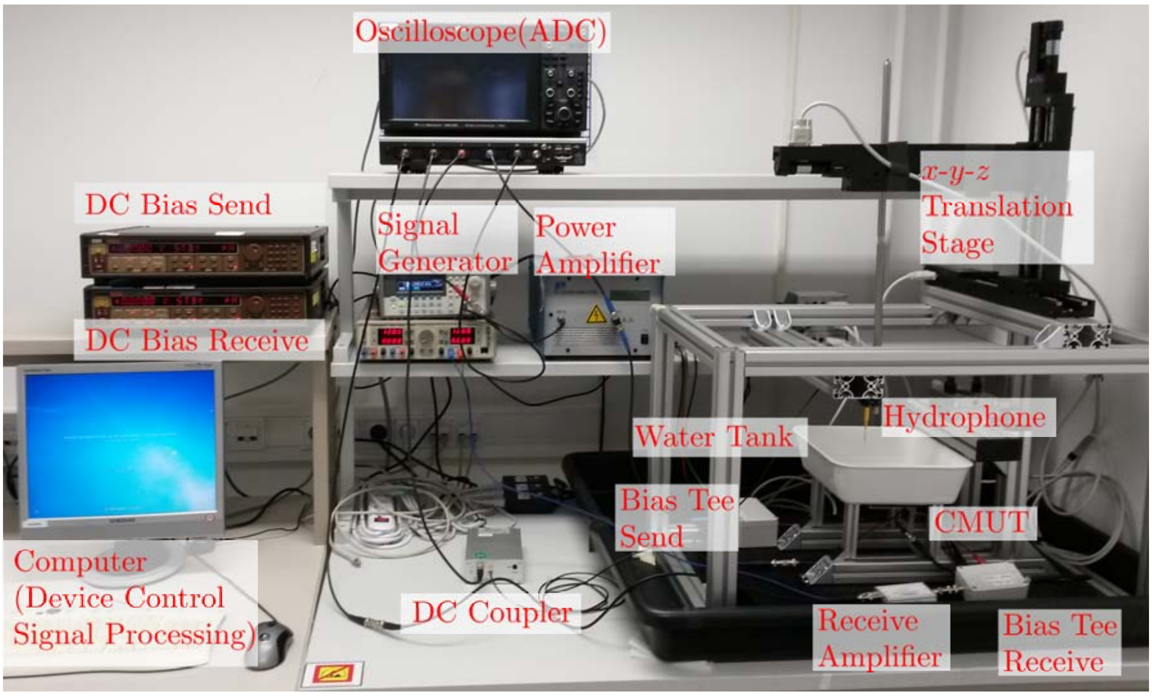

Figure 4.2: Setup to measure the sound of packaged CMUT chips in immersion (see also table B.1)

4.2.2 Hydrophone

To measure the sound pressure in immersion a needle hydrophone was used for three reasons:

- The omnidirectional directivity[1] is important for the sound field scanning as it is not necessary to rotate the hydrophone.
- The tip is small and allows a high spatial resolution, when scanning a sound field.
- The thin needle also allows an integration into a reflector which it necessary to measure the receive sensitivity as shown in section 4.5.

In particular, a Precision Acoustics needle hydrophone[2] was used with a tip diameter $0.5\,\mathrm{mm}$. The hydrophone including preamplifier is calibrated in a frequency range from 1 to $30\,\mathrm{MHz}$ and has a nominal sensitivity of $600\,\mathrm{mV/MPa}$.

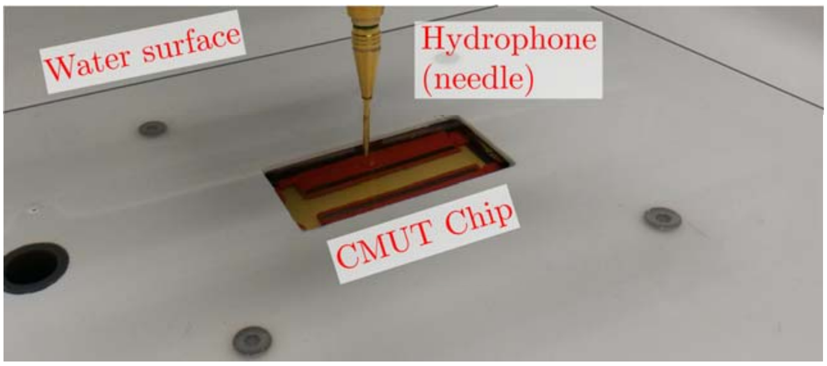

Figure 4.3: Needle Hydrophone and CMUT immersed in deionized water

4.2.3 Power Amplifier

To drive the CMUT elements with arbitrary AC signals, a signal generator (Agilent 33250A) was connected to a power amplifier (E&I 325LA). As the capacity of the CMUT elements and the capacity of the mounting and connections are in the range of pF to nF, the limiting factor for the drive signal is not the bandwidth of the amplifier but the deliverable current.

The maximum number of array elements N_{max}, which can be driven by the power amplifier using a continuous sine signal at a frequency f with an amplitude U_{AC} is estimated from the capacitive load.

---

[1] A capsule hydrophone from Onda Corp. (type HGL-0085) also offers a nearly omnidirectional directivity, but a small sensitivity in comparison to the used needle hydrophone.

[2] See also table B.1

The capacitive load C_{amp} for the amplifier is the capacity of the connected CMUT array elements capacity C_{el} and the capacity of the socket mount C_{soc} for each channel. In addition, the parasitic capacity C_{con} of the connectors between the amplifier and the socket mount has to be added. For N connected CMUT array elements, the capacitive load C_{amp} becomes

$$C_{amp} = N \cdot (C_{el} + C_{soc}) + C_{con}. \tag{4.1}$$

Assuming a sinusoid drive signal with the amplitude U_{AC} connected to the capacity C_{amp}, the necessary power P can be calculated by

$$\frac{1}{2\pi f C_{max}} = \frac{{}^{U_{AC}}/_{\sqrt{2}}}{I_{RMS}} = \frac{P}{\left({}^{U_{AC}}/_{\sqrt{2}}\right)^2}. \tag{4.2}$$

For a given amplifier power P_A, the maximum capacity C_{max}, which can be driven by the amplifier, becomes

$$C_{max} > \frac{P_A}{\left({}^{U_{AC}}/_{\sqrt{2}}\right)^2 \cdot 2\pi f} = \frac{P_A}{U_{RMS}^2 \cdot 2\pi f}. \tag{4.3}$$

The maximum number N_{max} of CMUT array elements is then

$$N_{max} < \left(\frac{P_A}{\left({}^{U_{AC}}/_{\sqrt{2}}\right)^2 \cdot 2\pi f} - C_{con} \right) \cdot (C_{el} + C_{soc})^{-1}. \tag{4.4}$$

The maximum number N_{max} of CMUT array elements, which can be driven by the power amplifier in parallel, is depicted in figure 4.4 as function of the drive voltage amplitude and frequency.

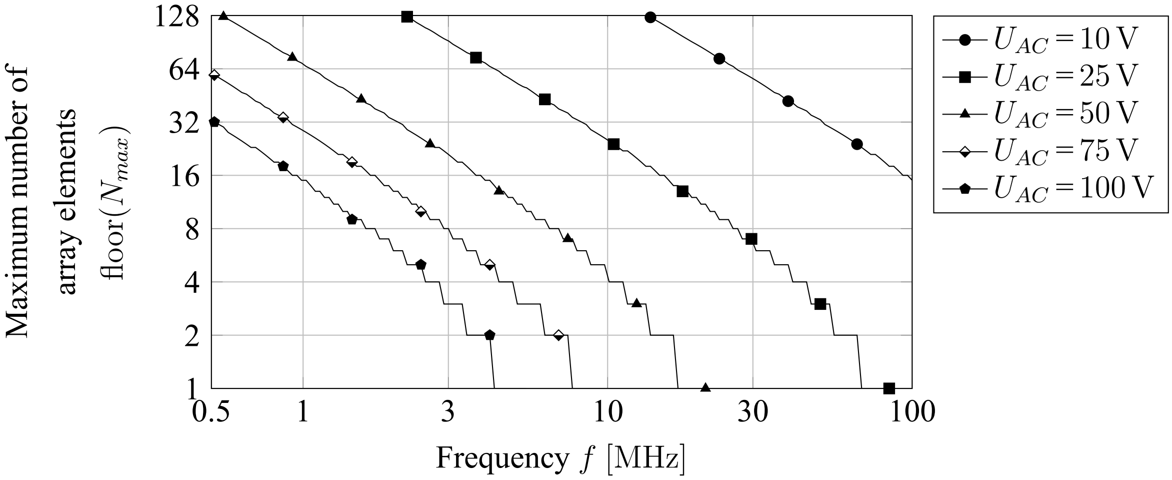

Figure 4.4: Maximum number of array elements N_{max} which can be driven by a $25\,\mathrm{W}$ amplifier (continuous sine signal) vs. frequency

- Capacity of one CMUT element [3] $C_{el} = 35\,\mathrm{pF}$
- Capacity of the chip socket per connected array element $C_{soc} = 10\,\mathrm{pF}$
- Capacity of the connectors $C_{con} = 100\,\mathrm{pF}$
- Power of the amplifier $P_A = 25\,\mathrm{W}$

4.2.4 CMUT Drive Signal

The full transmit potential of a CMUT can only be used when a suitable drive signal is applied. Commercially available integrated ultrasound driving ICs and ASICs designed to drive CMUTs deliver drive signals with rectangular pulse shape. The reason for this is the electronic implementation as push-pull circuit, which is less complicated in comparison to a digital-analog converter and a linear power amplifier.

For this reason, rectangular pulses are also used here as drive signal for the send and receive measurements. Optimized drive signals as presented in [Sav+15] where the second harmonic excitation is minimized by using trapezoid signals are not considered here.

The rectangular drive signal can be characterized by its pulse width t_{PW}, the rise time t_r and the fall time t_f (see figure 4.5). Here the rise time t_r is the time, when the voltage level rises from $0.1U_{AC}$ to $0.9U_{AC}$. The fall time t_f is defined accordingly for the falling edge. The value of the pulse width t_{PW} depends on the rise time, the fall time and the switch delay t_e, when the status changes from charging to discharging the capacitive load:

---

[3] Carrier including CMUT according to impedance measurements

$$U(t) = \begin{cases} 0 & \text{for } t \leq 0 \\ U_{AC} \cdot \left(1 - e^{\frac{t}{\tau_r}}\right) & \text{for } 0 < t \leq t_e \\ U_{AC} \cdot \left(1 - e^{\frac{t_e}{\tau_r}}\right) \cdot e^{\frac{t-t_e}{\tau_f}} & \text{for } t > t_e \end{cases} \tag{4.5}$$

$$\tau_r = \frac{t_r}{\ln(0.9)} \quad , \quad \tau_f = \frac{t_f}{\ln(0.9)} \tag{4.6}$$

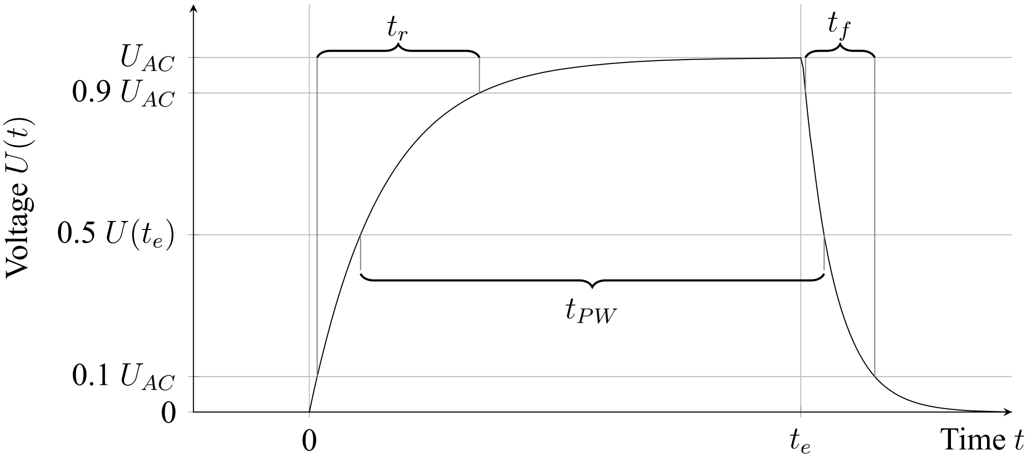

Figure 4.5: Pulse shape of a rectangular signal according to equation (4.5)

The CMUT shall be exited over the full bandwidth, thus the pulse shape is analyzed in frequency domain. Here, the Fourier transformed $\mathcal{F}\{U(t)\}$ is calculated analytically and results in a complex term:

$$\underline{U}(\omega) = jU_{AC} \left(\frac{1 - e^{-j\omega t_e}}{\omega} + \frac{\tau_r \left(e^{-\frac{t_e}{\tau_r} - j\omega t_e} - 1\right)}{\tau_r\, \omega - j} - \frac{\tau_f\, e^{-j\omega t_e} \left(e^{-\frac{t_e}{\tau_r}} - 1\right)}{\tau_f\, \omega - j} \right). \tag{4.7}$$

It is difficult to directly extract conclusions from equation (4.7) , except the fact that the spectral amplitude is directly proportional to the drive voltage U_{AC}. The second and third fraction in equation (4.7) indicate, that further simplification is possible if the rise time t_r equals the fall time t_f, which is reasonable for an ideal amplifier:

$$\underline{U}_{sym}(\omega) = \underline{U}(\omega)\Big|_{\tau_r=\tau_f=\tau} = U_{AC} \frac{1 - e^{-j\omega t_e}}{j\omega - \tau\omega^2}. \tag{4.8}$$

There are two significant values for the magnitude of the amplitude spectrum: the equivalent DC offset (spectral amplitude at $\omega = 0\,\mathrm{Hz}$) and the $-6\,\mathrm{dB}$-cut-off frequency f_{-6dB}. The DC component can be calculated analytically:

$$\lim_{\omega \to 0} \left| \underline{U}_{sym}(\omega) \right| = U_{AC} \cdot t_e. \tag{4.9}$$

In contrast, the cut-off frequency has to be solved numerically. In figure 4.7, the $-6\,\mathrm{dB}$ cut-off frequency f_{-6dB} is shown as function of the rise (and fall) time $t_r = t_f$ and the switch delay t_e and gives an overview for the electronic circuit design. If an amplifier can deliver a minimum rise time and switch time, then the cut-off frequency taken from the plot is the maximum frequency, which the amplifier can drive definitely.

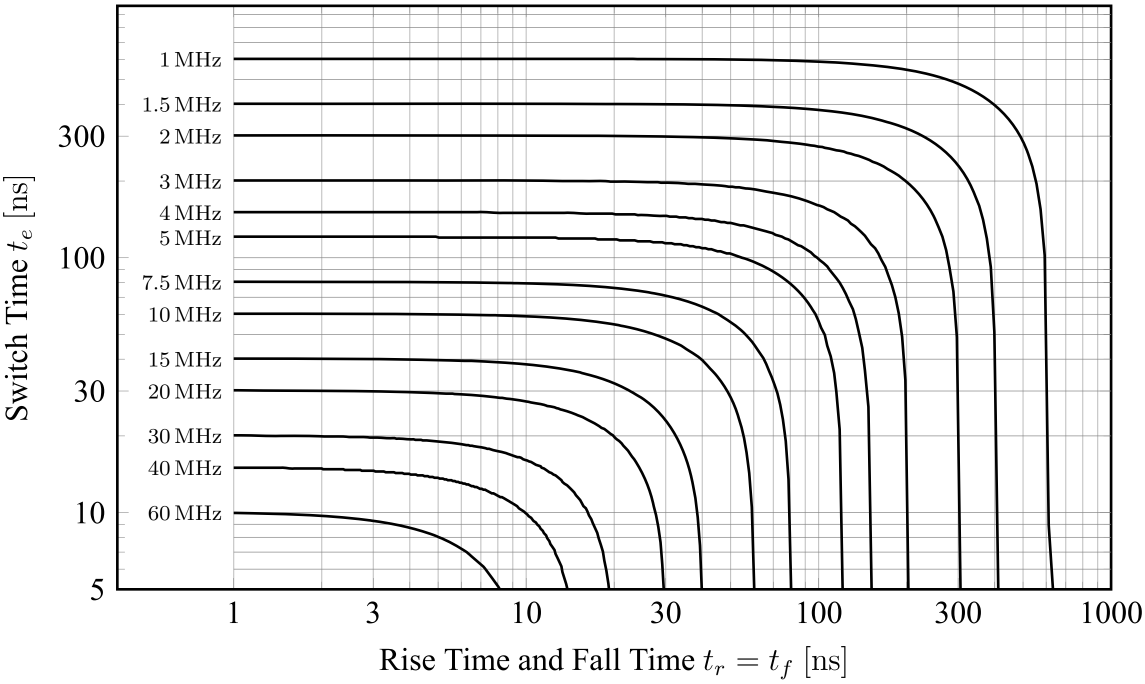

Figure 4.6: Cut-off frequency f_{-6dB} vs. switch time t_e and rise/fall time $t_r = t_f$ for a rectangular pulse shape with exponential rising and falling edges

In general, the aim is to keep the switch time t_e as long and the rise time t_r as short as possible, on condition that the cut-off frequency f_{-6dB} of the signal is bigger than the highest pursued transmit frequency.

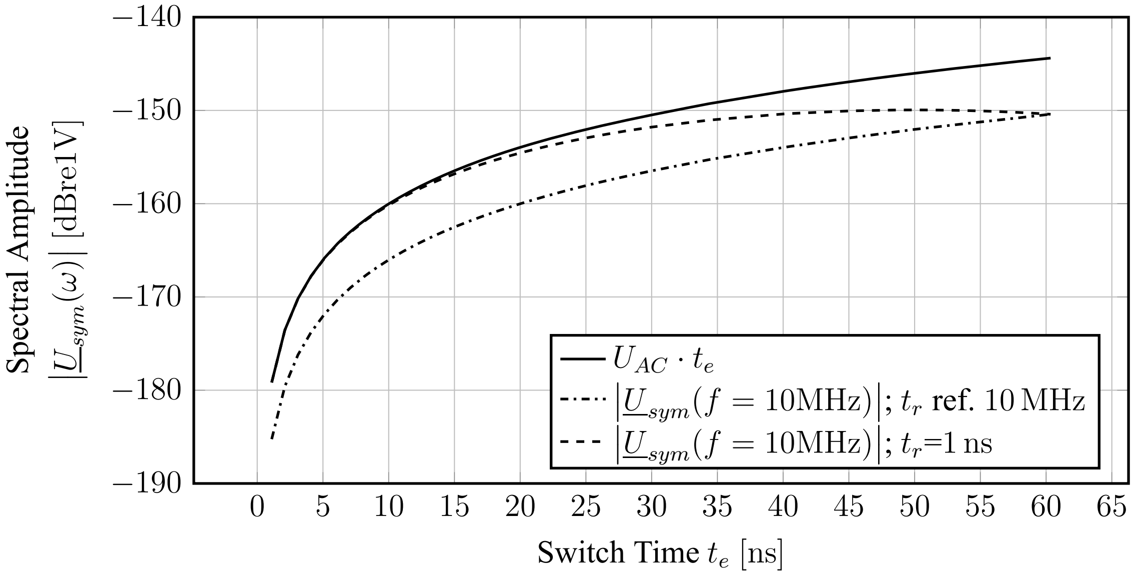

Figure 4.7: Spectral amplitude gained vs. switch time t_e for $t_r = t_f$ and $U_{AC} = 1\,\text{V}$

In figure 4.7 the spectral amplitude at $f = 0\,\text{Hz}$ is shown as function of the switch time t_e (solid line). The dashdotted line follows the rise time/switch time combination of figure 4.6 within the $10\,\text{MHz}$ line and is consequently $6\,\text{dB}$ below the maximum amplitude at $f = 0\,\text{Hz}$ for any switch time. The dashed line shows the dependence of the spectral amplitude at $10\,\text{MHz}$ on the switch time t_e for a rise time t_r of $1\,\text{ns}$. It becomes clear, that the spectral amplitude of the signal is mainly dominated by the switch time t_e. Further improvement is possible, if the rise time t_r is reduced. Additionally, a short rise and fall time results in a more constant spectral amplitude over the frequency range.

In conclusion, the following properties for a drive signals of rectangular pulse shapes with exponential rising and falling edges should be targeted:

1. The cut-of frequency of the pulse must be higher than the smallest used transmit frequency according to figure 4.6.
2. The switch time shall be as long as permissible.
3. The rise time shall be as short as permissible.

4.3 Sound Field Correction

A sound field analysis is essential in the development of (application-specific) transducers or the experimental validation of beamforming algorithms. Thereby, the sound field of a transducer is either simulated numerically or measured by sound field scanning. As basis for the measurement of the acoustic send- and receive characteristics of a CMUT cell design, the knowledge about the sound field allows the generation of a sound field correction factor. This parameter removes the impact of the interference pattern on the hydrophone signal. This enables to calculate the shape of the sound pressure signal on the CMUT's surface from a sound pressure measurement performed in the far field of the CMUT.

4.3.1 Setup and Alignment

For sound field measurement, the experimental setup shown in figure 4.1 is used. The receive path is not connected, as no receive signal is sensed by the CMUT. The hydrophone is mounted on a linear stage [4] with a unidirectional repeatability of $1\,\mu\mathrm{m}$.

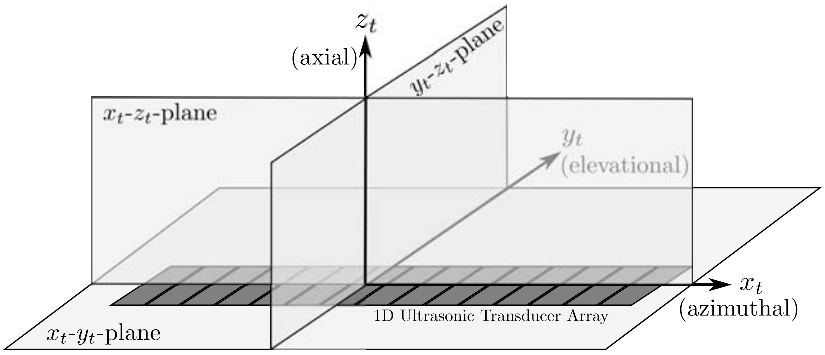

Figure 4.8: Transducer coordinate system for acoustic measurements

At the beginning, the coordinate system of the translation stage (x_s, y_s, z_s) and the coordinate system of the transducer (x_t, y_t, z_t) have to be aligned (figure 4.9). A subjective mechanical arrangement is not sufficient, as the position has to be determined with an accuracy in the range of $100\,\mu\mathrm{m}$. Therefore, the position of the hydrophone is determined in relation to the array by the sound field. The outer array elements are driven with a short transient signal (one half sine cycle) to suppress side lobes. The hydrophone is moved in the x_s-y_s-plane over the first array element until the maximum sound pressure is measured. This point defines the coordinate S_1. The propagation time t_{s1} from the CMUT array element to the hydrophone is measured as the time difference between trigger impulse from the signal generator and the

---

[4] Physik Instrumente (PI) GmbH&Co. KG, Type M-403.8DG, range $200\,\mathrm{mm}$

peak of the sound pressure. Now, the procedure is repeated for the array element on the other side of the transducer. Thereby also the z_t-coordinate needs to be varied until the propagation times t_{s1} and t_{s1} equal: $t_{s1} = t_{s2} = t_{s1,2}$. This defines the coordinate S_2.

Now, it is possible to align the transducer and the stage coordinate system except the elevational rotation (rotation around the x_t axis). Thus, a third point S_3 is obtained by searching for the maximum sound pressure in the x_s-y_s-plane at another z_s coordinate.

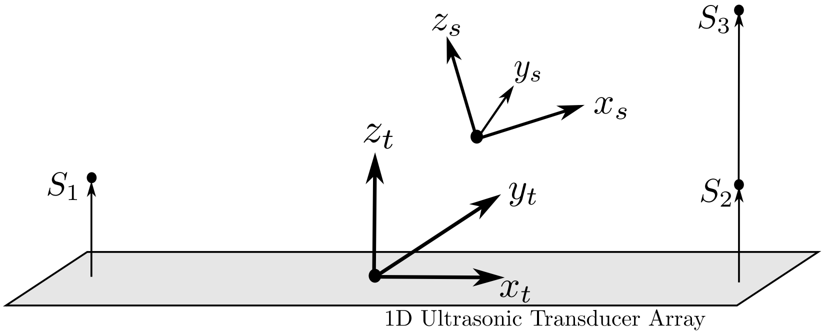

Figure 4.9: Alignment of the coordinate systems of the transducer and the x-y-z-stage

From those three points S_1, S_2 and S_3 it is possible to calculate the tilt angles α between the transducer coordinate system and the stage coordinate system:

$$\alpha_x = \arctan\left(\frac{y_{S3} - y_{S2}}{z_{S3} - z_{S1}}\right), \tag{4.10}$$

$$\alpha_y = \arctan\left(\frac{z_{S2} - z_{S1}}{x_{S2} - x_{S1}}\right), \tag{4.11}$$

$$\alpha_z = \arctan\left(\frac{y_{S2} - y_{S1}}{x_{S2} - x_{S1}}\right). \tag{4.12}$$

The rotational transformation matrix $T^S_{T\,rot}$ from the transducer coordinate system to the stage coordinate system is

$$T^S_{T\,rot} = \begin{pmatrix} 1 & 0 & 0 \\ 0 & \cos(\alpha_x) & -\sin(\alpha_x) \\ 0 & \sin(\alpha_x) & \cos(\alpha_x) \end{pmatrix} \begin{pmatrix} \cos(\alpha_y) & 0 & \sin(\alpha_y) \\ 0 & 1 & 1 \\ -\sin(\alpha_y) & 0 & \cos(\alpha_y) \end{pmatrix} \begin{pmatrix} \cos(\alpha_z) & -\sin(\alpha_z) & 0 \\ \sin(\alpha_z) & \cos(\alpha_x) & 0 \\ 0 & 0 & 1 \end{pmatrix}. \tag{4.13}$$

The translational transformation matrix $T^S_{T\,trans}$ is the distance vector from the origin $\mathcal{O}_t$ of the transducer coordinate system to the origin $\mathcal{O}_s$ of the stage coordinate system:

$$T^S_{T\,trans} = \mathcal{O}_s - \mathcal{O}_t = \frac{1}{2}\left(\vec{r}_{S1} - \vec{r}_{S2}\right) + \Delta z \cdot \vec{e}_z. \tag{4.14}$$

An absolute reference between both systems is in axial direction is contrivable, as the speed of sound c can be calculated from the sound propagation delay in between S_2 and S_3:

$$c = \frac{\|\vec{r}_{S3} - \vec{r}_{S2}\|}{t_{s3} - t_{s1,2}}. \tag{4.15}$$

Then the distance Δz in axial direction becomes

$$\Delta z = c\, t_{S1,2}. \tag{4.16}$$

Now, the full transformation from the transducer coordinate system (x_t, y_t, z_t) into the stage coordinate system (x_s, y_s, z_s) can be written as

$$(x_s; y_s; z_s) = T^S_{T\,rot} \cdot (x_t; y_t; z_t) + T^S_{T\,trans} \tag{4.17}$$

In the measurement, the target coordinates are set in the transducer coordinate system and converted into the stage coordinate system. The resulting coordinates are the destinations for the x,y,z linear stage.

For the shown alignment procedure, two conditions have to be fulfilled.

- The tilt angle α between the two coordinate systems should be smaller than $15°$ in order to get a valid maximum sound pressure in the x-y-plane.
- The positions S_1, S_2 and S_3 are measured in the main lobe of the sound field of the corresponding array element.

4.3.2 Sound Field Simulation and Measurement

a) Sound Field Simulation

The beam pattern of an ultrasonic transducer mainly depends on the aperture and the signal frequency. Individual CMUT cells are usually small compared to the wavelength of the radiated sound pressure signal. To achieve the necessary aperture size, every CMUT array element consists of many CMUT cells located next to each other. Thus, the sound field of the transducer is determined by the arrangement of the individual cells and the sound pressure signal generated by the individual CMUT.

In most applications, the CMUT cell is small compared to the wavelength of the ultrasonic signals transmitted. This fact allows to simulate the sound field of an array element by replacing each CMUT by a monopolic point source. The resulting sound pressure is the superposition of the signal emitted by all point sources. For continuous sine excitation, the result can be calculated efficiently numerically from

$$p_{sim}(f,\vec{r}) \sim \left| \sum_{i=1}^{N} \frac{q_0 \cdot e^{-jk\|\vec{r}-\vec{s}_i\|}}{\|\vec{r}-\vec{s}_i\|} \right| . \qquad (4.18)$$

$\vec{r}$ - Position vector to computation point

$\vec{s_i}$ - Position vector to i-th sound source

q_0 - Acoustic source strength

k - Wavenumber $k = \frac{2\pi f}{c}$

N- Number of sound sources

b) Sound Field Measurement

Replacing every CMUT by a point source is a big simplification which shall be verified by measurement results. Thus, the sound field of four neighboring array elements, driven in parallel, was measured using a sine burst with four cycles. Between the drive circuitry and the hydrophone, electrical crosstalk appears and creates a receive signal, which is several orders of magnitude higher than the actual hydrophone signal. Thus, no continuous excitation signal, but a burst signal can be used for driving the CMUT.

In addition, the measurement control automatically adapts the oscilloscope scale to the hydrophone signal. Only with this procedure, accurate measurements are possible, because the measured sound pressure amplitude varies extremely for different hydrophone positions.

The drive signal and the measured sound pressure signal in a distance of $5\,\mathrm{mm}$ in front of the array elements are shown in figure 4.10. The signals in figure 4.10 validate the fact that the CMUT is transmitting ultrasound into water in respect to the applied drive signal. But there are more effects to consider for the understanding of the relation between drive and hydrophone signal. First of all, the drive signal shall be investigated: The signal generator delivers an almost ideal sine burst to the power amplifier. Due to signal discontinuities at the beginning and end of the sine burst, the electrical load and feedback of the CMUT, the power amplifier is not able to reproduce the input signal without mutilation.

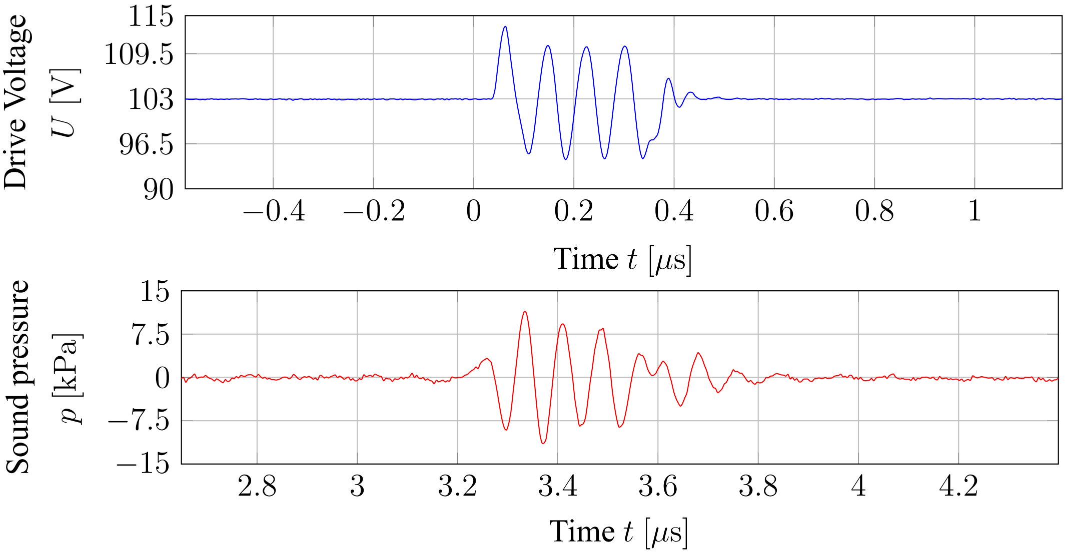

Figure 4.10: CMUT drive signal and hydrophone signal at the hydrophone position $P_T = (-15.5\,\mathrm{mm}; 0\,\mathrm{mm}; 5\,\mathrm{mm})$, which is centralized $5\,\mathrm{mm}$ in front of the active array element; pull-in voltage $U_{PI} \approx 180\,\mathrm{V}$

In addition, the voltage measured by the oscilloscope does not necessarily represent the actual potential difference between the two plates of the CMUT. A positive sound pressure correlates to an overpressure, which is created by the CMUT, when the bendable plate is moving away from the bottom electrode. In the beginning of the sine burst, the hydrophone senses a positive pressure before a local minimum is reached even though the applied voltage increases. This allows the conclusion that the potential difference in between the electrodes of the CMUT drops due to the high current flow in the beginning of the AC signal.

Afterwards, three full sine cycles and the post pulse oscillation generated by the CMUT are apparent in the sound pressure signal. The signal is also affected by the acoustic interference pattern created by the superposition of all waves emitted by the different CMUT cells within the active array element.

Based on the number of 4 sine cycles, the drive signal creates a radiation pattern with the main lobe and two side lobes. Higher order side lobes are suppressed substantially, because only three full sine cycles are available for interference as the hydrophone signal in figure 4.10 indicates.

c) Comparison between Measurement and Simulation

A sound field measurement in the x-z-plane over four array elements was done. The hydrophone was moved in steps of $100\,\mu m$ in each direction and the sound pressure at each point was measured. Figure 4.11 shows the result of the experiment.

The result of the simulation is normalized to the maximum measured sound pressure, which allows to compare the simulation and measurement result as shown in figure 4.11.

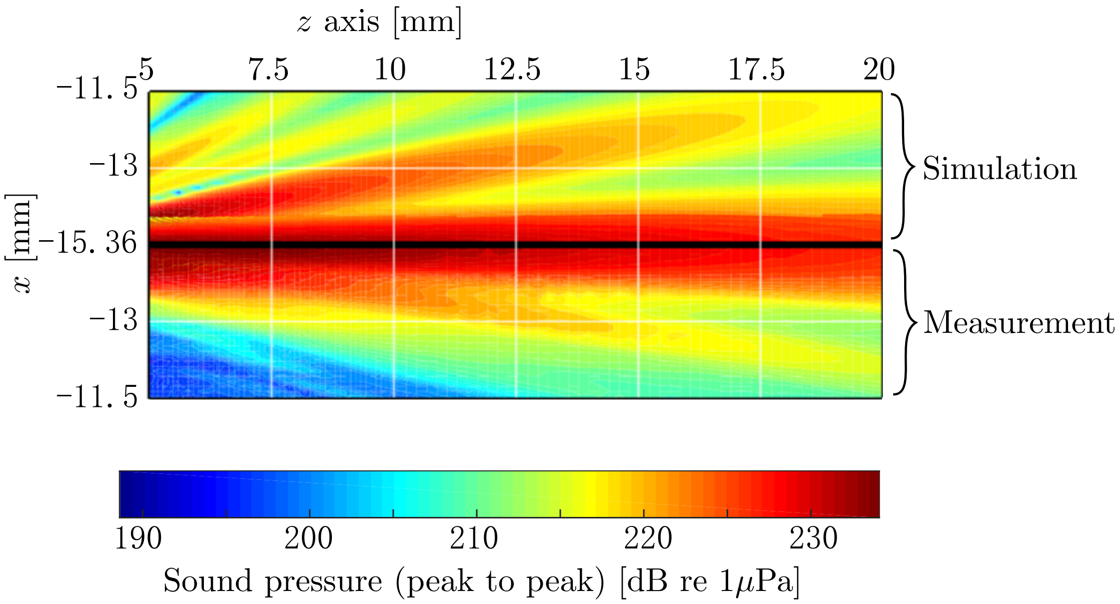

Figure 4.11: Sound field of four array elements at 12 MHz (measurement and simulation)

The agreement between measurement and simulation is acceptable, despite only monopolic sound sources instead of a distributed CMUT model were used for simulation. In the measurement, especially the second side lobe appears smaller and more attenuated than expected by the simulation. One reason for this is the drive signal shape used in the measurement as discussed in paragraph b). A second influencing factor is the hydrophone itself. The hydrophone needle, which was used for the measurements, has a tip size of $500\,\mu m$. This means, that the signal measured and assigned to the recent coordinate is the average sound pressure over a circular area in the x-y-plane around the coordinate.

This measurement procedure can be used to visualize acoustic diversities in between two or more array elements. If the measurement result does not match to the simulation or is not symmetric, this is a major indication that some CMUT cells or a full array element are not working properly.

4.3.3 Generation of the Sound Field Correction Factor

To determine the send- or receive sensitivity for a CMUT cell design, the sound pressure on the surface of the individual CMUT must be measured. However, it is not possible to position the hydrophone closer than $1...2\,\mathrm{mm}$ to the CMUT, because then electric crosstalk between the CMUT plate and the hydrophone needle superposes the hydrophone receive signal. As the wavelength of the ultrasonic signal at frequencies higher than $1\,\mathrm{MHz}$ is short in comparison to the minimum hydrophone distance possible, the measured sound pressure is affected by interference effects. Thus, the sound pressure depends on the hydrophone position and on the signal frequency. The aim is to find a correction factor transforming the measured hydrophone signal to the sound pressure on top of an individual CMUT cell.

Therefore, the sound pressure along the z_t for one single array element was simulated using equation (4.18) to evaluate the dependency between the sound pressure and the hydrophone distance to the transducer at different frequencies. The result is a frequency- and location-dependent sound pressure amplitude, which is created by N monopolic sources (figure 4.12). Each source represents one individual CMUT cell with a concentrated source power q_0.

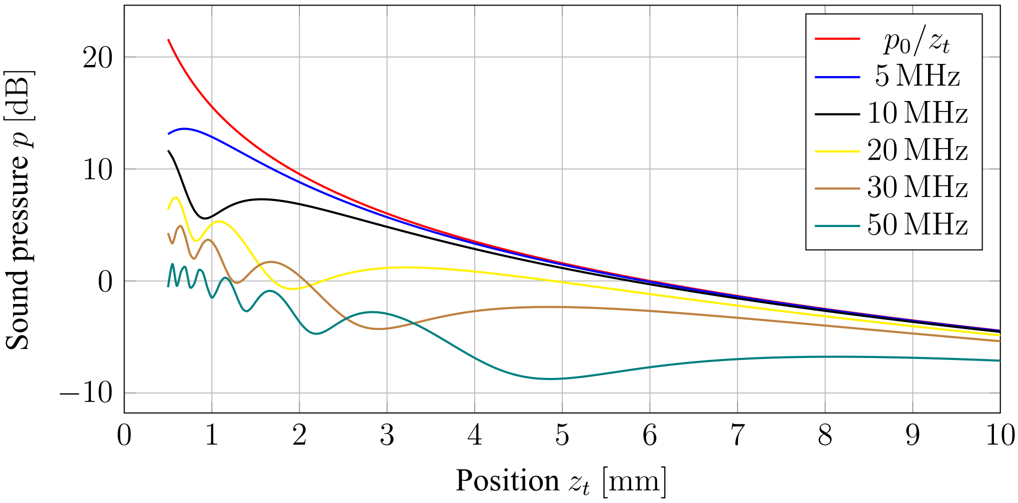

Figure 4.12: Simulation of the sound pressure of one array element in the z_t-axis for different frequencies according to equation (4.18).

In the simulation, the source power q_0 is set independent from the frequency. Thus, the change of the sound pressure amplitude at a given location appears only due to interference effects of the acoustic waves emitted by each point source. This allows to introduce a correction factor, which removes the effect of the interference pattern.

For generating the correction factor, the sound pressure at a location z_0 is calculated including the phase information $p(f, z_0)$ and excluding the phase information $p_{ref}(z_0)$ based on equation (4.18)

$$p(f, z_0) \sim \left| \sum_{i=1}^{N} \frac{e^{-jk\|\vec{r}-\vec{s}_i\|}}{\|\vec{r}-\vec{s}_i\|} \right| , \tag{4.19}$$

$$p_{ref}(z_0) = p(f, z_0)\Big|_{f\,=\,0\mathrm{Hz}} \sim \left| \sum_{i=1}^{N} \frac{1}{\|\vec{r}-\vec{s}_i\|} \right| . \tag{4.20}$$

Here, $\vec{r}$ represents the position vector with the coordinates $\vec{r} = (0;\, 0;\, z_0)$ and $\vec{s_i}$ is the position vector to the center of the i-th CMUT cell. The sound field correction factor $K_p(f, z_0)$ is the transfer function between $p_{ref}(z_0)$ and $p(f, z_0)$.

$$K_p(f, z_0) = \frac{p(f, z_0)}{p_{ref}(z_0)} = \left| \sum_{i=1}^{N} \frac{e^{-jk\|\vec{r}-\vec{s}_i\|}}{\|\vec{r}-\vec{s}_i\|} \right| \cdot \left| \sum_{i=1}^{N} \frac{1}{\|\vec{r}-\vec{s}_i\|} \right|^{-1} . \tag{4.21}$$

The factor $K_p(f, z_0)$ allows to remove the impact of the interference pattern and, therefore, the arrangement of the CMUTs from a (measured) sound pressure signal. In the far field of the transducer no local minimum or maximum of the sound pressure appears and the correction factor K_p only slightly changes for small distance variations. Using this fact is beneficial for real measurements because then the position accuracy of the hydrophone becomes less critical. The near-field length for a single array element with an aperture of $256\,\mu\mathrm{m}$ x $1.0\,\mathrm{mm}$ radiating at $30\,\mathrm{MHz}$ amounts to circa $5\,\mathrm{mm}$. So, all measurements were done in a distance of $z_0 = 6\,\mathrm{mm}$ from the transducer. Figure 4.13 shows the corresponding correction factor K_p as function of the frequency f.

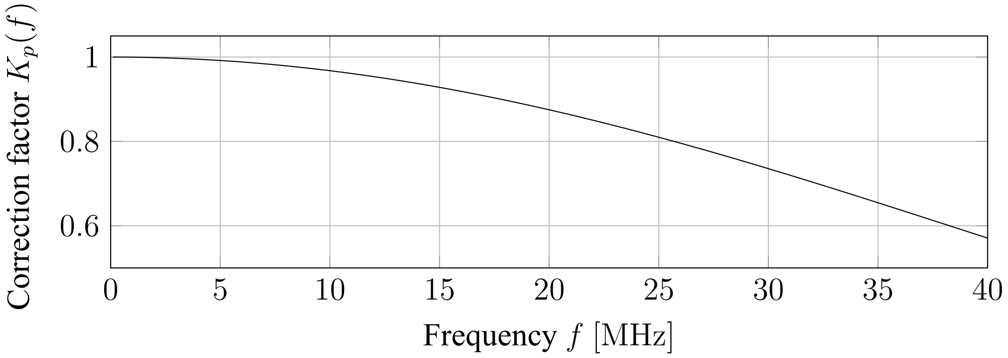

Figure 4.13: Sound field correction factor $K_p(f)$ vs. frequency for a single array element; hydrophone position $z_t = 6\,\mathrm{mm}$.

For small CMUT array element sizes, this correction factor is valid for both, harmonic and transient pulse shapes. The reason is the small phase shift in the hydrophone position. However, for higher accuracy and larger array elements, a more complex sound field simulation using a transient signal is required.

4.4 Send Sensitivity

The send characterization of a CMUT implies the measurement of the send sensitivity. This parameter represents the relation between emitted sound pressure and drive voltage. Therefore, the send sensitivity has to be measured for different drive signals and levels. Additionally, the center frequency and bandwidth can be derived from the send sensitivity.

4.4.1 Measurement Setup

For the measurement of the send sensitivity, the CMUT is immersed and a single array element is driven using a signal generator and power amplifier. A DC bias voltage is applied through a bias tee. The ultrasonic signal emitted by a CMUT is sensed by a hydrophone, which is located in the far field of the CMUT.

As drive signal, a short, transient signal is used, which excites the full spectral bandwidth of the CMUT transducer. In the signal generator, a rectangular pulse with a nominal pulse width of $30\,\mathrm{ns}$ was set to optimally drive the CMUT up to $20\,\mathrm{MHz}$ (figure 4.6). However, the signal still contains energy at higher frequencies and is sufficient for a characterization up to circa $30\,\mathrm{MHz}$.

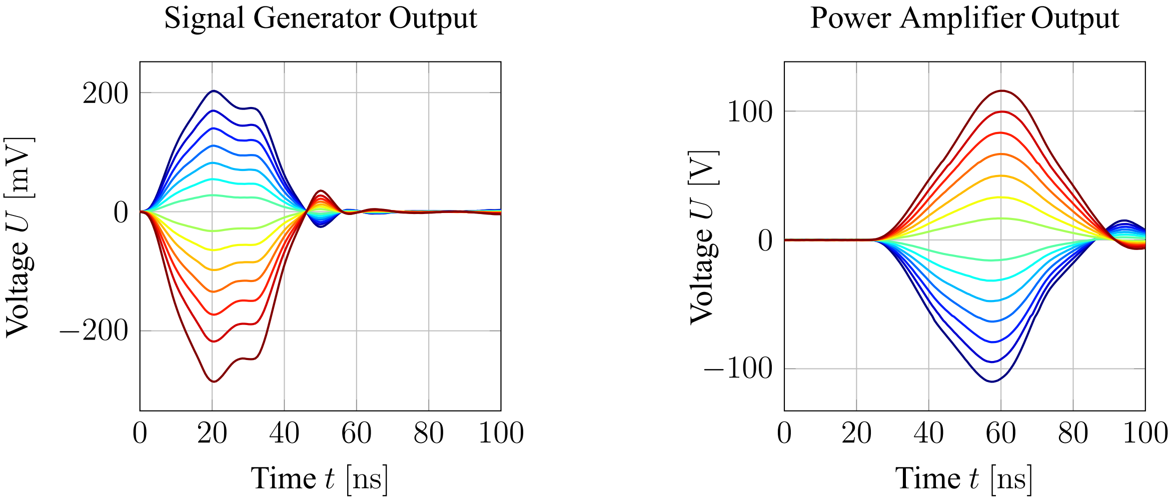

Figure 4.14: Drive signals used to characterize the send sensitivity. Detailed signal characteristics are given in table B.2

.

Due to the nonlinear characteristic of the CMUT, the send sensitivity has to be measured for various AC and DC voltage levels. The time domain drive signals are shown in figure 4.14.

The rise time ($14\,\mathrm{ns}$) and pulse width ($28\,\mathrm{ns}$) were set at the signal generator for all amplitude levels. At the output of the power amplifier, those short timing parameters were not preserved. However, a pulse width of 30-$33\,\mathrm{ns}$ and rise/fall times in the range of 18-$22\,\mathrm{ns}$ achieved at the output of the power amplifier, the drive signal is still useable for the conducted experiments.

The send sensitivity $\underline{H}_s(f)$ of the CMUT is calculated in frequency domain. Therefore, the measured AC drive voltage $U_{AC}(t)$ and the hydrophone voltage signal $U_{Hyd}(t)$ are converted via Fourier transform:

$$\underline{U}(f) = \mathcal{F}\{U_{AC}(t)\}. \tag{4.22}$$

Afterwards, the frequency-dependent hydrophone transfer sensitivity H_{hyd} (calibration, see figure B.1) and the sound field correction factor $K_p(f)$ are applied on the hydrophone voltage. In addition, the sound pressure is divided by the number N of active CMUTs. The resulting sound pressure $\underline{P}(f)$ represents the sound pressure generated by one CMUT in an axial distance of $6\,\mathrm{mm}$ from the array element for the applied drive signal:

$$\underline{P}(f) = \mathcal{F}\{p_{Hyd}(t)\} \cdot \frac{1}{N} = \mathcal{F}\{U_{Hyd}(t)\} \cdot H_{hyd}(f) \cdot K_p(f) \cdot \frac{1}{N}. \tag{4.23}$$

The send sensitivity $\underline{H}_s$ of the CMUT is the ratio between the drive voltage $\underline{U}(f)$ and the spectral sound pressure $\underline{P}(f)$:

$$\underline{H}_s(f) = \frac{\underline{P}(f)}{\underline{U}(f)}. \tag{4.24}$$

4.4.2 Measurement Results

In this section, first the bandwidth B and the center frequency f_m of the send sensitivity $|\underline{H}_s(f)|$ are analyzed in relation to the DC bias voltage U_{DC}. In the next step, also the influence of the AC voltage amplitude U_{AC} and polarization on the bandwidth B is investigated. The last part of this section shows the impact of AC and DC voltage level on the magnitude of the send sensitivity. All measurement results are shown for the CMUT design 1 in table B.4.

a) DC Bias Voltage and CMUT Bandwidth

The lower $-6\,\mathrm{dB}$ cut-off frequency f_{c1} and the upper $-6\,\mathrm{dB}$ cut-off frequency f_{c2} are calculated based on measurements of the send sensitivity $|H_S(f)|$. Both are characteristic parameters for the useable frequency range of a CMUT. Figure 4.15 shows the transfer sensitivity of a CMUT measured at different DC bias voltages at an AC signal amplitude of $20\,\%$ of the pull-in voltage $U_{AC} = 0.2 U_{PI}$. In this measurement, a center frequency f_m in the range of $13\,\mathrm{MHz}$ and a fractional bandwidth of circa $100\,\%$ were obtained.

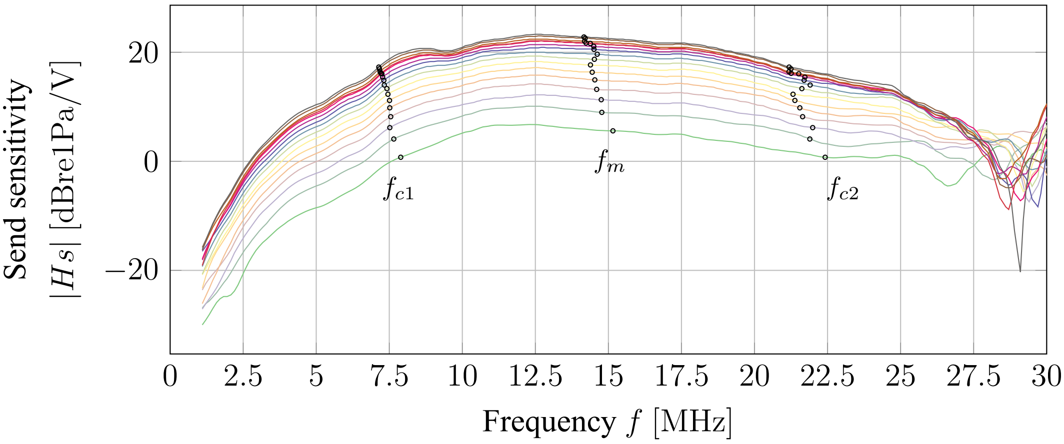

Figure 4.15: Send sensitivity for a single CMUT cell measured at $U_{AC} = 0.2 U_{PI}$ for different DC bias voltages $U_{DC} = \{0.15, 0.2, 0.25, \dots, 0.9\} \cdot U_{PI}$ in a distance of $6\,\mathrm{mm}$.

A more detailed analysis of the cut-off frequencies in relation to the DC bias voltage U_{DC} shows even more relevant effects:

- With increasing the DC bias voltage U_{DC} the lower cut-off frequency f_{c1} decreases and a peak in the sensitivity spectrum at $8\,\mathrm{MHz}$ appears. This characteristic is assigned to surface waves generated due to the periodic arrangement of the CMUTs [AKO14].
- At higher sound pressures, the surface waves exceed the noise level of the hydrophone and contribute to the total signal. The high quality factor of this surface wave is the reason that only a small frequency range near the lower $-6\,\mathrm{dB}$ cut-off frequency is affected. The surface waves do not represent a characteristic of the single CMUT cell itself, because they appear based on the CMUT cell arrangement. For a correct measurement of the cell design-related cut-off frequencies, a low-pass filter can be applied in the spectral domain on the send sensitivity curve to suppress this effect. For the measurement result in figure 4.15, this correction was not necessary.

- With increasing bias voltage, also the spring-softening effect becomes stronger and shifts the resonance frequency of the CMUT towards lower values. This causes also a reduction of the cut-off frequencies. However, this effect affects the absolute bandwidth B only slightly.

b) AC Voltage Amplitude and CMUT Bandwidth

In contrast to the DC bias voltage, the AC signal has a remarkable influence on the bandwidth of the CMUT, as shown in figure 4.16. The lower cut-off frequency is not affected by the AC signal amplitude, but the higher cut-off frequency is increased with rising AC signal amplitude. The reason for this is the nonlinear behavior of the CMUT, which increases with rising AC amplitude. Here, parts of the energy in the drive signal are radiated as ultrasound in a higher harmonic frequency. Due to the high fractional bandwidth in the range of $100\,\%$, the second harmonic and the fundamental mode overlap and shift the upper $-6\,\mathrm{dB}$-frequency to a higher frequency. In consequence, the measured bandwidth of the CMUT increases.

The possible increase of the fractional bandwidth by increasing the AC amplitude amounts to less than $10\,\%$ for this CMUT design. Ideally, the drive signal should be converted into an acoustic signal without nonlinear distortion. Both, the nonlinearity and the requirements on the electric driver circuitry rise with increasing AC voltage amplitude. Therefore, the AC voltage amplitude should be set as low as possible to still achieve the necessary sound pressure amplitude. However, the use of a high AC voltage can be a tool for increasing the transducers bandwidth artificially.

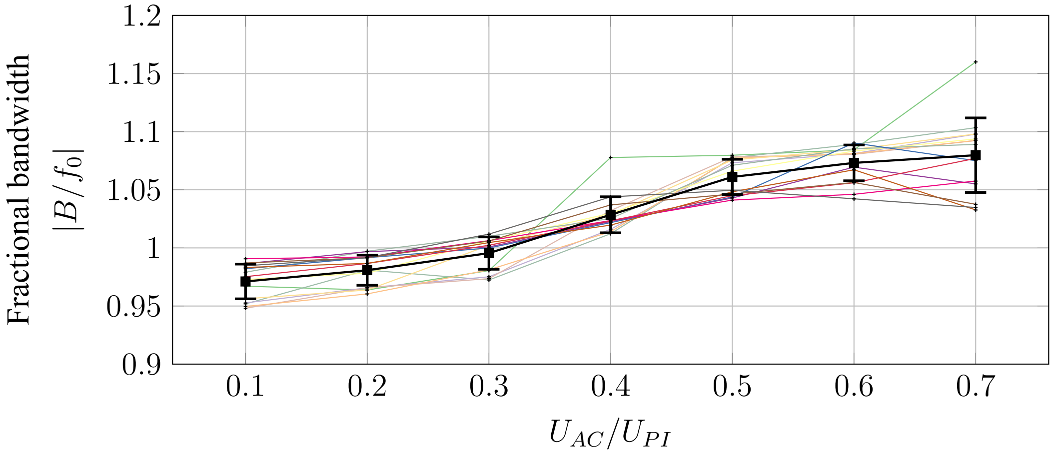

Figure 4.16: Measured fractional bandwidth (send) vs. AC drive voltage at different DC bias voltages $U_{DC} = \{0, 0.05, 0.1, \ldots, 0.9\} \cdot U_{PI}$

c) AC and DC Voltages vs. Sound Pressure Amplitude

The bandwidth is relevant for the characterization of the frequency dependent efficiency of a transducer. But the magnitude of the send sensitivity in the center frequency is important as it directly impacts the absolute signal to noise ratio in an application. Naturally, the magnitude of the send sensitivity increases with rising DC and AC voltages. The send sensitivity of the full drive voltage parameter field is shown in figure 4.18.

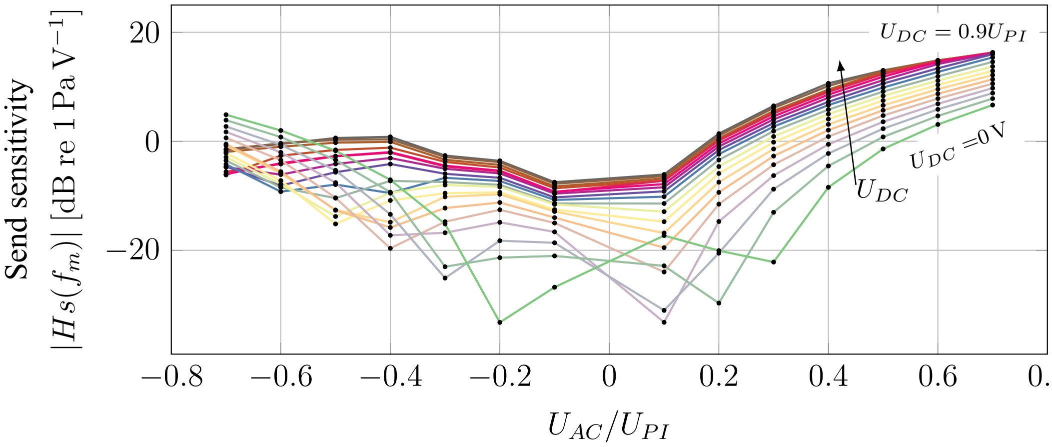

Figure 4.17: Measured send sensitivity H_S at the center frequency f_m vs. AC drive voltage at different DC bias voltages $U_{DC} = \{0, 0.05, 0.1, \ldots, 0.9\} \cdot U_{PI}$

For positive AC voltages, there is a nearly linear relation between the send sensitivity of the CMUT and the DC bias voltage: $H_S(f_m) \sim U_{DC}$. When the AC and DC voltage sum up to a level close to the pull-in voltage, a saturation appears and the sound pressure does not increase further. Applying a positive rectangular pulse to a given positive DC voltage, this saturation effect starts at $U_{DC} + U_{AC} = 1.2U_{PI}$ for the used CMUT design and AC pulse

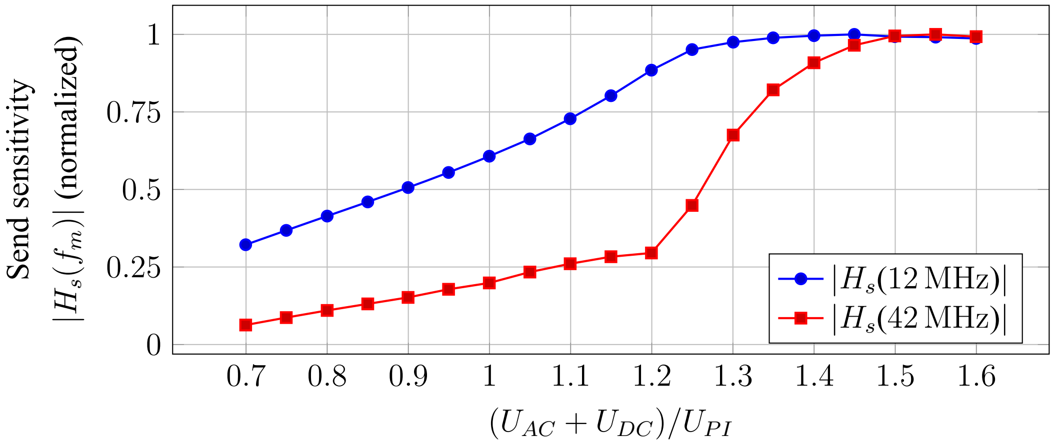

Figure 4.18: Measured send sensitivity in the first and higher-order eigenmodes at $U_{AC} = 0.7U_{PI}$ for different DC bias voltages

timings. At this level, also an abrupt increase of the send sensitivity at a higher eigenmode appears as shown in figure 4.18. This fact indicates that, due to the high electrostatic forces, some CMUTs are pulled in and do not contribute to the sound pressure signal in the first eigenfrequency.

For negative drive pulses, the send sensitivity $|\underline{H}_s(f)|$ also rises with increasing DC bias voltage U_{DC} and AC amplitude U_{AC}. However, the send sensitivity $|\underline{H}_s(f)|$ is smaller in comparison to a positive pulse at the same amplitude. This statement is true, as long as the AC voltage U_{AC} does not overcome the DC bias voltage U_{DC}. Then, the polarization of the voltage changes for a short time and the drive signal characteristic do alter significantly. The reason for this is the quadratic relation between voltage U and electrostatic force F_{el} in the CMUT ($F_{el} \sim U^2$). The send sensitivity is minimized, when $U_{DC} \approx -2U_{AC}$.

In practice, a CMOS drive circuit can handle a defined voltage range $0 \leq U \leq U_{max}$ and supports a DC bias voltage U_{DC} as well as a rectangular AC pulse U_{AC}. The AC and DC drive voltages must not exceed U_{max}, but can be selected arbitrarily apart from the restriction:

$$0 \leq U_{DC} + U_{AC}(t) \leq U_{max}. \tag{4.25}$$

Now, two cases have to be distinguished:

- $U_{max} \geq 1.2U_{PI}$:

The best results in terms of linearity and energy efficiency are obtained, when the CMUT is driven with U_{DC} close to the pull-in voltage U_{PI} and an additional AC pulse, which has the same polarization as the bias voltage (figure 4.17).

- $U_{max} < 1.2U_{PI}$:

In this special case, the use of a positive bias voltage and a negative AC pulse is beneficial. The highest send sensitivity is achieved by setting $U_{DC} = U_{max}$ and applying a negative AC voltage with $U_{AC} = -U_{max}$. This generates the highest sound pressure achievable with this driver, but also a high nonlinear excitation.

4.4.3 Conclusions

In this section, a method has been shown to measure the send sensitivity of a CMUT cell based on a sound field correction factor. This makes the result independent from the arrangement and the amount of CMUT cells transmitting in parallel. Besides the measurement of the absolute send sensitivity of a CMUT design, further parameters such as the bandwidth are analyzed depending on the electrical drive signals. Additionally, recommendations for the optimal drive signal are derived from the experiment.

The most efficient way to drive a CMUT with rectangular pulses is using a DC bias voltage close to the pull-in voltage and an AC pulse with the same polarization as the bias voltage. The AC signal amplitude should be as low as possible to reduce the nonlinear transfer characteristic of the CMUT. For positive rectangular pulses with $U_{AC} > 0.5U_{PI}$, the limit $U_{AC} + U_{DC} \approx 1.2U_{PI}$ should not be exceed, because then CMUTs start pulling in due to the AC drive voltage. The factor 1.2 slightly changes for different signal shapes, AC voltages and CMUT designs.

The fractional bandwidth of the CMUT is not affected by the DC bias voltage significantly. Only a shift in the center frequency f_m appears due to the spring stiffening effect. High AC voltages pretend an increased send sensitivity at high frequencies, which appears due to the generation of higher harmonics based on the nonlinear character of a CMUT.

A deviant scenario appears, when the electronic driver is limited to a maximum voltage which is smaller than the pull-in voltage of the CMUT. In this case, a high positive DC voltage and a negative pulse amplitude result in the highest sound pressure level achievable.

4.5 Receive Sensitivity

The receive characteristics of a CMUT can be characterized by different approaches. In all of them, the CMUT has to be exposed to an ultrasonic signal. In principle two different types of sound sources are useable to provide this ultrasonic signal:

- either a CMUT of the same design as the CMUT to investigate,
- or a different type of ultrasonic transducer (CMUT, piezo, ...).

The aim is to test different CMUT designs with different send/receive sensitivities and frequency ranges in a comparable setup. Therefore, the utilized sound source for the measurement has to cover the whole frequency range of the CMUT under test to be characterized. Due to the high bandwidth of a CMUT, it is complicated or even impossible to find a suitable single sound source. In [Olc+07] three different sources have been used to measure the receive sensitivity of a CMUT transducer. Differences of up to $3\,\mathrm{dB}$ in receive sensitivity $|\underline{H}_r(f)|$ appear at frequencies, where two sources are able to transmit. With this accuracy neither the $-6\,\mathrm{dB}$ bandwidth nor the absolute receive sensitivity of the CMUT can be measured. For this reason, a measurement procedure was developed using the same CMUT design for send and receive operation.

This section first introduces the measurement setup and the send signal as basis for the measurement of the receive sensitivity. Methods for signal conditioning of the receive signal are described to reduce noise in the receive signal. Afterwards, the receive sensitivity of the CMUT is analyzed depending on the incident sound pressure and the DC bias voltage. Finally, the spectral receive bandwidth of the CMUT is evaluated.

4.5.1 Measurement setup

For the measurements, laboratory equipment is used to drive the send CMUT and acquire the receive signal from the CMUT. This allows to characterize and compare several CMUT designs using the same drive and receive measurement chain. An ultrasonic signal is emitted by a single CMUT array element and received by another single array element. Both array elements are in the same sensor die and have the same cell design. The emitted sound pressure wave hits a reflector, is sensed by a hydrophone, which is integrated into the reflector and returns to the receive CMUT as shown in figure 4.19. The reflector is made from plexiglass, because this material is not conductive and does not emit ions into the deionized water. Additionally, its optical transparency facilitates the alignment of the reflector including the hydrophone in relation to the CMUT. The hydrophone is mounted in the reflector to verify the sound pressure emitted by the transmitting CMUT and to increase the accuracy of the measurement. The use of two neighboring array elements - one for send and one for receive operation (pitch-catch principle) supersedes the implementation of a send-receive-switch as it makes the (electrical) setup less complicated.

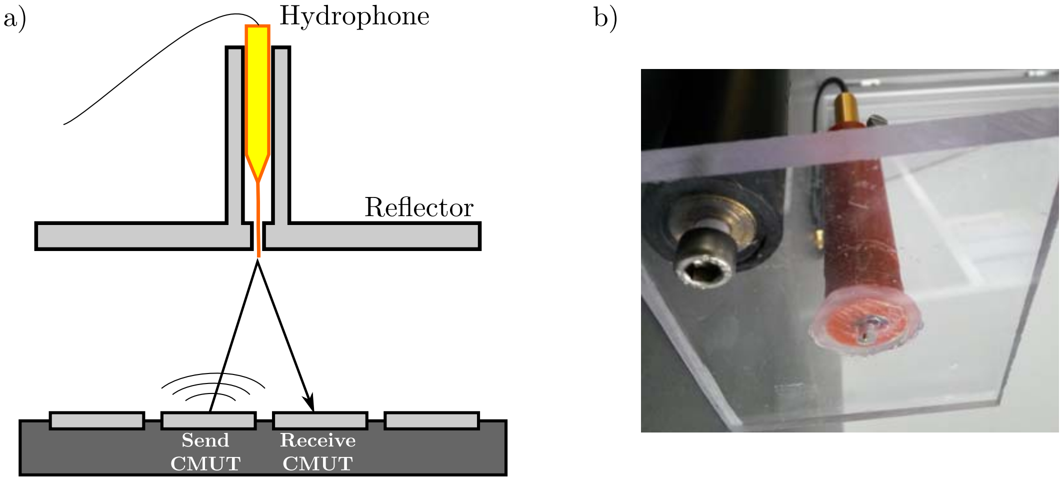

Figure 4.19: a) Setup for pitch catch measurement (not in scale), b) needle hydrophone mounted in the reflector

The details of the measurement setup have been shown in figures 4.1 and 4.2. The send CMUT is driven using a DC source, a signal generator, a power amplifier and a RC bias tee. The receive path consists of a RC bias tee, a DC source and a current amplifier. The amplifier is a $40\,\mathrm{dB}$ linear amplifier operating from $35\,\mathrm{kHz}$ to $2\,\mathrm{GHz}$ with $50\,\Omega$ input and output impedance[5]. For the signal acquisition an oscilloscope is used.

The measurement was performed at different DC bias voltages for both, the send and the receive CMUT. Within the measurement, charging effects appeared in the send as well as in the receive CMUT and varied when the DC bias voltage was changed.

4.5.2 Verification of the Hydrophone Signal Amplitude

The reflector is adjusted in a distance of $6\,\mathrm{mm}$ from the CMUT (see section 4.3.3) until the receive signal of the CMUT becomes maximal. Then the reflector is moved in the x_T-y_T-plane until the hydrophone signal becomes maximal, too. This indicates, that the hydrophone is located in the center in front of the send CMUT.

Figure 4.20 shows the drive signals with and without connected receive path on the neighboring CMUT array element. The drive signal is slightly affected by additional electrical

---

[5] The current amplifier cividec type C2 is denoted with a lower cut-off frequency of $1\,\mathrm{MHz}$ but was customized by the manufacturer to operate above $35\,\mathrm{kHz}$

parasitic capacities, introduced by bias tee, DC source and current amplifier to the neighboring CMUT array element. A negative overshoot appears in the signal and the rising edge is distorted, but the amplitude and general shape are kept.

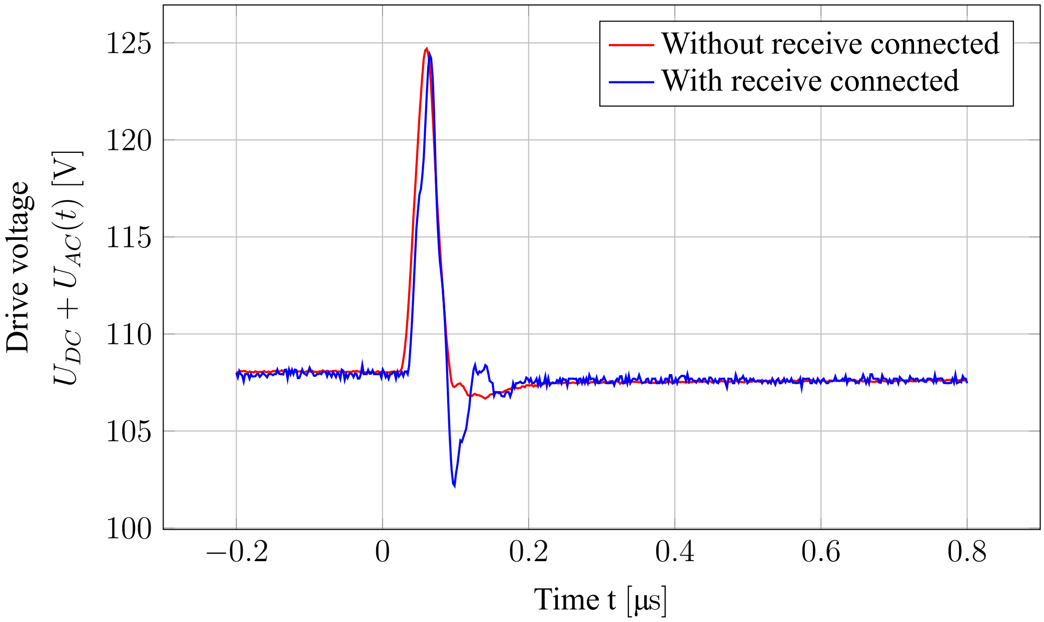

Figure 4.20: Drive signal with and without connected receive path

The reflector does not have a significant influence on the hydrophone, as the hole drilled into the reflector is small in comparison to the diameter of the main lobe of the sound cone. To verify this statement, the hydrophone signals with and without reflector are compared.

Therefore, a correction is necessary, because the distances for both measurements were slightly different. The maximum sound pressures at the times $t_{max,1}$ and $t_{max,2}$ are ascertained and the propagation loss in the far field is approximated with $p \sim 1/r$. From these parameters, a correction factor can be calculated and applied to the hydrophone signal U_{Hyd}:

$$\Delta t = (t_{max,2} - t_{max,1}), \tag{4.26}$$

$$U_{H,corr}(t) = U_{Hyd}(t - \Delta t) \cdot \frac{t_{max,1}}{t_{max,2}}. \tag{4.27}$$

The hydrophone signals measured in the two experiments are very similar (figure 4.21). This confirms, that the measured hydrophone signal represents the sound pressure emitted by the CMUT into free space.

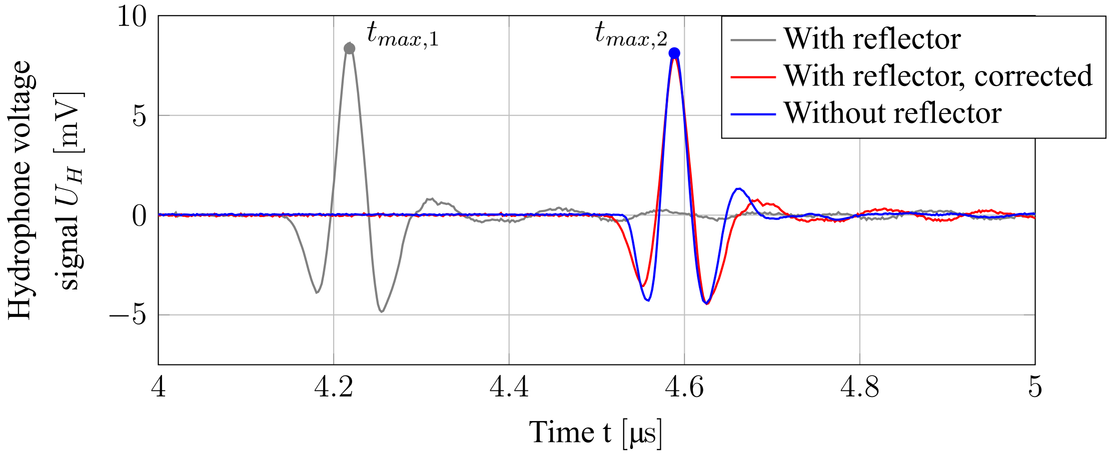

Figure 4.21: Comparison of the signals measured by a hydrophone with and without reflector

4.5.3 Extraction of the Receive Sensitivity

The sound pressure signal emitted by one CMUT array element is measured by the hydrophone and reflected to the receive CMUT. In order to calculate the receive sensitivity H_R, the transfer function T_{ges} between the hydrophone signal and the sound pressure on the surface of the receive CMUT has to be known. The transfer function T_{ges} comprises the geometric propagation loss T_g, the acoustic material damping T_m and the absorption at the reflector T_{ref}. All three parts reduce the sound pressure amplitude of the acoustic wave before it reaches the receive CMUT

$$T_{ges} = \frac{p_{CMUT}}{p_{hyd}} \leq T_{ref} \cdot T_g \cdot T_m. \tag{4.28}$$

An analytic estimation allows to calculate the lowermost signal loss from the hydrophone to the receive CMUT and is explained in the following.

The acoustic reflection coefficient T_{ref} depends on the acoustic impedance of the reflector. In the setup plexiglass is used with an impedance Z_{Plex}, which is about two times higher than the impedance of water[6] [GG06, p. 383]. From these information, the reflection coefficient T_{ref} can be calculated:

$$T_{ref} = \frac{Z_{Plex} - Z_{H_2O}}{Z_{Plex} + Z_{H_2O}} \approx 0.36. \tag{4.29}$$

The resulting amplitude relation between incident and reflected wave is $T_{ref} = 0.36$.

---

[6] $Z_{H_2O} = 1.5 \cdot 10^6 \; 1\,\mathrm{kg/(s\,m^2)}$; $Z_{Plex} = 3.2 \cdot 10^6 \; 1\,\mathrm{kg/(s\,m^2)}$

The ultrasonic signal propagates the distance r from the send CMUT to the hydrophone and the same distance back to the receive CMUT. As the hydrophone is located in the far field of the array element, the geometric transmission coefficient becomes

$$T_g = \frac{d_{ref}}{2d_{ref}} = 0.5\,. \tag{4.30}$$

This coefficient does not depend on the absolute distance between CMUT and reflector d_{ref} and is valid as long as the hydrophone is in the far field of the transducer.

The material damping of the water is $0.002\,\mathrm{dB/(MHz\,cm)}$[Azh10]. For the short distance d_{ref} of $6\,\mathrm{mm}$ the material damping corresponds to a frequency-dependent transmission coefficient $T_m(f)\ \geq 0.99$ from the reflector to the CMUT for the whole frequency range below $100\,\mathrm{MHz}$.

The signal loss due to the hole in the reflector is not considered here. Based on this analysis, the transfer function from the hydrophone to the reflector is:

$$T_{ges} = \frac{p_{CMUT}}{p_{hyd}} \leq T_{ref} \cdot T_g \cdot T_m \approx 0.18\,. \tag{4.31}$$

The receive sensitivity of the CMUT $\underline{H}_R$ can be calculated from the hydrophone signal U_{Hyd}, the CMUT receive signal $U_{R,CMUT}$ and the transfer function T_{ges}:

$$\underline{H}_R(f) \geq \frac{\underline{U}_{R,CMUT}(f)}{\underline{p}_{Hyd}(f) \cdot T_{ges}} = \frac{\mathcal{F}\{U_{R,CMUT}(t)\}}{\mathcal{F}\{U_{Hyd}(t)\} \cdot H_{hyd}(f) \cdot T_{ges}}. \tag{4.32}$$

The bandwidth of the sensitivity basically depends on the impedance match between the CMUT plate and the surrounding medium. Especially for practical use, it makes sense to find also a single-number indication for the receive sensitivity. Therefore, the peak-to-peak receive voltage $\hat{U}_{R,CMUT}$ and the hydrophone signal $\hat{U}_{Hyd}$ is used:

$$H_{R,P2P} \geq \frac{\hat{U}_{R,CMUT}}{\hat{U}_{Hyd} \cdot H_{hyd} \cdot T_{ges}}. \tag{4.33}$$

The accuracy of the measurement results can be increased significantly by calibrating the system using a reference transducer with known send- and receive sensitivity. This is recommended, when the exact absolute receive sensitivity must be measured. For the comparison of the receive sensitivity of different CMUT designs, the uncalibrated setup is mostly sufficient.

4.5.4 Measurement Procedure

Two different types of measurements have to be performed:

- receive sensitivity as function of the incident sound pressure level and
- receive sensitivity as function of to the DC bias voltage.

At first, the incident sound pressure p_{CMUT} is altered and the receive signal of the CMUT is analyzed. Therefore, the amplitude of the ultrasonic signal p_{CMUT} emitted by the send CMUT can be varied by changing the DC bias voltage $U_{S,DC}$. In the next step, the send sound pressure p_{CMUT} (bias voltage of the send CMUT $U_{S,DC}$) is kept constant, while the bias voltage $U_{R,DC}$ of the receive CMUT is changed. With this procedure, both types of measurement listed above are addressed. In figure 4.22, measurement 0 to 448 represent one cycle of the measurement sequence.

One major issue of the CMUT technology is charging. This means, that charge carriers remain in the insulating layers within the CMUT, even if no electrical voltage is applied. This effect changes the characteristics of the CMUT element depending on the previous applied bias voltage. A second run of the full sequence with inverse AC drive voltage $U_{S,AC}$ allows to identify and monitor this charging effect (measurements #449...896 in figure 4.22). If charging appears, the results with inverse voltage differ from the previously measured signals.

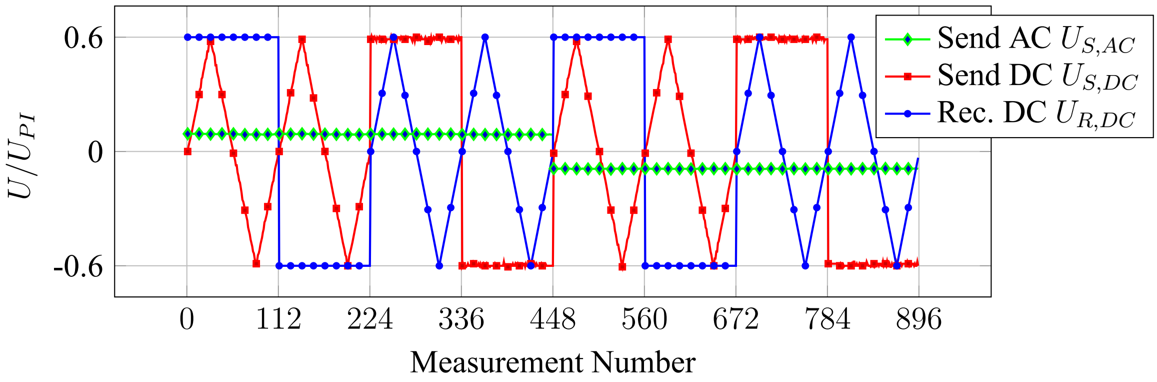

Figure 4.22: Measurement sequence used: DC bias voltages $U_{S,DC}$, $U_{R,DC}$ and AC peak-to-peak drive voltage $U_{S,AC}$ vs. measurement number. All values are normalized on the pull-in voltage U_{PI}

At each measurement (figure 4.22), both the hydrophone signal U_{Hdy} and the CMUT U_{CMUT} receive signal are acquired. In post processing, the peak-to-peak values of both signals are extracted. From this information, the success of the measurement can be validated including the fact that no charging effects appeared. Figure 4.23 represents a valid measurement without the influence of charging. The hydrophone signal increases and decreases corresponding to the send DC bias and the signal is higher, when AC drive and DC bias voltage have the same polarization. The CMUT receive voltage follows the hydrophone signal, when the DC bias of the receive CMUT is not changed. A variation of the receive CMUT's bias voltage $U_{R,DC}$ involves a change of the CMUT receive signal as well.

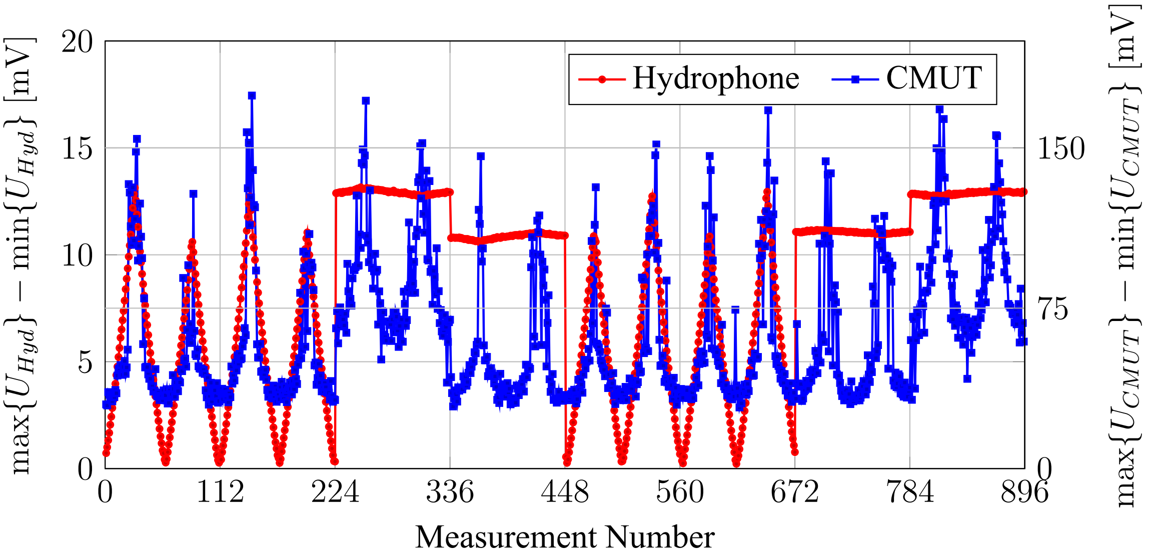

Figure 4.23: Measurement number (see figure 4.22) and corresponding peak-to-peak voltage measured by the hydrophone and the receive CMUT

The peak-to-peak values of the signals cannot be used to calculate the receive sensitivity without further signal processing, as especially the CMUT receive channel is significantly affected by noise. This is also the reason, why a CMUT receive voltage is measured, even if the hydrophone does not show a reasonable sound pressure amplitude. The resulting noise amplitude changes depending on the channel input range of the oscilloscope, which is set automatically by the measurement algorithm. This means, that only subtracting a constant noise amplitude from the peak-to-peak signal is not meaningful. In addition, the information about the phase is lost and no distinction between a positive or negative transient sound pressure signal is possible.

4.5.5 Signal Conditioning

Mainly the CMUT receive signal is affected by noise. Particularly, at low incident sound pressure amplitudes and low bias voltages $U_{DC,R}$ on the receive CMUT, the signal-to-noise ratio becomes lower than 6 dB. For accurate measurement results, the impact of the noise on the acquired CMUT receive signal must be reduced. The maximum bandwidth of the receive channel was limited to 200 MHz by a high-cut filter in the oscilloscope. However, a Fourier transform of the receive signal points out massive distortions in the frequency range above 60 MHz. Thus, a digital finite impulse response (FIR) bandpass filter is used to reduce parasitic effects and noise as shown in figure 4.24.

a) Time domain signal

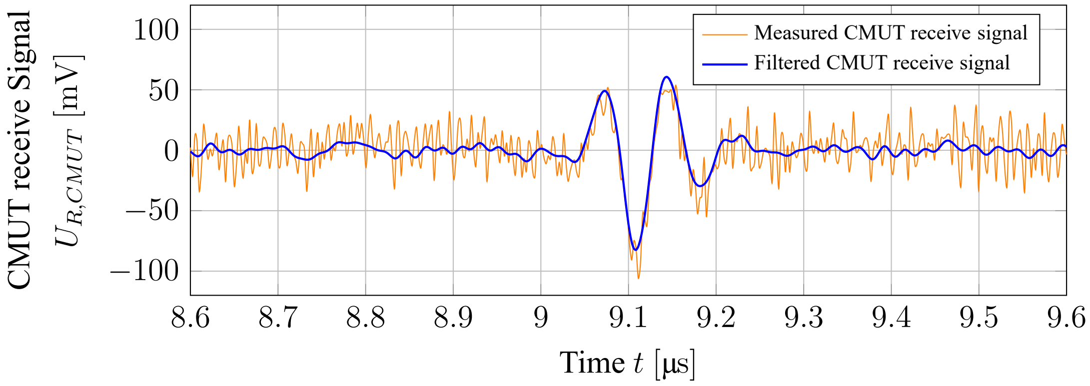

b) Frequency domain signal

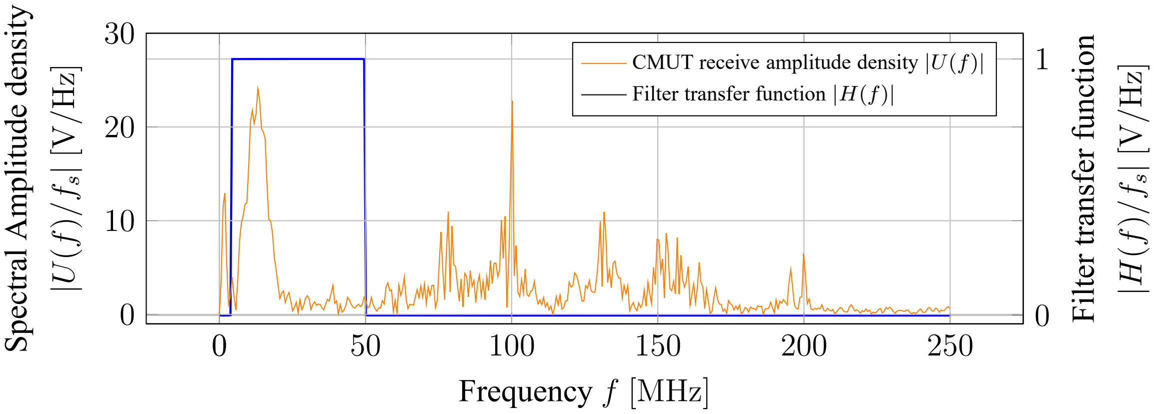

Figure 4.24: Receive signal measured by the CMUT in a) time domain and b) frequency domain. The signal was filtered using a finite-impulse response (FIR) high-cut filter

The filtered signal still contains noise. The aim is to remove the influence of the noise from the measured peak-to-peak amplitude of the ultrasonic signal. At the time before and after the sound wave impacts the CMUT, only the noise is present on the receive channel and can be investigated further. A statistical analysis shows, that the acquired sample values follow a normal distribution (see figure 4.25), when only the noise is present. According to [GG06], the peak-to-peak value n_{P2P} of a stationary normal distributed signal is approximately six times the signals standard deviation σ_n:

$$n_{P2P} = 6 \cdot \sigma_n = 6 \cdot \mathrm{RMS}\{U(t)\}. \tag{4.34}$$

For a stationary time signal, the standard distribution equals the root mean square of the signal.

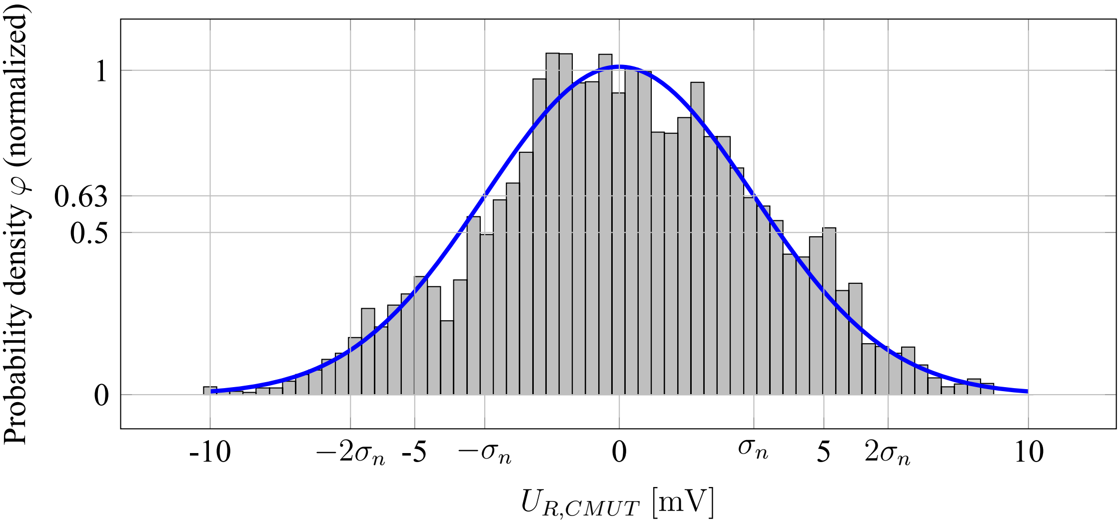

Figure 4.25: Probability distribution for the noise value of the CMUT receive channel (gray bars) and corresponding normal distribution with mean $\mu = 0$ and standard deviation $\sigma_n = \mathrm{RMS}\{U_{R,CMUT}(t)\}$.

Accordingly, any peak-to-peak U_{P2P} value extracted from the noisy CMUT receive channel is corrected by the corresponding noise level n_{P2P}. In addition, a sign is applied to the peak-to-peak value. If the maximum value of the signal is greater than the absolute value of the signal's minimum, the peak-to-peak value is treated as positive, otherwise negative:

$$\hat{U} = U_{P2P} = \begin{cases} +(\max\{U(t)\} - \min\{U(t)\}) - n_{P2P}, & \text{if } \max\{U(t)\} > |\min\{U(t)\}| \\ -(\max\{U(t)\} - \min\{U(t)\}) + n_{P2P}, & \text{if } \max\{U(t)\} \leq |\min\{U(t)\}| \end{cases} . \tag{4.35}$$

This allows to keep the information about the polarization of the incident ultrasonic signal.

The application of this noise-canceling to the hydrophone signal U_{Hyd} and the CMUT signal U_{CMUT} significantly improves the quality of the result. From the achieved peak-to-peak signal values, it is possible to calculate the receive sensitivity even at small bias voltages and sound pressure amplitudes (figure 4.26).

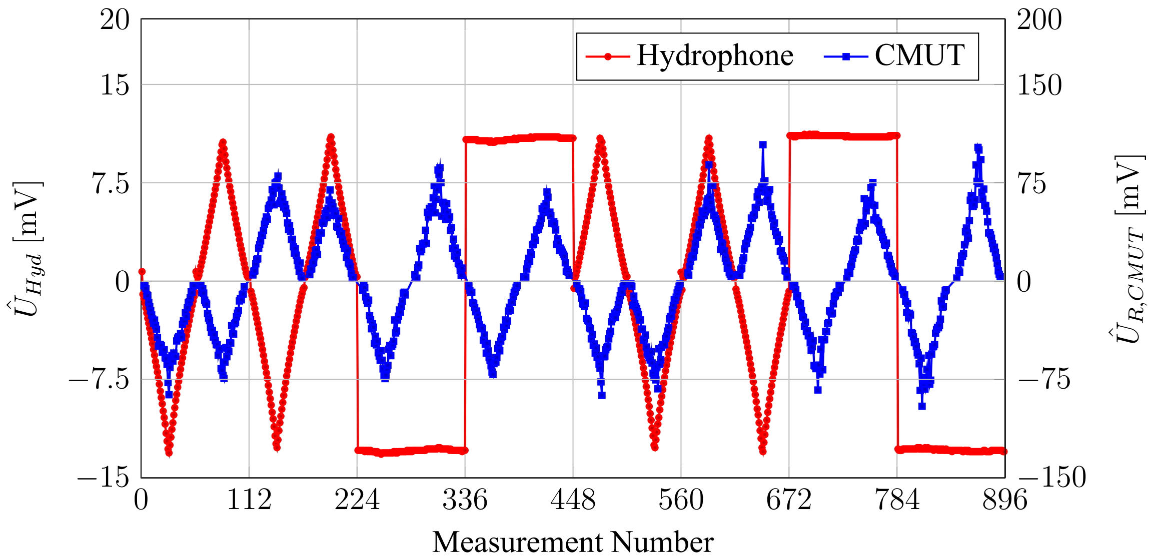

Figure 4.26: Corrected peak-to-peak voltage $\hat{U}_{Hyd}$ and $\hat{U}_{R,CMUT}$ measured by the hydrophone and the receive CMUT respectively (see figure 4.22) for corresponding applied voltages).

4.5.6 Measurement Results

In this section, the results of the receive sensitivity measurement are presented. For each measurement (see figure 4.26) a receive sensitivity $H_{R,P2P}$ can be calculated according to equation (4.33). However, a further analysis of the results is necessary, as the CMUT is a nonlinear device and the absolute incident sound pressure amplitude and the DC bias voltage have an impact on the send sensitivity. In the first step, the linearity of the CMUT cell is analyzed depending on the incident sound pressure amplitude. In addition, the influence of the DC bias voltage on the receive sensitivity of a CMUT is investigated. The last part of this section shows the spectral bandwidth of the CMUT in receive operation.

a) Receive Sensitivity vs. Incident Sound Pressure

At first, the relation between CMUT receive signal and incident sound pressure shall be investigated at constant bias voltage. Therefore, the measurement results are used, where the DC bias voltage of the receive CMUT $U_{R,DC}$ is 60 % of the pull-in voltage ($U_{R,DC} = \pm 0.6\, U_{PI}$). The DC bias of the send CMUT $U_{S,DC}$ is altered to change the amplitude of the sound pressure signal.

The hydrophone signal U_{Hyd} scales linear with the incident sound pressure p_{Hyd} and the transfer function T_{ges} between hydrophone and CMUT is a pressure independent constant (see equation (4.31)). Thus, any nonlinear relation between hydrophone signal and CMUT receive signal is generated due to the nonlinear (pressure amplitude-dependent) receive sensitivity of the CMUT.

Figure 4.27 shows the peak-to-peak signal of the CMUT receive voltage over the sound pressure measured at the hydrophone. For small pressure amplitudes, the dynamic deflection of the CMUT is directly proportional to the sound pressure. This indicates a linear characteristic of the CMUT. This is confirmed by a linear regression U_{reg} as shown in figure 4.27 with a coefficient of determination $R^2 = 0.94$:

$$U_{reg} = m_{reg} \cdot \hat{U}_{Hyd}. \tag{4.36}$$

For the regression, only measurements with a signal to noise ratio $\mathrm{SNR} > 6\,\mathrm{dB}$ respectively $\hat{U}_{R,CMUT} > 2 \cdot n_{eff}$ have been used.

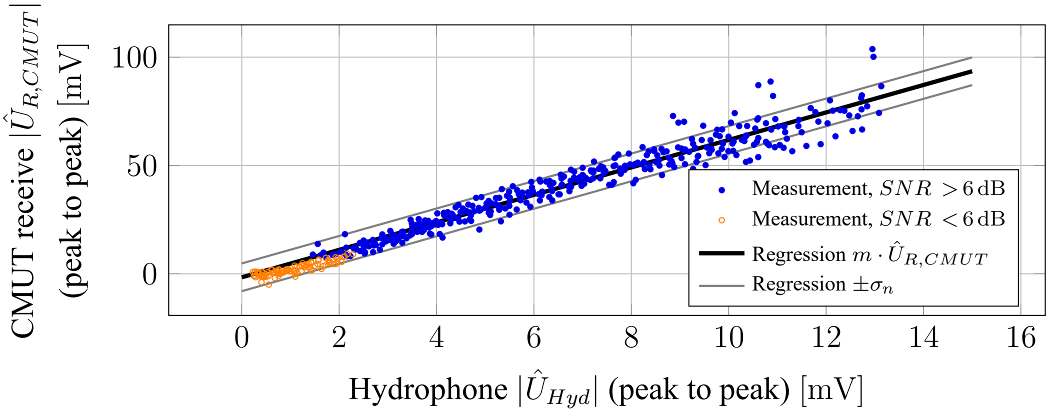

Figure 4.27: Receive signal (peak-to-peak) measured by the hydrophone vs. the receive signal of the CMUT. The DC bias voltage applied to the receiving CMUT was $0.6\,U_{PI}$ for all measurements.

From the slope m_{reg} of the regression, the receive sensitivity $H_{r,P2P}$ can be calculated:

$$H_{r,P2P} = m_{reg} \cdot \frac{1}{H_{hyd}(f) \cdot (T_{ref} \cdot T_g \cdot T_m(f))}. \tag{4.37}$$

The hydrophone used for the measurements has a sensitivity of $1530\,\mathrm{nV/(Pa\,mm^2)}$. Using equation (4.37), the sensitivity of the CMUT element becomes $940\,\mathrm{nV/(Pa\,mm^2)}$ at $U_{R,DC} = 0.6\,U_{PI}$ (without receive amplifier). This shows, that the receive sensitivity of this CMUT design is comparable to a needle hydrophone as used in this experiment, if the bias voltage is increased further.

b) Receive Sensitivity vs. DC Bias Voltage

In the next step, the receive sensitivity $H_{r,P2P}$ of the CMUT depending on the DC bias voltage $U_{R,DC}$ is investigated. Physically, the increase of the receive bias has two effects: The displacement current $i_{\Delta C}$ created from the capacity change is increased, because more charge carriers are stored on the electrodes due to the higher bias (see also equation (2.8))

$$i_{\Delta C}(t) = U_{R,DC}\frac{\mathrm{d}C_{CMUT}(t)}{\mathrm{d}t}. \tag{4.38}$$

In addition, the average deflection w_{avg} of the CMUT plate increases due to the electrostatic force created by the DC bias voltage. Assuming the most general case, that an attractive force between the two electrodes exists, the derivative of the capacity is a function $g(\cdot)$ of the incident sound pressure signal and the absolute value of the DC bias voltage

$$\frac{\mathrm{d}C_{CMUT}(t)}{\mathrm{d}t} = \varepsilon A\frac{\mathrm{d}}{\mathrm{d}t}\left(\frac{1}{d_g - w_{avg}(t)}\right) = -g(|U_{R,DC}|)\cdot p_{CMUT}(t). \tag{4.39}$$

A negative sign is added to the function $g(\cdot)$, as a positive bias voltage deflects the CMUT plate towards the bottom electrode, increases the capacity and creates a negative current flow (into) the CMUT. According to this convention, the CMUT is an inverting receiver, (when biased with positive bias voltage). Additionally, a linear relation between incoming sound pressure p_{CMUT} and the displacement current $i_{\Delta C}$ is assumed. The validness of this fact has been shown in the previous paragraph (see also figure 4.27). The (nonlinear) relation between the bias voltage $U_{R,DC}$ and the dynamic capacity change can be approximated using a Maclaurin series (Taylor series around the point zero):

$$\begin{aligned} i_{\Delta C}(t) &= -U_{R,DC}\cdot K_R\cdot p_{CMUT}(t)\left(\sum_{n=0}^{\infty} a_n\cdot |U_{R,DC}|^n\right) && (4.40)\\ &= -K_R\cdot p_{CMUT}(t)\sum_{n=0}^{\infty} a_n\cdot U_{R,DC}^{(n+1)}. && (4.41)\end{aligned}$$

The value K_R is a scalar proportionality constant, which allows to transfer the fraction between measured current $i_{\Delta C}$ and incoming sound pressure amplitude into the receive sensitivity $H_{r,P2P}$:

$$\begin{aligned} K_R &= \frac{i_{\Delta C}(t)}{p_{CMUT}(t)\cdot H_{r,P2P}}, && (4.42)\\ H_{r,P2P} &= -U_{R,DC}\left(\sum_{n=0}^{\infty} a_n\cdot |U_{R,DC}|^n\right). && (4.43)\end{aligned}$$

This is possible, as both the receive amplifier and the acoustic transfer function from the hydrophone to the CMUT and the hydrophone itself are assumed as linear.

Equation (4.43) allows to calculate the receive sensitivity of a CMUT, if the parameters a_n are known. This is possible by fitting the equation to measurement results. Therefore, the receive sensitivity is calculated from the measured signals by using equation (4.33). Actually, all measurements can be used for this analysis, as the CMUT's receive signal is approximately direct proportional to the incident pressure as shown in figure 4.27. Only for very small send signals in combination with a small bias voltage $U_{R,DC}$, the calculated receive sensitivity is inaccurate. The reason is the signal to noise ratio in the receive path, which is below 6 dB in this case.

Figure 4.28 shows the measurement results and a fit of equation (4.43). The achieved fit curve for $n \leq 3$ is sufficient and results in a coefficient of determination $R^2 = 0.94$.

$$H_{r,P2P} = a_2 \cdot U_{R,DC}^3 + a_1 \cdot U_{R,DC}^2 + a_0 \cdot U_{R,DC} \tag{4.44}$$

Thereby, only data points with a signal to noise ratio $\mathrm{SNR} > 6\,\mathrm{dB}$ are used for the fit.

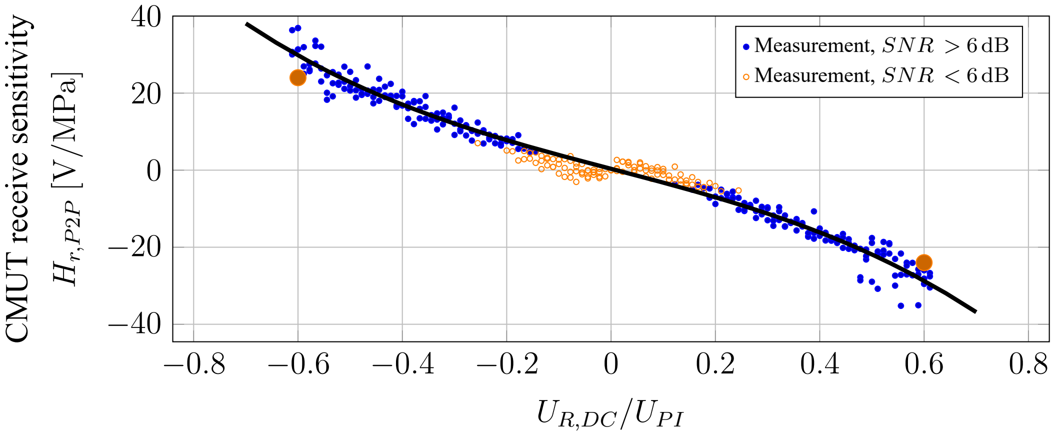

Figure 4.28: Receive sensitivity over the DC bias voltage of the receiving CMUT and fit of equation (4.43).

The measured receive sensitivity of the CMUT design[7] yields:

$$\frac{H_{r,P2P}}{1\,\mathrm{V}/\mathrm{MPa}} \approx -36.51 \cdot \left(\frac{U_{DC,R}}{1\mathrm{V}}\right)^3 + 0.53 \cdot \left(\frac{U_{DC,R}}{1\mathrm{V}}\right)^2 - 35.63 \cdot \frac{U_{DC,R}}{1\mathrm{V}}\,. \tag{4.45}$$

---

[7] see design 1 in table B.4

c) Spectral Bandwidth

In addition to the single value $H_{r,P2P}$ for the receive sensitivity , also a spectral analysis has been performed. Therefore, the spectral bandwidth of the receive signal $U_{R,CMUT}$ was investigated for different DC bias voltages $U_{R,DC}$. Again, the noise of the CMUT receive channel becomes an issue when calculating the receive sensitivity in frequency domain. Figure 4.29 shows the spectral amplitude of a CMUT receive signal and the corresponding noise. At frequencies lower than $10\,\mathrm{MHz}$, the noise dominates the spectral amplitude. The signal shown in figure 4.29 represents the highest CMUT receive signal amplitude acquired within the full measurement cycle. For all other measurements the noise becomes even more dominant.

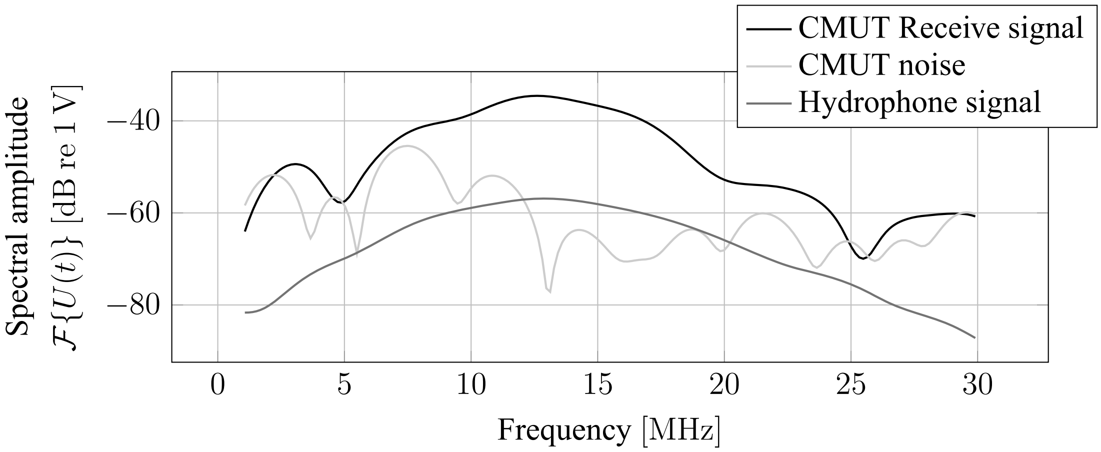
CMUT Receive signal
CMUT noise
Hydrophone signal
Spectral amplitude
$\mathcal{F}\{U(t)\}$ [dB re 1 V]
−40
−60
−80
0
5
10
15
20
25
30
Frequency [MHz]

The CMUT receive sensitivity was calculated using the cross-spectral density to reduce the impact of the noise on the transfer function:

$$\underline{H}_R(f) = \frac{S_{XY}(f)}{S_{XX}(f)} = \frac{\mathcal{F}\{U_{R,CMUT}(t)\} \cdot \mathcal{F}\{U^*_{Hyd}(t)\}}{\mathcal{F}\{U_{Hyd}(t)\} \cdot \mathcal{F}\{U^*_{Hyd}(t)\} \cdot H_{hyd}(f)}. \tag{4.46}$$

The resulting spectral curve of the receive sensitivity does not indicate a significant relation to the applied DC bias voltage $U_{R,DC}$ (figure 4.30). Only the absolute value of the receive sensitivity increases with rising bias voltage $U_{R,DC}$ applied. This effect has already been discussed in the previous paragraph b) (see also figure 4.28).

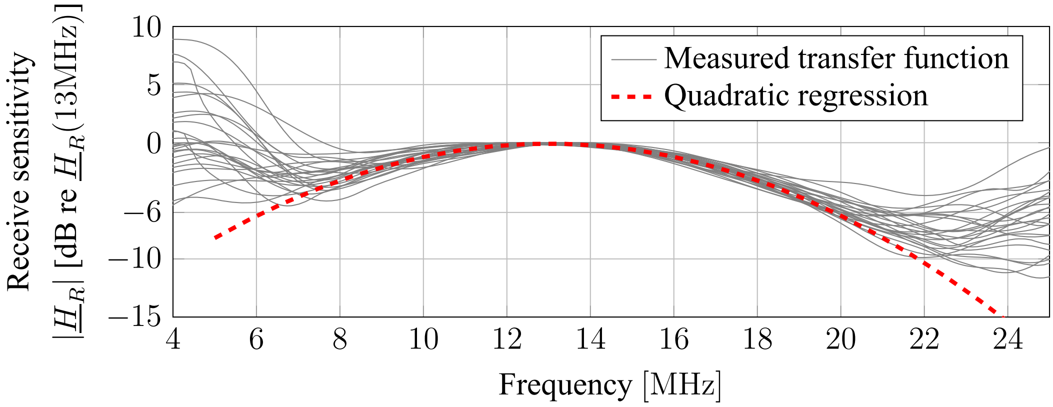
Receive sensitivity
$|\underline{H}_R|$ [dB re $\underline{H}_R(13\mathrm{MHz})$]
10
5
0
−6
−10
−15
4
6
8
10
12
14
16
18
20
22
24
Frequency [MHz]
Measured transfer function
Quadratic regression

A quadratic regression in the range between 8 and $20\,\mathrm{MHz}$ offers to estimate the receive bandwidth. A $-6\,\mathrm{dB}$ fractional bandwidth of $110\,\%$ and a center frequency of $13\,\mathrm{MHz}$ are achieved. Small variations of the bandwidth (depending on the DC bias voltage) as shown in the send sensitivity measurements (figure 4.16) cannot be proven, because the noise predominates the receive signal.

4.5.7 Conclusions

In section 4.5 a method for the experimental determination of the receive sensitivity of a CMUT has been presented in this section. The procedure is based on a pitch-catch measurement via a reflector. An embedded hydrophone is used to measure the incident sound pressure. This allows to use the same CMUT design as ultrasonic reference sound source. This ability supersedes the selection of another source, which must be able to transmit in the full frequency bandwidth necessary.

The receive sensitivity of a CMUT design is measured depending on the incident sound pressure amplitude and applied DC bias voltage. The bandwidth of the receive sensitivity was determined in frequency domain. For all measurements, the noise level of the receive path became an issue. Thus, signal post-processing and filtering was necessary for achieving accurate results. However, improving the receive electronics can further increase the quality of the results.

The full measurement takes between $20\,\mathrm{min}$ and $2\,\mathrm{h}$ depending on the desired accuracy. Especially for long measurement durations, charging effects may become present in some CMUT chips. In this case, the receive sensitivity cannot be identified, but the setup allows the acoustic investigation of charging.

4.6 Uniformity of a CMUT Array

Caused by manufacturing deviations, small variations of the CMUT characteristics appear over a wafer. Then, the characteristics of the individual CMUT elements show small differences in their eigenfrequency, send- or receive sensitivity. In this section, a measurement procedure based on the sound field scanning setup is described, which allows to investigate the (acoustic) equality of CMUT array elements within an 1D-array.

4.6.1 Basic Approach

The sound field of an ultrasonic transducer based on CMUTs results from the superposition of the emitted acoustic waves of each individual CMUT cell. Thus, the comparison of the sound field of the individual array elements within a CMUT array is a reliable indicator for the equality of the CMUTs all over the array. Additionally, the symmetry of the sound field of one array element permits an interpretation of the equality of the CMUT cells within the element.

However, the long measurement duration is a drawback of a full sound field scan. A sound field scan as shown in figure 4.11 for one array element with adapted spatial resolution takes $10...20\,\mathrm{min}$ depending on the achieved signal to noise ratio. Then the complete evaluation of a full array with 128 elements takes about 1...2 days. Additionally, it has to be ensured that the drive signal does not change, when another channel (with another parasitic capacity) is connected.

To overcome both problems, but still be able to reliably investigate the equality of a full array, the sound field scanning is reduced to a 1D-line scan. The measurement of several array elements is done by connecting them in parallel and driving them simultaneously. The sound field created by the individual array elements needs to be separated in the scanning result. Therefore, the array elements are driven in pairs of two with a gap to the next doublet as shown in figure 4.31. The reason for driving the array elements as doublets is the resulting directivity of the sound field. The sound field of an array element pair becomes directive in comparison to the omnidirectional radiation of a single array element. The interspace has to be large enough in order to separate the created sound fields of each element pair from their neighbors. For an interspace of two array elements as used in figure 4.31, each individual array element is accessed after two scans. With this procedure, it is possible to investigate a full 1D-array within $1\,\mathrm{h}$.

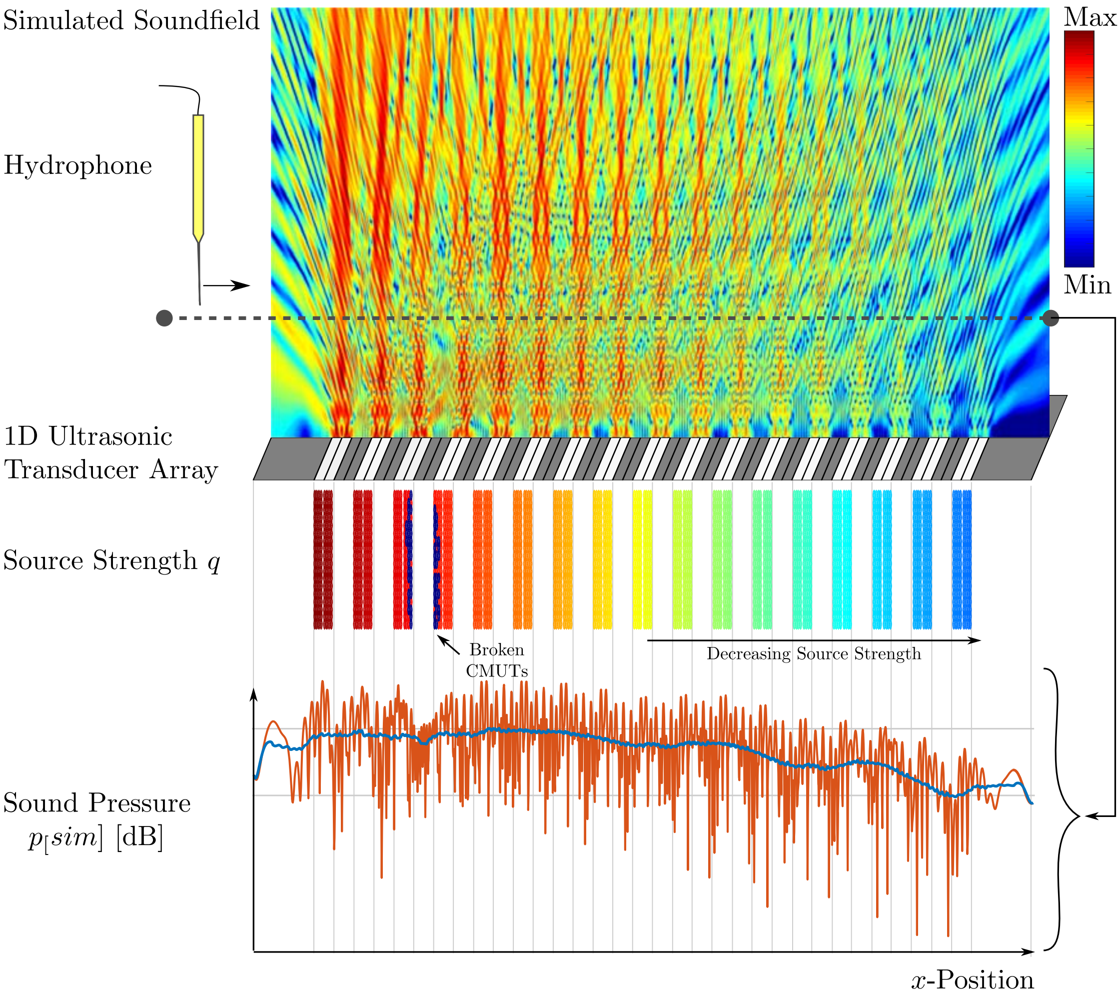

Figure 4.31: Sound field (simulated) of a 1D CMUT array with array elements emitting in pairs. Each array element (256 µm × 1 mm) consist of 72 individual sources radiating at 12 MHz

The result of the line scan enables to compare the equality of two neighboring CMUT array elements in detail as well as the diversity over a full transducer. Every proper working doublet generates a symmetric sound field. The measurement may show an asymmetric sound field for two reasons.

- Either the sound field is affected by asymmetric side lobes of neighboring doublets at the edge of the array, or
- some CMUT cells within the array elements of the transmitting doublet have a different characteristic.

An example is given in figure 4.31, where some CMUTs of the 10th and 14th array element are treated as broken. In the red curve indicating the sound pressure measured at a line scan, both corresponding pairs show an asymmetrical sound pressure level and the sound pressure in between the doublets drops.

Individual CMUT elements with a different characteristic can be investigated by analyzing the symmetry. However, a small decrease or increase of the source strength is not clearly visible in the line scan. A spatial low pass filtering of the sound pressure curve measured in a line scan allows to extract such (small) trends. The cut-off length of the filter should equal the distance between two doublets, which ensures to always include the same amount of transmitting CMUTs for each sampling point. The filtered (blue) sound pressure curve in figure 4.31 clearly indicates a decreasing sound pressure level with increasing x-position. The reason for this is the source strength, which descends in x-direction. For real CMUTs, this effect can appear due to a change in gap or plate thickness which impacts the send sensitivity.

4.6.2 Measurement Results

Prior the measurement, the sound field scanning setup was adjusted as described in section 4.3.

In the CMUT array, 32 out of 128 array elements have been connected to the drive signal. They were arranged by groups of two connected and six unconnected elements as represented by the active array element numbers: $\{5; 6; 13; 14; 21; 22; ...; 117; 118; 125; 126\}$. The gap of six array elements allows to separate the signal for each radiating pair of array elements. A smaller gap then six elements is possible, but the number of CMUT elements connected in parallel was limited to 32 by the power of the RF amplifier (see section 4.2.3).

Using this setup, a line scan in x-direction within the x-z-plane was done resulting in the measured peak-to-peak sound pressure over position x_t (gray line in figure 4.32) . It is important that the step width of the hydrophone in x-direction is smaller than half of the wavelength of the ultrasonic signal and smaller than half of the array element size to meet the Nyquist-theorem in space. The equality of the CMUT array can be seen after low-pass filtering the sound pressure curve in space (black line in figure 4.32).

The results shown in figure 4.32 indicate a very uniform behavior of the CMUTs within the 1D array on one side of the array (position $x_t \geq 0\,\mathrm{mm}$). The maximum variation of the trend curve is less than $1.2\,\mathrm{dB}$ for $x_t \leq 0\,\mathrm{mm}$, which is in the range of the uncertainty of the hydrophone measurement. On the other side of the array ($x_t \geq 0\,\mathrm{mm}$), a clear maximum and a minimum of the sound pressure appear. Here, various effects could play a role. Resonance frequencies of the individual array elements have been measured on wafer level by electrical impedance measurements and do not change significantly over the array. This means that the plate structure of the CMUT is very uniform for each array element. A thickness measurement on the wafer of the SiO_2 insulation layer showed a variation of circa $5\,\%$ within the chip. Due to the fact that only 16 thickness measurement points all over the wafer have been collected, it remains unclear, if this is the only reason for the change in the sound pressure. The measurement of the pull-in voltage of each array element offers more information. However, charging effects, which appear especially when the CMUTs are pulled in, make a reliable conclusion impossible.

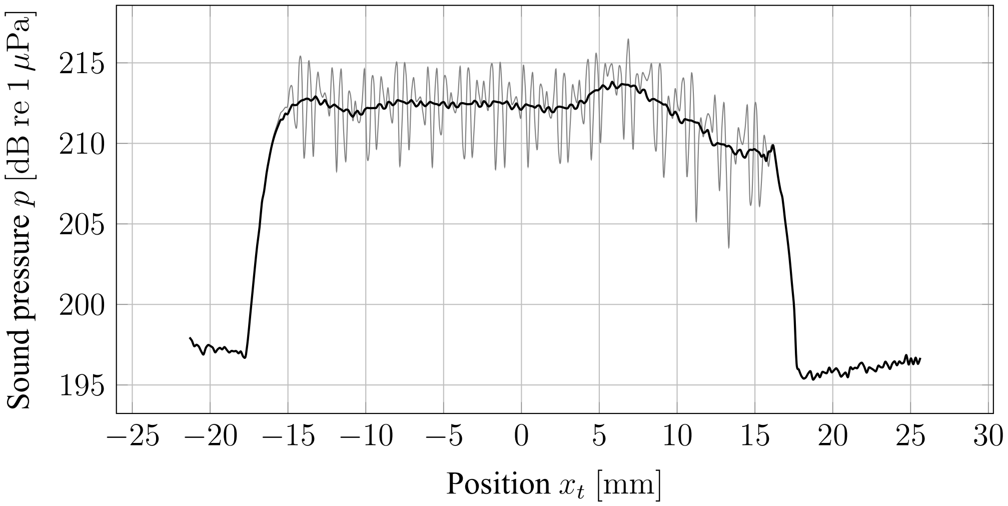

Figure 4.32: Sound pressure at position $y_t = 0$ and $z_t = 5\,\mathrm{mm}$ depending on the azimuthal position (azimuthal line scan). Gray: measured sound pressure (peak-to-peak), black: spatial trend

Nevertheless, the result validates the usability of this chip for beamforming. The sound pressure in figure 4.32 shows a repetitive pattern and the amplitude is in a range within $5\,\mathrm{dB}$. The low-pass filtered curve can be used as amplitude correction factor in send operation to ensure a uniform sound pressure deviation all over the array.

Chapter 5

Electrical CMUT Characterization

THE electrical impedance is a significant parameter for the characterization of a CMUT, as properties having an impact on the dynamic movement of the plate also affect the electrical impedance of the CMUT. Additionally, the electrical impedance is the decisive parameter for the development of drive- and receive electronics.

In this chapter, a novel analytic model for the electrical impedance is described and validated by simulation and measurement results. Additionally, performance parameters are extracted from impedance measurements by using analytic models. A method for a quality assessment based on the electrical impedance is presented, which is developed to be used in a production environment for monitoring the quality of the CMUT.

5.1 Analytical Model

For a better understanding and analysis of the electrical impedance of a CMUT, an analytical model was developed. At first, the Butterworth-van-Dyke model is explained as state of the art approach to describe the electrical impedance of a CMUT cell. Afterwards, the new analytic model is presented. The modeling approach is based on a mass-spring-damper system, which is coupled to a dynamic capacity. For a verification, the model is solved in time and frequency domain and the results will be compared to a FE-model.

5.1.1 Butterworth-van-Dyke Model

The electrical impedance Z of a CMUT defines the ratio between the voltage drop U over a CMUT element and the current i flowing into the CMUT. From the electrical impedance, basic characteristics such as the acoustic bandwidth in air or the mechanical resonance frequency can be obtained. The impedance analysis of CMUTs originates from the electro mechanical description of piezoelectric transducers. The so-called Butterworth-van-Dyke (BvD) equivalent circuit model describes the impedance of a resonant oscillator by an electrical circuitry. It consists of a capacitor C_P (dielectric properties, a capacitor C_S (mechanical dynamic mass), a coil L_S (mechanical stiffness) and a resistor R_S (mechanical damping). In [Par+11] an extended BvD for CMUT is shown, which offers an even better fit to the measured impedance curve of CMUT. Both versions are shown in figure 5.1.

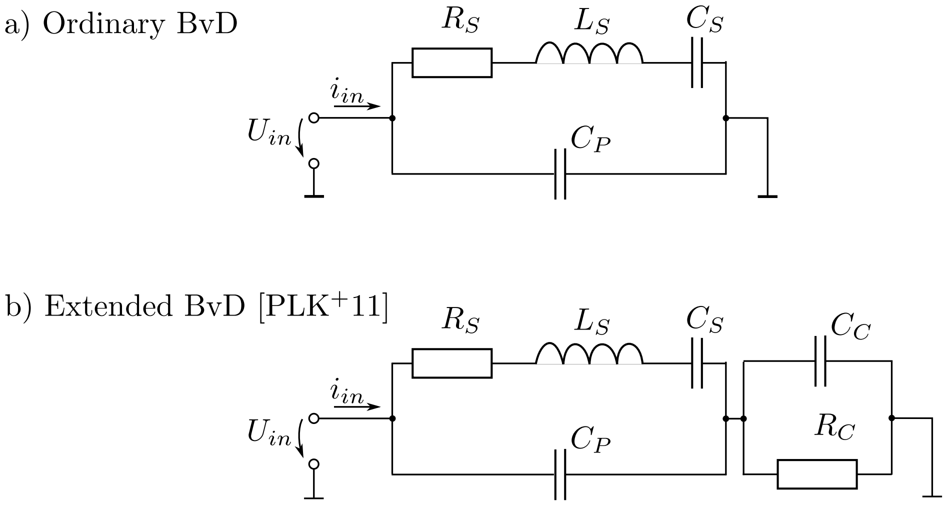

Figure 5.1: Butterworth-van-Dyke equivalent circuit model: Ordinary (a) and extended for CMUT (b)

Characteristic parameters of the BvD are the static capacity C_p and the resonance frequencies $f_{0,1}$ and $f_{0,2}$, where $f_{0,1}$ is the open-circuit (parallel) and $f_{0,2}$ the short circuit (serial) resonance:

$$f_{0,1} = \frac{1}{2\pi} \cdot \sqrt{\frac{L_S \cdot (C_S + C_P)}{C_S C_P}}, \tag{5.1}$$

$$f_{0,2} = \frac{1}{2\pi} \cdot \sqrt{\frac{1}{L_S C_S}}. \tag{5.2}$$

However, the BvD offers a decent model of a resonating CMUT at a specific operating point for a given drive signal and can be easily used in circuit design. It does not cover the impact of the AC and DC drive voltage, the spring-softening effect and the nonlinearity. So, the BvD representation for a CMUT describes the linearized characteristic of a CMUT cell at defined drive conditions.

The aim is now to overcome these limitations by creating a better analytic representation of a CMUT.

5.1.2 Modeling Approach

The bending of a CMUT plate can be described by a superposition of the mechanical eigenmodes of the CMUT. For squared and circular CMUT plates, the 1st and the 5th eigenmode have an impact on the CMUT's capacity, because their average displacement over the CMUT plate is not zero (table 5.1). In air, the CMUT has a very low bandwidth and the eigenfrequencies differ significantly. Thus, no modal coupling between the modes appears and only the first eigenmode of the CMUT is relevant to calculate the first impedance peak.

Table 5.1: Frequency and deflection of different eigenmodes for a squared and circular CMUT geometry with clamped edges, normalized to the first eigenfrequency.

Squared geometry [Lei73]				
Order of eigenmode	1	2; 3	4; 5	6
Eigenfrequency $f_{0,i}/f_{0,1}$	1	2.0	3.0	3.66
Average deflection $\overline{w}/w_{max}$	0.3	0	0	0.15

Circular geometry [Lei69]				
Order of eigenmode	1	2; 3	4; 5	6
Eigenfrequency $f_{0,i}/f_{0,1}$	1	2.1	3.4	3.9
Average deflection $\overline{w}/w_{max}$	0.32	0	0	0.14

The CMUT plate itself is a linear mechanical system because the deflection is small in comparison to the plate dimensions. The deflection w_A of a mechanical system in a linear eigenmode can be completely expressed by a damped spring-mass system with one degree of freedom and the eigenvector of the mode (modal decomposition). The deflection w_A of this simple mass oscillator is directly coupled to the capacity C_A.

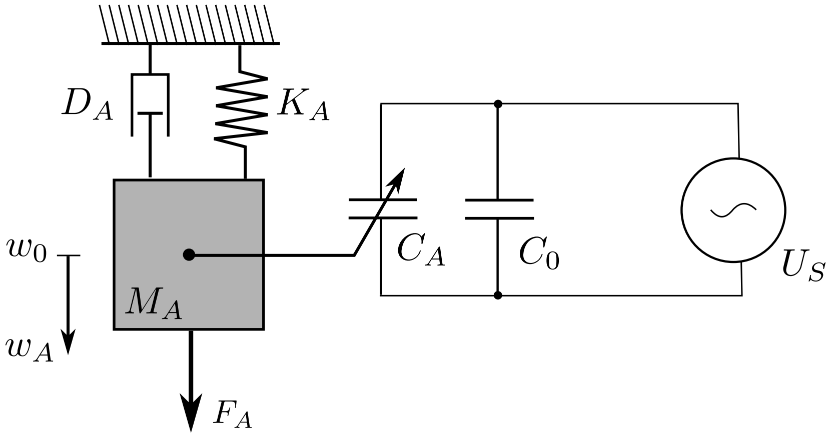

Figure 5.2: Electromechanic model for the dynamic capacity of a CMUT

5.1.3 Time Domain Solution

The time domain solution allows to calculate the complex impedance curve from a given voltage signal $U(t)$, the mechanical (angular resonance frequency ω_0 of the CMUT, the modal damping coefficient D_A and the modal capacity change C_A. To also include the nonlinearity of the CMUT, a factor K_{SH} has to be added.

Starting from the electrical circuit in figure 5.2, the capacity can be expressed by

$$\underline{C}(t) = C_0 + C_A(t). \tag{5.3}$$

To determine the coupling between deflection $w(t)$ and capacity $C_A(t)$, the approximation of a plate capacitor is used. The capacity change due to a deflection $w_A(t)$ of a CMUT with an effective gap d_{eff} is then (for a vacuum gap):

$$\begin{aligned} C_A(w_A, d_{eff}) &= C\left(d_{eff} - w_A(t)\right) - C(d_{eff}) \\ &= \frac{\epsilon_0 \cdot A_{equ}}{d_{eff} - w_A(t)} - \frac{\epsilon_0 \cdot A_{equ}}{d_{eff}} \\ &= \frac{\epsilon_0 \cdot A_{equ}}{d_{eff}^2 - d_{eff} w_A(t)} w_A(t). \end{aligned} \tag{5.4}$$

For small deflections in comparison to the effective gap ($w_A(t) \ll d_{eff}$), the dynamic capacity change C_A is nearly proportional to the deflection w_A:

$$C_A(w_A, d_{eff}) \approx \frac{\epsilon_0 \cdot A_{equ}}{d_{eff}^2} w_A(t). \tag{5.5}$$

For large deflections, equation (5.4) shows the limitations of the linear model. For a compensation, a nonlinear scaling factor could be introduced, wherefore the effective gap of the CMUT must be known. Another possibility to include the nonlinear relation between displacement and capacity is adding a term for the second harmonic generation. This approach is used in this model here.

The relation between the dynamic capacity change $C_A(t)$ and the average deflection of the plate $w(t)$ is now analyzed depending on the applied drive voltage. In the first step, the average displacement $w_A(t)$ is calculated from the electrostatic force $F(t)$. The transfer function $h_{w/F}(t)$ between both parameters describes the mechanical mass-spring-damper system.

$$h_{w/F}(t) = K_0 \cdot e^{-tD_A\omega_0} \cdot \sin(\omega_0 t), \tag{5.6}$$

$$w_A(t) = \int_{-\infty}^{\infty} h_{w/F}(t-\tau) F(\tau) \mathrm{d}\tau. \tag{5.7}$$

Assuming that the capacity is proportional to the displacement $C_A(t) = K_1 \cdot w(t)$ and the electrostatic force is proportional to the square of the drive voltage $F(t) = K_2 \cdot U^2(t)$, equation (5.7) becomes:

$$C_A(t) = K_1 w_A(t) = K_1 \int_{-\infty}^{\infty} h_{w/F}(t-\tau) K_2 U^2(\tau)) \mathrm{d}\tau. \tag{5.8}$$

Summing up all constant scalar factors to a parameter K and expanding the transfer function $h_{w/F}(t)$ leads to

$$C_A(t) = K \int_{-\infty}^{\infty} U^2(t-\tau) \left(e^{-\tau D_A \omega_0} \sin(\omega_0 \tau)\right) \mathrm{d}\tau. \tag{5.9}$$

To determine the factor K, design parameters of the CMUT (such as the effective gap) are necessary. If they are not known, K can be set as the normalized modal amplitude of the dynamic capacity $C_A(\omega)$ at the resonance frequency ω_0

$$K = \underline{C}_A(\omega_0) \frac{\underline{H}_{w/F}(\omega_0)}{\underline{U}^2(\omega_0)}, \tag{5.10}$$

$$C_A(t) = \frac{C_A(\omega_0)}{\underline{U}^2(\omega_0) \cdot 2D\omega_0\sqrt{1-D^2}} \int_{-\infty}^{\infty} U^2(t-\tau) \left(e^{-\tau D_A \omega_0} \sin(\omega_0 \tau)\right) \mathrm{d}\tau. \tag{5.11}$$

Equation (5.11) allows to calculate the dynamic capacity change in time domain. Therefore, the damping coefficient D_A, the resonance frequency ω_0 and the dynamic capacity change in the resonance frequency have to be known. If also the CMUTs nonlinear characteristic shall be added to the model, equation (5.4) needs to be analyzed in more detail. It is not possible to implement this equation directly into the transfer function, because then the convolution cannot be solved analytically. A possibility to overcome this problem is using a Taylor approximation:

$$T\left\{\frac{1}{d_{eff}}-\frac{1}{d_{eff}-w_A(t)}\right\}=\sum_{n=1}^{n=\infty}\frac{w_A^n(t)}{d_{eff}^{n+1}} \tag{5.12}$$

Implementing equation (5.12) up to the second coefficient into equation (5.11) allows to also include the nonlinearity between displacement and capacity change.

$$\begin{aligned}C_{A,NL}(t)=&\frac{C_A(\omega_0)}{\underline{U}^2(\omega_0)\cdot 2D\omega_0\sqrt{1-D^2}}\\&\cdot\int_{-\infty}^{\infty}U^2(t-\tau)\left[\left(e^{-\tau D_A\omega_0}\sin(\omega_0\tau)\right)+\frac{K_{SH}}{2}\left(e^{-\tau D_A\omega_0}\sin(\omega_0\tau)\right)^2\right]\mathrm{d}\tau\end{aligned} \tag{5.13}$$

Using trigonometric identities and removing constant offsets, as they are time-independent and therefore part of C_0, shows the effect of the nonlinearity: a second harmonic is generated.

K_{SH} indicates, which fraction of the drive signal is transferred into the second harmonic, because the capacity change is not linearly dependent from the plate deflection. Thus, K_{SH} also depends on the applied drive voltage.

From the capacity change, now the current flow into the CMUT can be calculated for a known drive voltage $U_S(t)$:

$$i_{IA}(t)=U_S(t)\frac{\mathrm{d}C(t)}{\mathrm{d}t}+C(t)\frac{\mathrm{d}U_S(t)}{\mathrm{d}t}. \tag{5.14}$$

The current flow i_{IA} is calculated by inserting either equation (5.11) (linear representation) or equation (5.13) (nonlinear representation) into equation (5.14).Then the fraction of the spectral drive voltage and spectral current flow deliver the impedance in frequency domain:

$$\underline{Z}(\omega)=\frac{\mathcal{F}\{U_S(t)\}}{\mathcal{F}\{i_{IA}(t)\}}. \tag{5.15}$$

With this approach, the impedance can be calculated for any drive signal shape. Also, the implementation in a SPICE simulator is possible, which allows to use the model for the design of electrical drive and receive circuitry for CMUT. In addition, it has potential to be a full representation of a CMUT in immersion as the model allows the extraction of the mechanical impedance of the CMUT plate. However, this is only possible by either provide the dimensions of the CMUT or measure the impedance at several AC and DC voltages. In this case, it has to be ensured, that no charging effects appear.

5.1.4 Validation Based on the Hybrid Simulation Model

For the validation of the analytical impedance model solved in time domain, the electrical impedance of a CMUT cell was simulated using the developed hybrid CMUT model (see section 3.3).

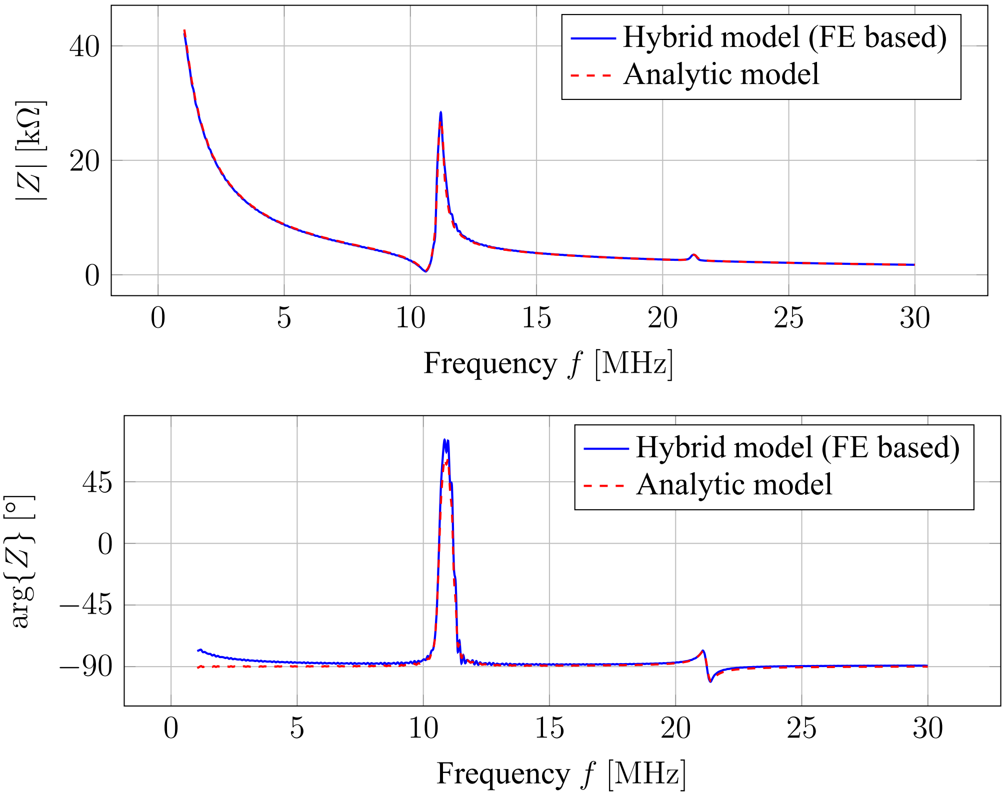

Best fit parameters:

$C_m = 3.1\,\text{pF}$ $C_A = 327\,\text{fF}$ $f_0 = 10.6\,\text{MHz}$ $D_A = 0.006$ $K_{SH} = 0.078$

Figure 5.3: Impedance of a CMUT, simulated using the hybrid CMUT simulation model (section 3.3)and fitted impedance curve of the analytical impedance model (time domain, nonlinear). All simulation parameters are listed in figure A.1

The impedance was calculated from the drive voltage and current flow into the CMUT. All design, input and result data is shown in figure A.1. Based on the known drive voltage, the analytical model for the impedance of the CMUT in time domain was fit to the simulation result of the hybrid FE-based model.

A best-fit algorithm with the parameters C_m, C_A, D_A, f_0 and K_{SH} delivers a very good agreement between the impedance curves (figure 5.3). Only in the phase information small differences appear.

5.1.5 Frequency Domain Solution

Still depending on the input signal, the model is difficult to solve analytically in time domain. The aim of this section is to find an analytical solution directly in the frequency domain, which also represents the impedance measurement result from an impedance analyzer. The measurement procedure and results will be discussed in section 5.2.1 in more detail. For the following solution, it has to be considered, that the impedance analyzer performs a sine sweep and only evaluates the impedance at the current sweep frequency. For transferring the solution of the analytic impedance model into the frequency domain, a sinusoid input voltage and corresponding capacity change are used:

$$U_S(t,\omega) = U_{DC} + U_{AC}e^{j\omega t}, \tag{5.16}$$

$$C(t,\omega) = C_m + |\underline{C}_A(\omega)|e^{j\omega t+\varphi}. \tag{5.17}$$

The current flow can be calculated by inserting these equations into equation (5.14):

$$\underline{i}(t,\omega) = \underbrace{j\omega U_{AC}C_m e^{j\omega t}}_{\text{Static capacity}} + \underbrace{j\omega U_{DC}|\underline{C}_A(\omega)|e^{j(\omega t+\varphi(\omega))}}_{\text{Dynamic capacity}} + \underbrace{j2\omega|\underline{C}_A(\omega)|U_{AC}e^{j(2\omega t+\varphi(\omega))}}_{\text{Second harmonic}}. \tag{5.18}$$

Based on equations (5.16) and (5.18), the impedance $\underline{Z}$ is:

$$\underline{Z}(t,\omega) = \frac{U_{DC} + U_{AC}e^{j\omega t}}{j\omega U_{AC}C_m e^{j\omega t} + j\omega U_{DC}|\underline{C}_A(\omega)|e^{j(\omega t+\varphi(\omega))} + j2\omega|\underline{C}_A(\omega)|U_{AC}e^{j(2\omega t+\varphi(\omega))}}. \tag{5.19}$$

The impedance analyzer performs a sine sweep. For that reason, the influence of the static, dynamic and second harmonic component of the capacity is separated in the measured impedance curve (figure 5.4).

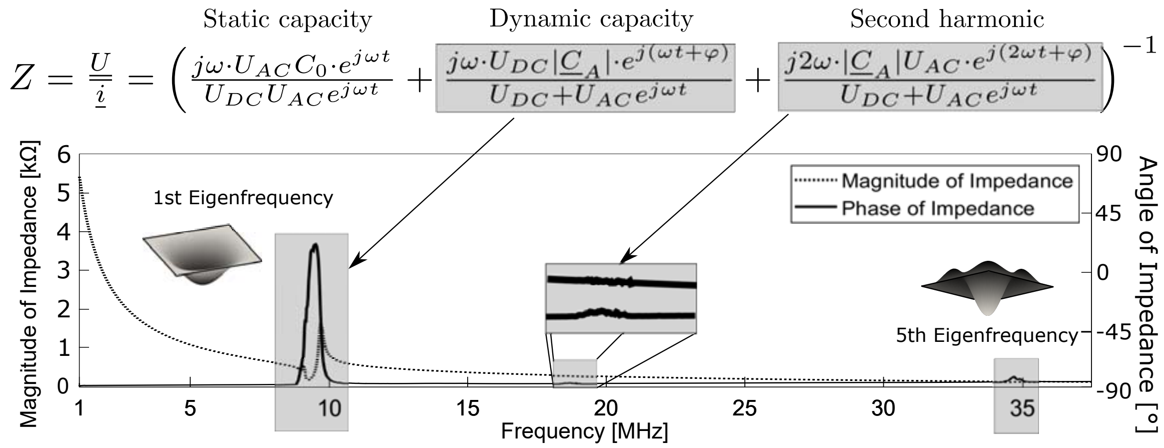

Figure 5.4: Measured impedance curve (magnitude and phase) vs. frequency using a sine sweep as voltage excitation signal.

The current and, therefore, the impedance consists of three parts as also shown in figure 5.4. The first and dominating contribution is caused by the static capacity, which is charged and discharged by the applied AC voltage. The second part represents the current, which flows due to the capacity change within the CMUT and, therewith, represents the dynamic behavior of the CMUT plate. The third part is a second harmonic, which is generated by the superposition of the drive voltage and the capacity change. As the second harmonic oscillates at twice the excitation frequency, the impedance analyzer is not sensitive to this component while measuring the first harmonic. Respecting this fact, the measured current $\underline{i}_{IA}$ of the impedance analyzer $\underline{i}_{IA}$ becomes:

$$\underline{i}_{IA}(\omega, t) = j\omega\left(U_{AC}C_m e^{j\omega t} + U_{DC}|\underline{C}_A(\omega)|e^{j(\omega t+\varphi(\omega))}\right). \tag{5.20}$$

From this equation, a closed analytical form for the complex impedance $\underline{Z}_{IA}$ measured by the impedance analyzer can be obtained:

$$\begin{aligned}\underline{Z}_{IA}(\omega) = \frac{\underline{U}_{IA}(\omega)}{\underline{i}_{IA}(\omega)} &= \frac{U_{AC}e^{j\omega t}}{j\omega\left(U_{AC}C_m e^{j\omega t} + U_{DC}|\underline{C}_A(\omega)|e^{j(\omega t+\varphi(\omega))}\right)}\\ &= \frac{1}{j\omega}\cdot\frac{U_{AC}}{U_{AC}C_m + U_{DC}|\underline{C}_A(\omega)|e^{j\varphi(\omega)}}.\end{aligned} \tag{5.21}$$

Here, the time-dependency disappears due to the simplification of ignoring the second harmonic generation. The parameters U_{AC} and U_{DC} are the voltages applied in the impedance measurement. The capacity C_m can be obtained by a static capacity measurement. The magnitude of the frequency-dependent capacity $|\underline{C}_A(\omega)|$ and the corresponding phase angle $\varphi(\omega)$ are the more interesting quantities, as they are directly linked to the mechanical characteristics of the plate. Therefore, they are coupled to the transfer function $H_{w/F}(\omega)$ of the mass-spring-damper system:

$$\begin{aligned}\underline{H}_{w/F}(\omega) = \frac{\underline{w}_A(\omega)}{\underline{F}_A(\omega)} &= \frac{1}{(j\omega)^2 M_A + j\omega D_A + K_A} \\ &= \frac{1}{M_A} \cdot \frac{1}{\omega_0^2 - \omega^2 + 2jD_A\omega_0\omega}.\end{aligned} \tag{5.22}$$

Equation (5.22) is the modal form of the transfer function of a damped spring mass oscillator. Three parameters have to be determined: the (undamped) resonance frequency ω_0, the damping ratio D_A and the modal dynamic mass M_A.

To transfer the dynamic capacity into frequency domain, equation (5.5) is used:

$$\begin{aligned}|\underline{C}_A(\omega)|e^{-j\varphi(\omega)} &= \mathcal{F}\left\{C_A(t, w_A, d_{eff})\right\} \\ &= \mathcal{F}\left\{\frac{\epsilon_0 \cdot A_{equ}}{d_{eff}^2 - d_{eff}w_A(t)} w_A(t)\right\} \approx \mathcal{F}\left\{\frac{\epsilon_0 \cdot A_{equ}}{d_{eff}^2} w_A(t)\right\}.\end{aligned} \tag{5.23}$$

Using a variable K_4 to replace all constant parameters in equation (5.23) the linearized dynamic capacity C_A becomes proportional to the deflection w_A:

$$|\underline{C}_A(\omega)|e^{-j\varphi(\omega)} = K_4\mathcal{F}\{w_A(t)\}. \tag{5.24}$$

For large deflections, equation (5.23) shows the limitations of the linear model and cannot be applied.

Using the modal capacity change $\underline{C}_{A,0} = \underline{C}_A(\omega_0)$, which represents the dynamic capacity oscillation only at the resonance frequency, eliminates the constant K_4:

$$|\underline{C}_A(\omega)|e^{-j\varphi(\omega)} = \underline{C}_{Ad,0}\frac{\underline{w}_A(\omega)}{\underline{w}_A(\omega_0)}. \tag{5.25}$$

Now, the transfer function from equation (5.22) of the mass-spring-damper system can be inserted:

$$|\underline{C}_A(\omega)|e^{-j\varphi(\omega)} = \underline{C}_{A,0}\frac{\underline{F}(\omega)}{\underline{F}(\omega_0)}\frac{\underline{H}_{w/F}(\omega)}{\underline{H}_{w/F}(\omega_0)}. \tag{5.26}$$

The impedance analyzer performs a sweep with constant U_{AC}-voltage amplitude. Therefore, the spectral amplitude of the force is constant:

$$F(\omega) \sim U^2(\omega) = U_{AC}^2. \tag{5.27}$$

Then, the dynamic capacity change C_A becomes:

$$|\underline{C}_A(\omega)|e^{j\varphi(\omega)} = \underline{C}_{Ad,0} \cdot \frac{2D\omega_0^2 \cdot \sqrt{1-D^2}}{\omega_0^2 - \omega^2 + 2jD_A\omega_0\omega}. \tag{5.28}$$

The resulting value for $|\underline{C}_A(\omega)|$ is accurate, but linearized in the operating point for both, voltage excitation and the relation between deflection and capacity. Inserting equation (5.28) in equation (5.21) allows to analytically calculate the impedance curve of a CMUT:

$$\underline{Z}_{IA}(\omega) = \frac{1}{j\omega} \cdot \frac{U_{AC}}{U_{AC}C_m + U_{DC}\underline{C}_{A,0} \cdot \frac{2D\omega_0^2 \cdot \sqrt{1-D^2}}{\omega_0^2 - \omega^2 + 2jD_A\omega_0\omega}}. \tag{5.29}$$

Four parameters describing the electrical and mechanical characteristics of the CMUT and two parameters for the corresponding drive voltages are used:

- the parallel capacity (including parasitic capacities) C_m,
- the capacity change $\underline{C}_{A,0}$ in the (damped) resonance frequency,
- the mechanic and acoustic damping coefficient D_A,
- the undamped angular eigenfrequency ω_0,
- the DC bias voltage U_{DC}
- the amplitude of applied excitation voltage U_{AC}.

5.2 Measurement and Analysis of the Electrical Impedance

The electrical impedance measurement is often the first characterization step, as no immersion is necessary and a basic acoustic characterization is possible from the knowledge of the impedance curve.

5.2.1 Measurement of the Electrical Impedance

For all impedance measurements, a Wayne Keer 6520B impedance analyzer was used. However, the device is able to deliver a bias voltage only up to $40\,\mathrm{V}$, which is too low for the characterization of most of the CMUT designs. Thus, an external bias tee was used as specified in figure B.2 [Agi09, Figure 5-46]. With a $1\,\mu\mathrm{F}$ blocking capacitor it is useable in the frequency range above $50\,\mathrm{kHz}$. After calibration, the bias tee allows to measure the impedance up to a frequency of $35\,\mathrm{MHz}$. The reason for this is the low-pass character between the input voltage and the voltage at the device under test (DUT) of the bias tee as shown in figure 5.5. The voltage transfer function H_f was measured with a sine sweep at an amplitude of $1\,\mathrm{V}$, as the impedance analyzer also uses the same signal to measure the impedance of the DUT.

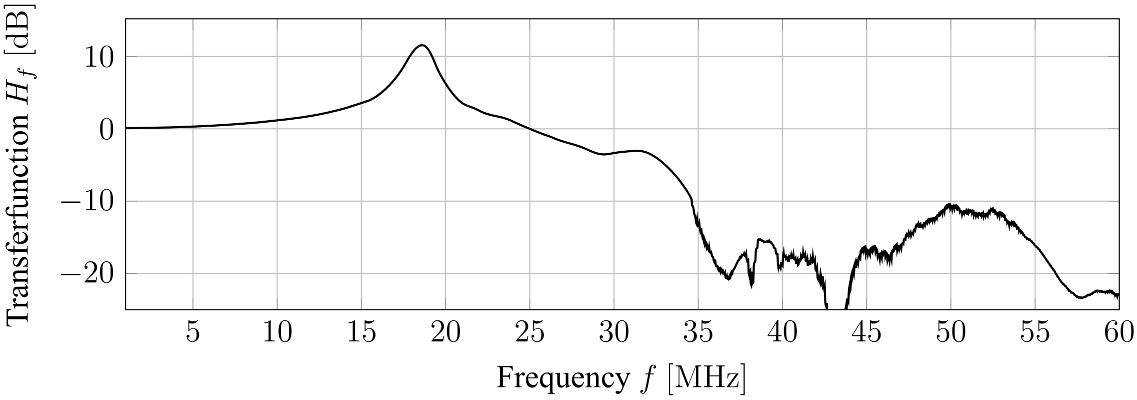

Figure 5.5: Voltage transfer function of the bias tee for impedance measurements with a load of $20\,\mathrm{pF}$

The full lab setup is shown in figure 5.6. The impedance analyzer and a DC voltage source are connected to the self-built bias tee. A chip socket is soldered on a printed circuit board (PCB), where the CMUT chip is mounted. The array element to be measured can be selected by multi-pin connector on the PCB. The impedance analyzer is calibrated by inserting the calibration standards directly into the chip socket. Thus, the measured impedance contains not only the impedance of the CMUTs, but also the ones of the chip carrier, the wire bonds and the parasitic impedances within the CMUT chip.

a) Schematic representation of measurement setup

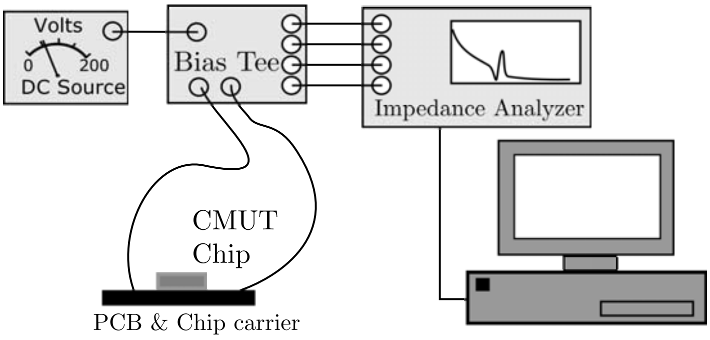

b) Photo of measurement setup used

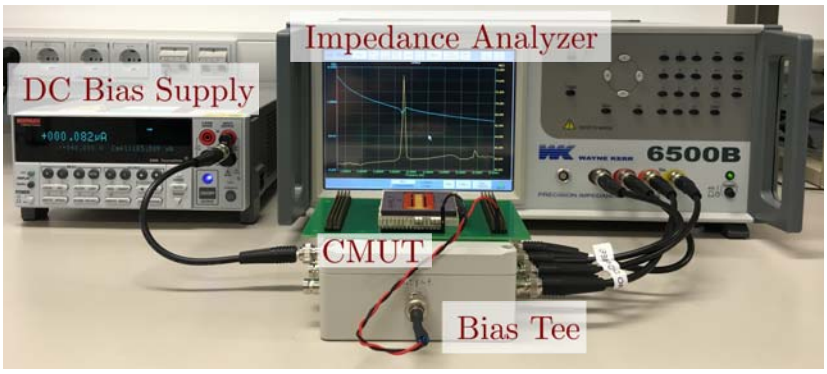

Figure 5.6: Schematic and photograph impedance measurement setup for packaged CMUT chips (see also table B.5)

The measurement time is basically defined by the sweep time and the number of frequency bins. To increase the quality of the results at a minimum measurement duration, two measurements are performed. First, a very wide frequency range is scanned with low resolution and the maximum of the phase of the impedance $\max(\arg\{\underline{Z}\})$ is identified. The corresponding frequency indicates the resonance frequency f_0 of the CMUT. Then the range around f_0 is scanned again with a higher spectral resolution and the results of both scans are merged.

The full setup is controlled by a self-built Matlab/C#-based interface, which allows to configure all device parameters and to run the measurement automatically.

Figure 5.7 shows a typical result of an impedance measurement at different bias voltages for one array element. Aside from the CMUT's resonance frequency, the device acts like a static capacitor and the impedance can be described by:

$$Z = \frac{1}{2\pi f \cdot C_0}. \tag{5.30}$$

Reaching the resonance frequency, the magnitude of the impedance first decreases to a minimum (resonance f_{01}), then rises to a local maximum (antiresonance at f_{02}) and returns to the impedance curve of the static capacity. The phase of the impedance reaches a maximum (inductive) value in between the two resonance frequencies f_{01} and f_{02}. With increasing bias voltage, the impedance peak increases, as the same plate displacement creates a larger capacity change. Also, the resonance frequency of the CMUT decreases with rising DC bias voltage due to the spring-softening effect [Loh05]. As the CMUTs at the center, edge and corner of an array element have a different boundary stiffness, the resulting resonance frequency change due to the spring softening is different. The CMUT cells of unequal characteristics within an array element can be separated in the impedance curve, because more than one impedance peak occurs.

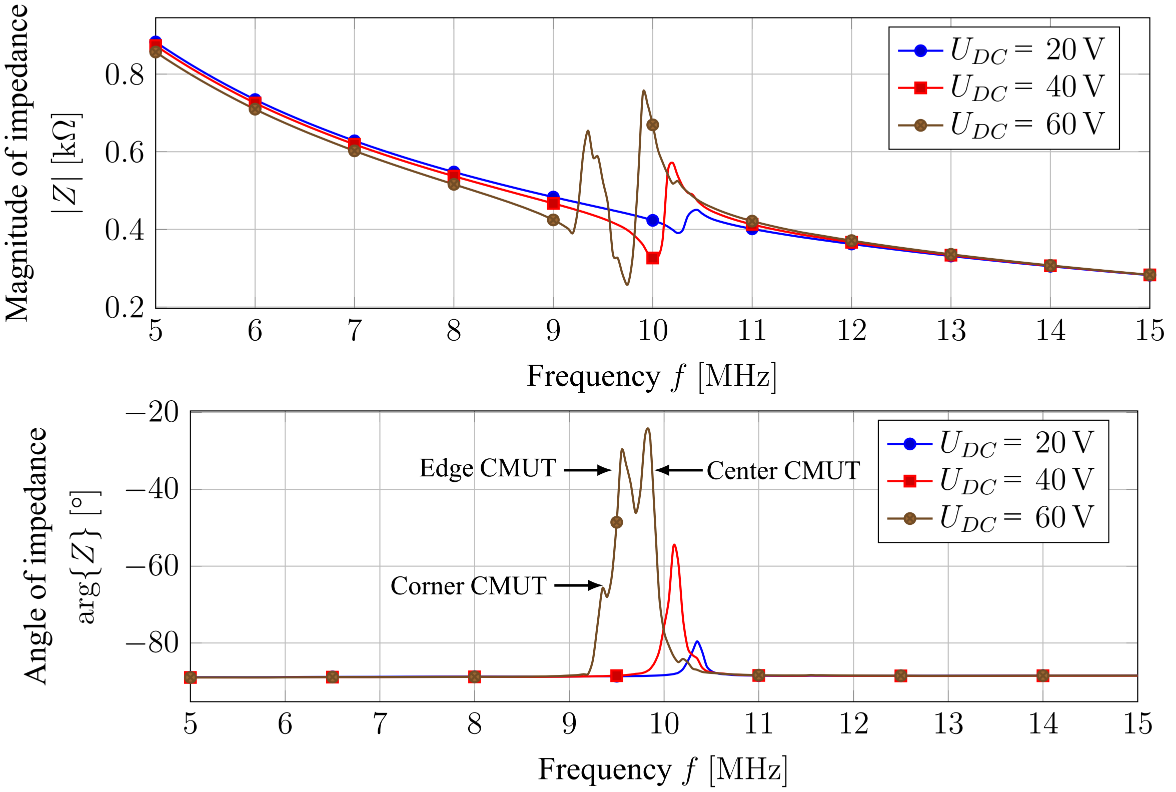

Figure 5.7: Measured impedance of one array element at different bias voltages (CMUT design 1 in table B.6).

5.2.2 Analysis using the Analytical Impedance Model

The measured impedance curves have been analyzed using the analytical model described in section 5.1.5. In figure 5.8, the measured impedance and the fitted curve are shown for different bias voltages. For the measurement, a drive voltage of $U_{AC} = 1\,\mathrm{V}$ was used. In table 5.2 the resulting parameters are listed according to the curves in figure 5.8. The CMUT design parameters are shown in table B.6, design 1.

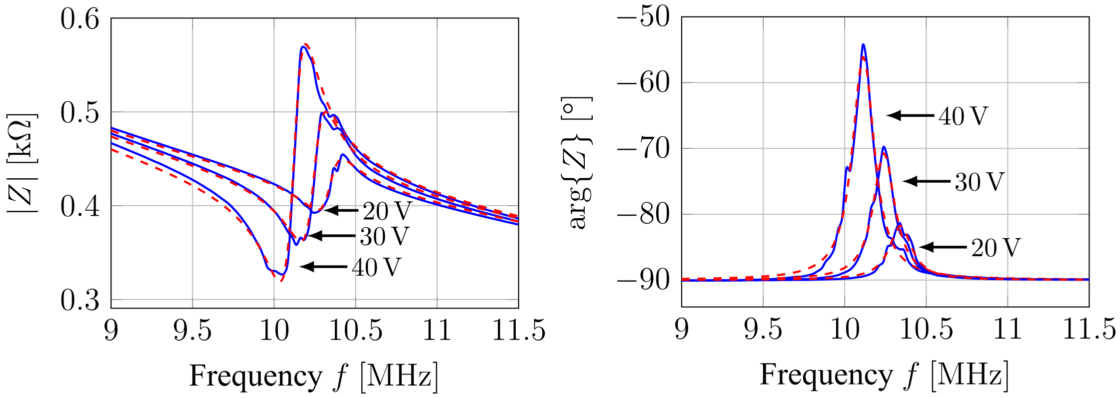

Figure 5.8: Measured and fitted magnitude and phase of the impedance for one array element at different bias voltages at $U_{AC} = 1\,\mathrm{V}$ (see also table 5.2, design 1)

Table 5.2: Resulting fit parameters for approximating the model to measured impedance curves at different drive voltages U_{DC} and U_{AC}. The values correspond to one full CMUT array element with 110 CMUTs operating in parallel (table 5.2, design 1).

U_{AC}	0.5 V				1.0 V			
U_{DC} [V]	C_m [pF]	$\lvert\underline{C}_{Ad,0}\rvert$ [fF]	D_A [-]	f_0 [MHz]	C_m [pF]	$\lvert\underline{C}_{Ad,0}\rvert$ [fF]	D_A [-]	f_0 [MHz]
20.0	36.48	131	0.0162	10.33	36.22	264	0.0162	10.33
25.0	36.45	169	0.0157	10.29	36.16	346	0.0157	10.28
30.0	36.49	207	0.0153	10.22	36.19	426	0.0160	10.22
35.0	36.51	239	0.0153	10.16	36.20	484	0.0173	10.15
40.0	36.56	278	0.0154	10.09	36.20	562	0.0182	10.07

Table 5.2 demonstrates the reaction of the CMUT for different drive voltages. With rising AC and DC voltage, the dynamic capacity $\lvert\underline{C}_{Ad,0}\rvert$ increases, because the dynamic deflection of the plate becomes larger. The resonance frequency f_0 drops with increasing bias voltage due to the electrostatic spring-softening effect. The static capacity C_m is nearly constant at low DC levels. Here, it has to be taken into account, that, due to the linearization, the dynamic capacity counteracts the rise of the static capacity C_m in the model.

5.2.3 Measurement Results

a) Resonance Frequency and Pull-in Voltage

The impedance measurement in air allows to measure both, the resonance frequency f_0 and the pull-in voltage U_{PI} of a CMUT. Therefore, the DC bias voltage U_{DC} is increased until the resonant peak of the first eigenmode disappears. Also, an extrapolation of the pull-in voltage U_{PI} from the spring-softening effect is possible by measuring the resonance frequency at different bias voltages. Then equation (5.31) can be fitted to find the parameters U_{PI} and the resonance frequency f_0 at zero DC bias voltage [Loh05, equ (3.84)]:

$$U_{PI} = U_{DC} \cdot \frac{3 - {f_{rel}}^2}{3\sqrt{3}} \sqrt{\frac{3 - f_{rel}^2}{1 - f_{rel}^2}}; \tag{5.31}$$

$$f_{rel} = \frac{f_0(U_{DC} = U_{DC})}{f_0(U_{DC} = 0\text{V})}. \tag{5.32}$$

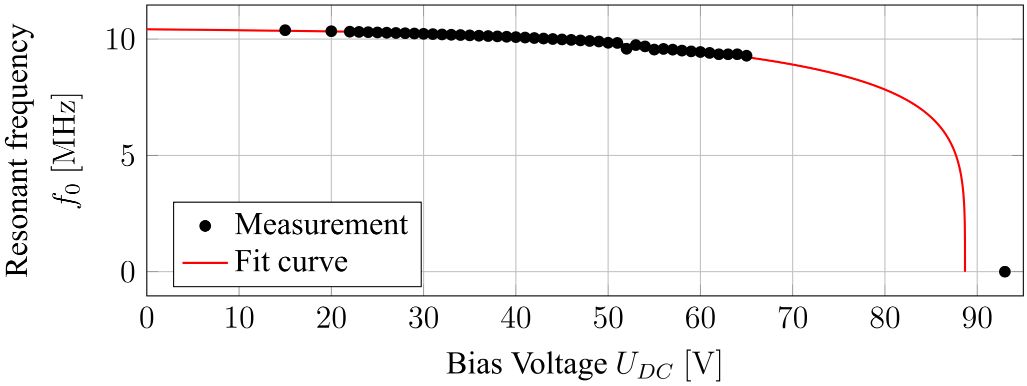

Figure 5.9: Resonance frequency f_0 determined from measured impedance curves (table 5.2, design 1) using the analytic impedance model from section 5.1.5 and fit of equation (5.31)

The prediction of the pull-in voltage U_{PI} is accurate, even if only resonance frequencies are measured at bias voltages between 15% and 70% of the pull-in voltage U_{PI} are used as data basis for a function fit. For small bias voltages, no distinguishable resonant peak could be extracted from the impedance measurements, which makes the resonance frequency difficult to identify. At high bias voltages, more than one peak appears in the impedance curve, as within one array element the CMUTs at the center, edge and corner are slightly different. In such cases, the fit of the analytical impedance model is not possible, as only one degree of freedom (and therefore one CMUT cell type) is supported.

b) Quality Factor

Especially for CMUTs in air-borne applications, the quality factor in air is an important physical property. However, the quality factor is usually calculated by fitting a Butterworth-van-Dyke equivalent circuit to a measured impedance curve (see section 5.1.1). Then either the short- or the open-circuit resonance is used to calculate the quality factor Q [Par+11]. Physically, there is only one resonance - the bending of the plate in its eigenmode. The supposed two resonance frequencies (open- and short-circuit resonance) in the impedance curve are no mechanical resonant phenomena. They appear due to the frequency-dependent phase shift $\varphi(\omega)$ between excitation voltage and plate displacement.

The quality factor Q is the fraction of the mechanical energy stored in the plate and the energy loss of the plate. Both are directly linked to the damping coefficient D_A derived by the analytical impedance model (see figure 5.2):

$$Q = \frac{f_0}{B} = \frac{1}{2D_A}. \tag{5.33}$$

The quality factor Q of the measured CMUT array (table 5.2) amounts to about 30 and does not significantly change with the applied voltages.

c) Coupling Coefficient

The coupling coefficient k_T describes the transformation ratio between mechanical energy E_{mech} and the total energy E_{total} stored in the CMUT. This equals the ratio between the so called fixed C_s and free capacity C_T at a given DC voltage [Yar+03].

$$k_T^2 = \frac{E_{mech}}{E_{total}} = 1 - \frac{C_S}{C_T}. \tag{5.34}$$

The coupling coefficient k_T^2 compares the parasitic capacity of a CMUT with the dynamic capacity. Here, the current transfer function H_i is used as equivalent parameter. It is defined as relation between the current i_A created due to the capacity change and the total current flow at the CMUT. Thereby the total current consists of the flow i_S due to the (parasitic) static capacity and the flow i_A caused by the dynamic capacity change. For a sinusoidal drive voltage, the current flow becomes:

$$i_S = C_m \frac{\mathrm{d}U}{\mathrm{d}t} = 2\pi f_0 \cdot U_{AC} C_m \cos\left(2\pi f_0 t\right), \tag{5.35}$$

$$i_A = U_{DC} \frac{\mathrm{d}C}{\mathrm{d}t} = 2\pi f_0 \cdot U_{DC} |\underline{C}_{Ad,0}| \cos\left(2\pi f_0 t\right). \tag{5.36}$$

The transfer function H_i determines the electrical efficiency of a CMUT. It shows, which fraction of the current delivered by an electrical source is converted into a dynamic capacity change:

$$H_i = \frac{i_A}{i_S + i_A} = \frac{|\underline{C}_{Ad,0}| \cdot U_{DC}}{C_m \cdot U_{AC} + |\underline{C}_{Ad,0}| \cdot U_{DC}}. \tag{5.37}$$

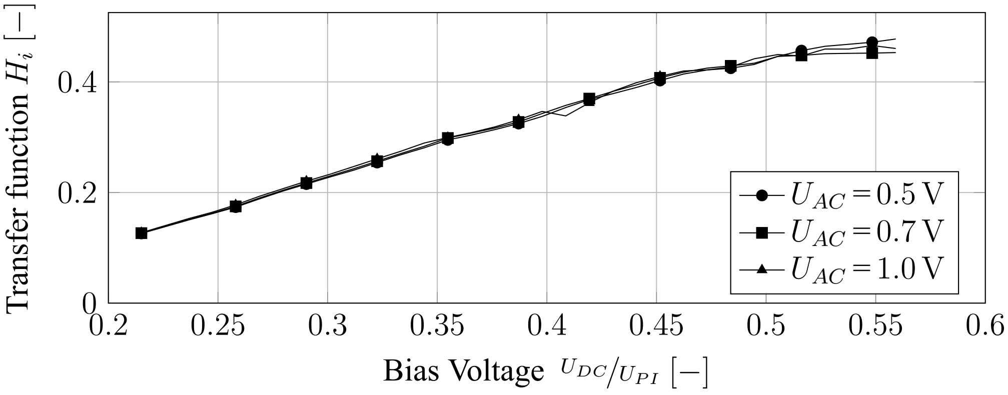

Figure 5.10: Current transfer function H_i for one CMUT array element based on measurements for different drive voltages U_{AC} (design 1 of table 5.2).

Figure 5.10 shows clearly, that the amount of current i_A due to the dynamic deflection of the CMUT plate rises with increasing bias voltage U_{DC}. Increasing the AC voltage U_{AC} does not lead to a more effective transducer, as long as the assumption of a linear regime holds.

To compare different CMUT designs, the transfer function H_i provides an information about the displacement at the resonance frequency. As discussed in section 3.2, also the bandwidth of the transducer has to be evaluated. The gain-bandwidth product GBP is adopted to this methodology by multiplying the current transfer function H_i with the fractional bandwidth of the CMUT[1].

$$GBP_i = H_i \cdot \frac{B}{f_0} = H_i \cdot 2D_A = \frac{2D_A \cdot |\underline{C}_{Ad,0}| U_{DC}}{C_m U_{AC} + |\underline{C}_{Ad,0}| U_{DC}} \tag{5.38}$$

---

[1] The transformation $GPB \rightarrow GBP_i$ inherits also a change of the unit from [V Hz] to [-].

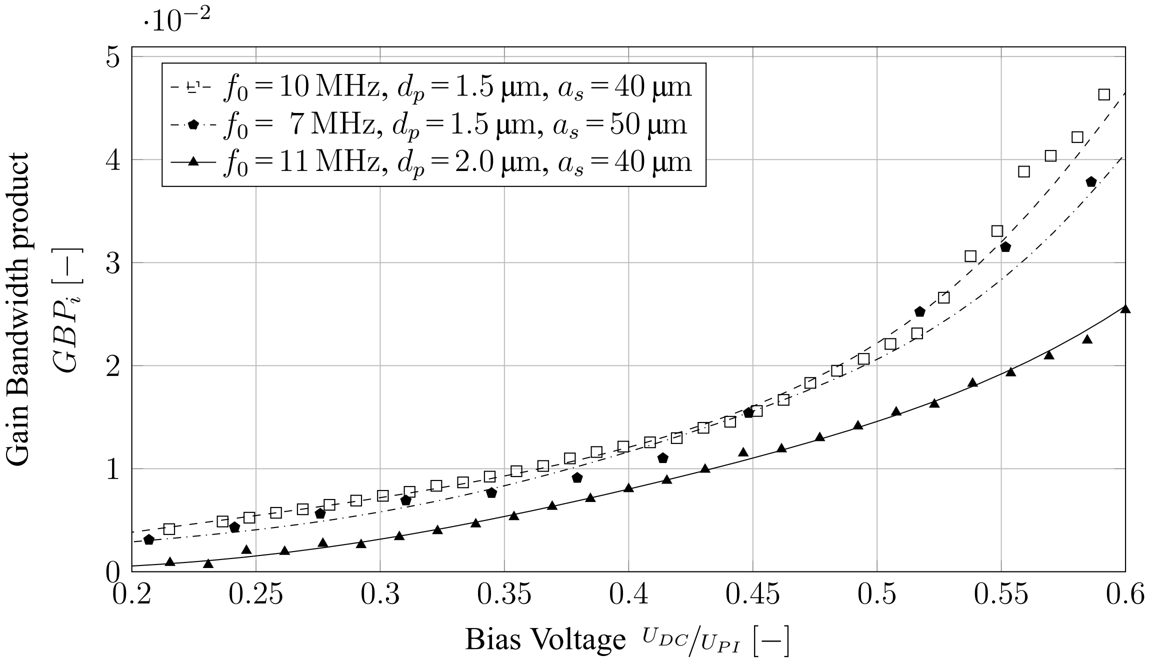

Figure 5.11: Gain-bandwidth product GBP_i based on measurements for different plate thicknesses and plate diameters (see also table 5.2)

The evaluation of GBP_i over the bias voltage confirms the conclusions from section 3.2, that changing the plate diameter has major impact on the resonance frequency, but has minor effect on the acoustic characteristics (in air) within the given design space. The CMUTs with a thinner plate offer a higher value of GBP_i and transfer more electrical energy into acoustic energy. The main reason for this is the better adaption of the mechanical impedance of the plate to the acoustic impedance of air.

The analytic model for the impedance of CMUT allows to determine the main characteristics of the CMUT design in air such as resonance frequency, nonlinearity and bandwidth in air and compare different CMUT design variants to each other. An adaption of the gain-bandwidth product is established as indicator for the electroacoustic efficiency of CMUTs.

5.3 Electrical Wafer Level Impedance Test for Chip Quality Investigation

This section is based on results already published in [Kle+15a].

In a production environment, it is necessary to verify the quality and proper functioning of the extraditable CMUT chips. Therefore, in principle two methods are useable.

The first one is the extraction of acoustic parameters such as send and receive sensitivity and compare them against a previously defined limit. This is the most reliable way on validating parameters given in a data sheet or specification book, but also the most complex method. In addition, it is difficult to verify the acoustic properties of a CMUT which is desired to operate in immersion without the real acoustic load before packaging.

For the second method, one CMUT design, which fulfills all the required specifications, can be treated as reference. Then, all further produced devices are compared against this reference. An indicator for the comparison has to be chosen, which inherits all relevant acoustic characteristics. In case of CMUTs, the impedance can be an indicator to use, as it is influenced by the electrical, mechanical and acoustical characteristic of the CMUT.

The effect of deviations in production on the electrical impedance is shown in table 5.3. A full acoustic characterization of a CMUT cell (especially in immersion) only from the electrical impedance is not possible, as the acoustic load and the drive voltages differ from the real application. Thus, differences in the impedance to a previous tested and characterized CMUT as reference allow to completely verify the equality of the acoustic characteristics and is a sufficient criterion for a chip quality assessment.

Table 5.3: Influence of fabrication tolerances on the electrical impedance of CMUT.

Effect	Possible Causes
Drift of ω_0	Variation in • thickness, • shape and anchor, • or stress of the mechanical plate.
Change of $\lvert Z\rvert$	Variation of • gap height, • thickness of dielectrics, • material properties of dielectrics, • parasitic capacities.
Very high $\lvert Z\rvert$ ($\lvert Z\rvert$>100 kΩ, f>1 MHz)	• The array element is broken. • The probe tips do not properly contact the bond pad.
Extreme low $\lvert Z\rvert$ ($\lvert Z\rvert$<10 Ω, f<100 MHz)	Broken CMUT cell creates an electrical short

5.3.1 Measurement Setup

The measurement setup used for the electrical impedance test as depicted in figure 5.12 is comparable to the configuration in figure 5.6. The bias tee is connected to probe needles (tungsten probe tips with $0.35\,\mu\mathrm{m}$ diameter), which contact the bond pads on the CMUT wafer. A semi-automatic probe station (Cascade Microtech PA200) and the software package Patmos[2] realize the automated stepping to measure the CMUT chips all over the wafer.

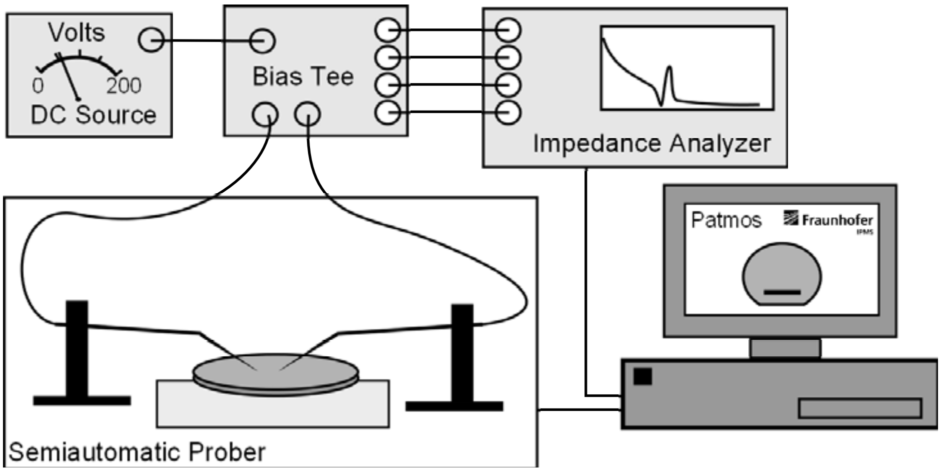

Figure 5.12: Wafer level impedance test setup

The measurement duration is a critical factor of the test, as one wafer contains 14,464 testable CMUT array elements for the used design. The test duration is basically dominated by the sweep time of the impedance analyzer.

The impedance analyzer supports four speed modes, which define the excitation time per frequency bin. To achieve an equilibrium state, the measurement speed level “fast” has to be used. Then the resulting impedance curve does not differ significantly from the measurement results obtained in “medium” or “slow” mode. The center frequency of the CMUTs to measure was greater than $3\,\mathrm{MHz}$. Assuming a fractional bandwidth in air of about $10\,\%$, the minimum bandwidth is $300\,\mathrm{kHz}$. Therefore, a minimal spectral resolution of about $15\,\mathrm{kHz}$ is used to cover the dynamic area of the CMUT with at least 20 frequency bins. Thus, the measurement was performed with 200 frequency bins for the full impedance curve. By measuring only 41 out of 128 array elements within a chip, the measurement duration for one wafer becomes less than three days. To verify that the outer elements within the array are working properly, the outer 10 elements and in between, every fifth element was tested (see figure 5.13).

---

[2] Software package to control the measurement setup; in-house developed by Fraunhofer IPMS

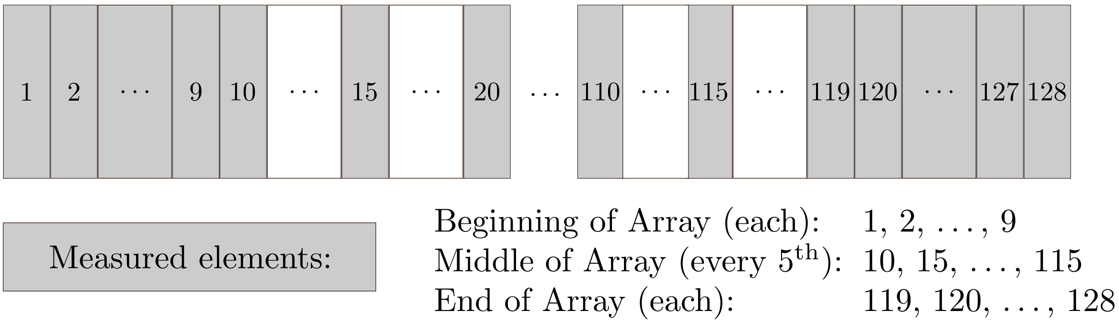

Figure 5.13: Measured array elements within one CMUT array

5.3.2 Processing of Impedance Curves

As discussed in the preface of section 5.3, the impedance data contains all characteristic information about the CMUT. The aim is to compare the measured impedance curve against a reference to generate a statement about the fabrication quality of the CMUT. Therefore, two different approaches are feasible.

- The two curves of the complex impedance are compared as abstract mathematical function without further physical interpretation. Therefore, a coherence analysis is developed and delivers a single number quality factor.
- A second possibility is the fit of lumped element models and a subsequent analysis of the resulting lumped parameters. This allows to derive a statement about the dynamic characteristics of the measured CMUT array element and derive a statement about the quality of the CMUT as well.

Both methods are introduced and explained here. The results of the analysis are shown in section 5.3.3.

a) Coherence Criterion as Quality Factor

The coherence γ^2 of two signals $(x1, x2)$ represents the cross spectral density between two signals:

$$\gamma^2(x_1, x_2) = \frac{|\langle \mathcal{F}\left\{x_1(t)\right\} \mathcal{F}\left\{x_2(t)\right\}^* \rangle|^2}{\langle |\mathcal{F}\left\{x_1(t)\right\}|^2 \rangle \cdot \langle |\mathcal{F}\left\{x_2(t)\right\}|^2 \rangle}. \tag{5.39}$$

The coherence equals one ($\gamma^2 = 1$) if a linear relation is present between the two signals and zero ($\gamma^2 = 0$) in case of complete linear independence between the signals. The idea is using the coherence γ^2 as an indicator for the equality of two measured impedance curves $(\underline{Z}_k, \underline{Z}_l)$:

$$\gamma^2(\underline{Z}_k, \underline{Z}_l) = \frac{|\langle \mathcal{F}\{\underline{Z}_k\}\, \mathcal{F}\{\underline{Z}_l\}^*\rangle|^2}{\langle|\mathcal{F}\{\underline{Z}_k\}|^2\rangle \cdot \langle|\mathcal{F}\{\underline{Z}_l\}|^2\rangle}. \tag{5.40}$$

Here, the coherence γ equals one, if both signals are equal or the relation between both can be described by a completely linear system. In this case, any change of bandwidth, peak-value, resonance frequency or static capacity adds a phase angle to the cross-spectral density between the 'signals' $\underline{Z}_k$ and $\underline{Z}_l$ and the coherence decreases. All measured impedance curves within one CMUT array are compared against each other by calculating the coherence γ^2. The information is stored in a coherence matrix Γ. For N measurements, Γ becomes a squared symmetric matrix of order N and the k-th row represents the results of the k-th measured array element.

The element quality q_{el} indicates, how well one array element fits into the CMUT array and is defined as the geometric mean of the k-th row of the coherence matrix Γ:

$$q_{el,k} = \left(\prod_{l=1}^{N} \Gamma_{(k,l)}\right)^{1/N}. \tag{5.41}$$

The conformity of the whole CMUT array can be distinguished by comparing all measured array elements against each other, which is defined by the geometric mean of all elements in the coherence matrix Γ. This quality is called local quality q_{lok}. The use of the geometric mean leads to a very low local quality even if only one array element is for example broken:

$$q_{lok} = \left(\prod_{k=1}^{N}\prod_{l=1}^{N} \Gamma_{(k,l)}\right)^{1/N^2} = \left(\prod_{k=1}^{N} q_{el,k}\right)^{1/N}. \tag{5.42}$$

A high local quality factor is a necessary, but not a sufficient condition for a properly fabricated CMUT chip. If for example all elements are shorted or the release process did not work, all elements will show a very equal impedance curve. The result is a very high quality factor even if no element is working. Therefore, the comparison against a reference impedance is necessary. This impedance $\underline{Z}_{ref}(\omega)$ can be predefined by simulation, by prior test results of a working device or calculated from the wafer-level test results.

To compare the impedance of the array to the impedance reference $\underline{Z}_{ref}(\omega)$, the mean impedance $\underline{Z}_m(\omega)$ of the array is calculated:

$$\underline{Z}_m(\omega) = \frac{1}{N}\sum_{i=1}^{N} \underline{Z}_i(\omega). \tag{5.43}$$

The global quality is the coherence between the mean impedance of the chip and the reference impedance:

$$q_{glob} = \gamma(Z_m, Z_{ref}). \tag{5.44}$$

From both information, the local and global quality, the resulting quality q_{res} is the final indicator for the proper operation of the CMUT array:

$$q_{res} = q_{glob} \cdot q_{lok}. \tag{5.45}$$

b) Lumped-Element Analysis as Quality Criterion

Another possibility to analyze the measured impedance of the CMUT elements is the use of lumped-element representations such as the Butterworth-van-Dyke equivalent circuit or the analytic model presented in section 5.1. Then an investigation of the resulting lumped parameters for any CMUT array element can be an indicator for the quality the CMUT. Therefore, not only deviations of a design from a reference can be detected but the full characteristics of the CMUT can be analyzed. Thus, the lumped-element analysis should be the preferred approach.

However, the implementation of this method on real data turns out to be difficult. For calculating the lumped parameters, an impedance curve has to be fitted to measured data. Therefore, the fit algorithm has to be very reliable and converge even on impedance data of a very small frequency range with low resolution. A second factor is, that the different boundary conditions within one CMUT array element create different types of CMUTs within one element, which superimpose in the measured impedance curve. Figure 5.14 shows the measured impedance on wafer level and a model fit (presented analytical impedance model). The deviation of the measured impedance curve from an ellipsoid is based on the different boundary conditions for the CMUT cells within the array element. This also creates a set of different solutions (local minimum error) for the used least-square algorithm.

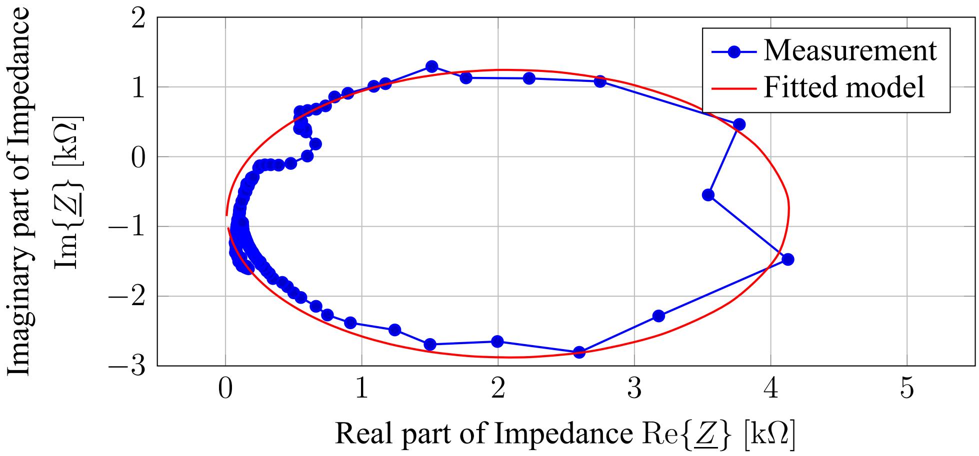

Figure 5.14: Measured and fitted impedance curves on wafer level for one array element

5.3.3 Results of Quality Analysis

Table 5.4 shows the measurement results for three chips of the same design from one wafer with different quality levels.

In chip one, all impedance curves nearly perfect match each other, which indicates, that this chip is very uniform. However, the fit of the model is not ideal, due to the different boundary conditions of the CMUTs within the array element.

For chip two, still all curves show working CMUT array elements. A small drift in the resonance frequency appears, but the peak amplitude of the impedance does not change. This chip is also considered as high quality. The small frequency drift does not matter in immersion. Still, the quality of chip two is slightly smaller than chip one.

Chip three contains some properly working CMUT array elements. However, some elements show a strange impedance curve with magnitudes 100 times higher than expected. For some measurements, it seems like, a parasitic insulating layer between bond pad and needle is breaking while running a sweep, because the impedance drops to the expected level. However, from this measurement results, this chip has to be marked as not useable, even if only a few elements behave irregular.

a) Coherence Criterion as Quality Factor

The quality indicator based on the coherence criterion was calculated for all three chips in table 5.4. As global impedance reference, the average impedance of another chip of high quality within the same design was used. Chip one shows the highest quality level, as the curves match each other and the used reference impedance as well. Due to the drift, the quality of chip two decreases slightly. The resulting quality value is bigger than $95\,\%$.

For chip three, only a few impedance curves differ from all other curves. However, these curves have great impact on the quality factor and the resulting quality drops below $80\,\%$. A more detailed analysis of chip three is shown in figure 5.15. From the coherence matrix Γ it can be seen easily, that eleven measured array elements show an abnormal impedance curve and lead to an element quality factor q_{el} of less than $70\,\%$ for those elements. In figure 5.15, all measured curves with an element quality smaller than $90\,\%$ are drawn in black. All peculiar curves have been identified by the algorithm.

Table 5.4: Quality factors for different chips (same design and wafer) and corresponding impedance curves (41 per chip). Black: Measured curves, gray: corresponding fit of the analytical impedance model.

Chip	Chip 1			Chip 2			Chip 3		
Quality	q_{lok}	q_{glob}	q_{res}	q_{lok}	q_{glob}	q_{res}	q_{lok}	q_{glob}	q_{res}
parameters	0.996	0.999	0.995	0.987	0.974	0.962	0.902	0.869	0.784

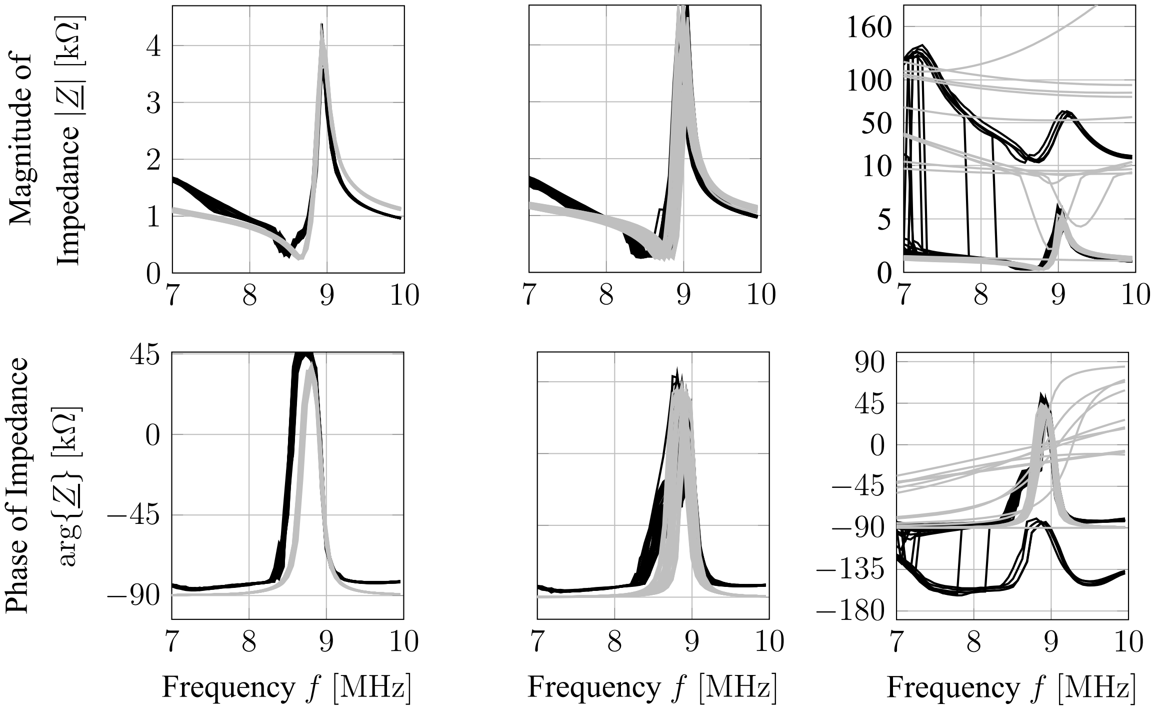

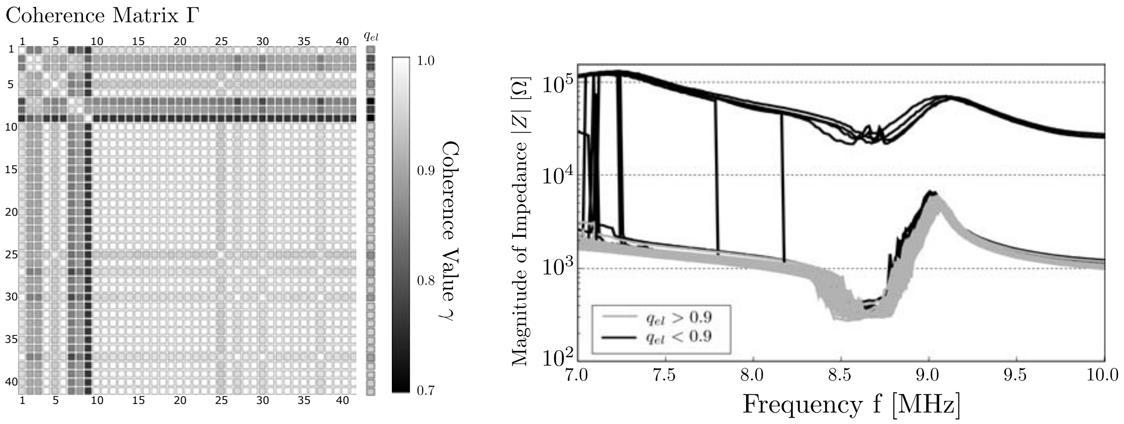

Figure 5.15: Coherence matrix Γ of chip three, quality factor of the array elements and corresponding impedance curves.

The result of the quality assessment based on the coherence criterion are shown in figure 5.16. The center of the wafer shows the best quality in terms of quality of the CMUT chips. At the borders, the quality decreases. Within the wafer, nine different CMUT designs were fabricated. The specifications of the designs are listed in table B.7 in the appendix.

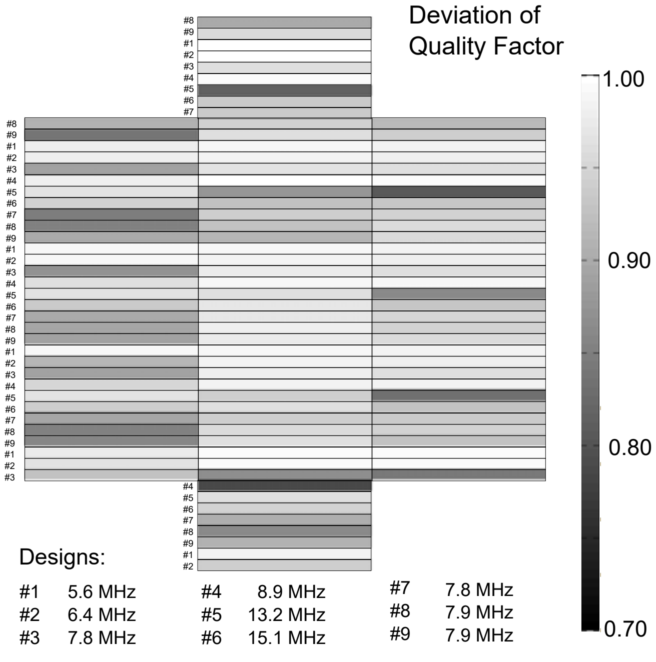

Figure 5.16: Deviation of resulting quality factor q_{res} for one wafer. $93.8\,\%$ of the chips show a resulting quality factor of $q_{res} > 0.85$

b) Lumped-Element Analysis as Quality Criterion

The lumped-element analysis has been performed using the Butterworth-van-Dyke equivalent circuit model and the analytical impedance model based on the spring-mass-damper system. However, both approaches deliver slightly different results depending on the initial conditions set to the fit algorithm. Not only the individual results for each impedance curve, but also the probability distribution changes by using another starting point for the fit. This fact has been verified using a Kolmogorov-Smirnov test on the extracted lumped parameters. However, a clear statement on the quality of the chips based on the lumped element analysis is not possible.

Table 5.5: Mean value and standard deviation of fitted lumped-circuit parameters for the CMUT chips shown in table 5.4

Mass-Spring-Damper Model

	C_0 [1 pF]	C_a [1 pF]	D [-]	$f0$ [1 MHz]
Chip 1	17.58 ± 0.21	1.75 ± 0.09	0.015 ± 0.0004	8.47 ± 0.011
Chip 2	16.97 ± 0.31	1.73 ± 0.18	0.012 ± 0.0012	8.77 ± 0.065
Chip 3	Fit does not converge			

Butterworth-van-Dyke Model

	C_p [1 pF]	C_s [1 pF]	R [1 Ω]	L [1 µH]
Chip 1	17.74 ± 0.60	1.04 ± 0.07	274 ± 21	325 ± 23
Chip 2	17.71 ± 0.65	1.19 ± 0.10	235 ± 21	283 ± 24
Chip 3	Fit does not converge			

5.3.4 Conclusions

The acoustic characteristics of CMUTs can be extracted from their electrical impedance. This incorporates the advantage of measuring on wafer-level before packaging and with less measurement efforts. Two different methods to judge the quality of a fabricated CMUT have been studied based on the electrical impedance.

The first approach is based on an analytical electromechanical model, which directly accesses acoustic parameters of a CMUT design. However, no sustainable quality-parameter could be extracted from the analysis results.

To compare the measured impedance of different CMUTs, a novel efficient method is developed. Based on a coherence criterion, a quality factor is assigned to each measured CMUT array. The procedure is optimized for high measurement throughput as thousands of CMUT array elements per wafer need to be tested. It is suitable for an automated acoustic end-of-line check and quality assurance for CMUT.

Chapter 6

Outlook

In this chapter, possible approaches to improve the performance of CMUT and promising applications are discussed. This inherits improvement of the send sound pressure, a measurement setup for acoustic characterization on wafer level and a multifrequency transducer suitable for acoustic spectroscopy.

6.1 Mechanically Interconnected CMUTs for Improved Send- and Receive Sensitivity

Within a collaboration of Fraunhofer IPMS and BTU Cottbus-Senftenberg, the idea of mechanically interconnected CMUTs (MICMUT) was initiated. [Kle+15b].

One weakness of current CMUT arrays is their low fill factor and thereby its small active aperture. For a circular CMUT cell, the average displacement within its cell diameter is about one third of the center displacement [WKK08]. In addition, at the border walls between the cells, no acoustic radiation is achieved. By interconnecting all CMUT cells within one array element by a radiating plate, the full area can be used for radiating and sensing sound (figure 6.1). Then, the full center displacement of the CMUT cells underneath is available for transmitting sound. This leads to a decisive increase of the send- and receive performance of CMUT transducers.

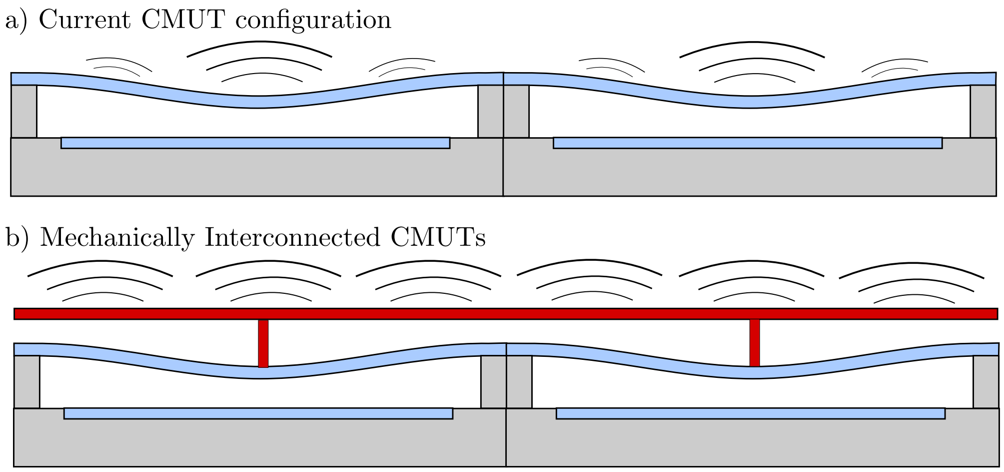

Figure 6.1: CMUT configuration a) without and b) with radiating plate (MICMUT)

Aside from the higher fill factor, there are two more advantages of a MICMUT against using a conventional CMUT. As the individual cells[1] are now electromechanical actuators, the plate diameter and the corresponding radiating area can be designed independent. Due to this fact, one more degree of freedom for design optimization is achieved.

Further advantages are:

- Ideal array geometries are achievable (see figure 6.2)
- Uniform characteristic all over the radiating surface, even if the individual actuators differ slightly from each other due to fabrication tolerances
- Use of the dynamic response (eigenmodes) of the radiating plate offers a further increase of the radiated sound pressure.

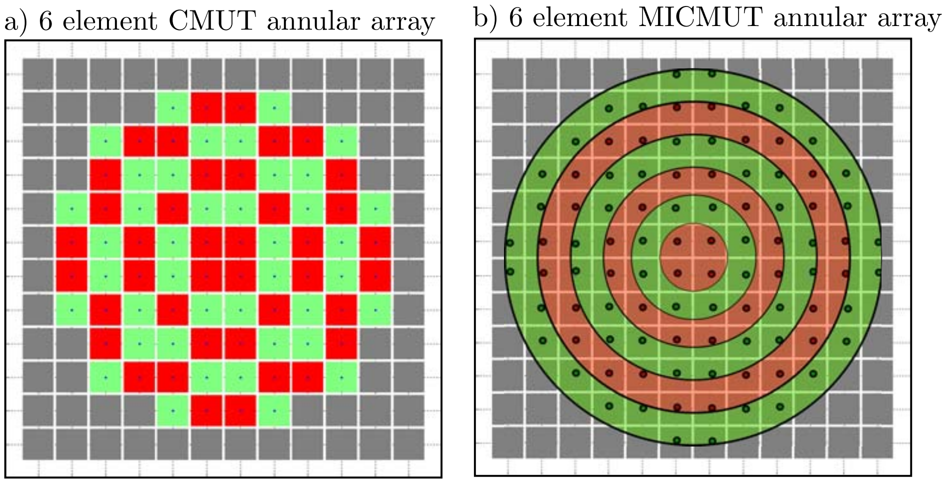

Figure 6.2: Annular array with rectangular CMUT and possible configuration as MICMUT transducer

---

[1] The term CMUT is not exact anymore for the cell connected to the radiating plate, as it is not a ultrasonic transducer itself anymore.

6.2 Improved Waver Level Acoustic Test

As CMUTs are fabricated on wafer level, an efficient test procedure in the production chain as early as possible is favored. In section 5.3, a test procedure for quality assessment based on the electrical impedance has been described. However, the sound pressure as central test parameter is not accessed. Vibrometry measurements (of CMUTs) on wafer level in air are state of the art [Plo06] for investigating the surface velocity, but no method to analyze the sound pressure with an appropriate acoustic load (immersion) is available yet.

Therefore, an acoustic tip can be used as shown in figure 6.3 [KU15]. The tip consists of four main parts: a contact head, an acoustic transmission medium, an acoustic backing and an acoustically hard housing.

Depending on the desired test procedure, another sound transmitter might be integrated into the tip (figure 6.3 a). If the CMUT acts as sound source, it emits an acoustic wave into the acoustic tip. The sound wave propagates through the contact head into the acoustic transmission medium and is sensed by the sound transmitter. From this signal, it is possible to calculate the send sensitivity of the CMUT.

For the investigation of the receive sensitivity, a sound signal has to be measured by the CMUT. This signal is generated by the sound transmitter, propagates through the tip and impacts the CMUT. From the receive signal, the receive sensitivity of the CMUT can be calculated. If only the combined send- and receive sensitivity (two-way insertion loss) is of interest, a simpler pulse-echo setup (figure 6.3 b) is sufficient.

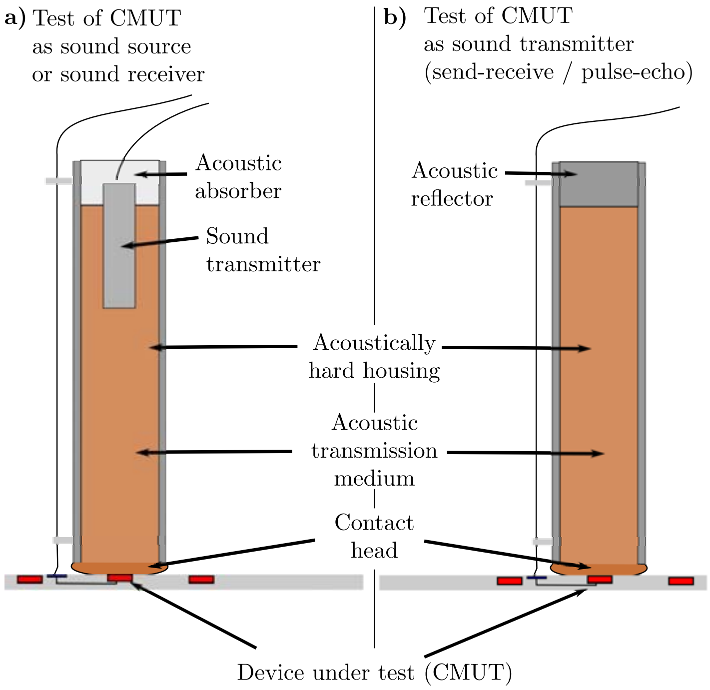

Figure 6.3: Acoustic tip for wafer level testing of sound sources or receivers (a) and transmitters (b).

However, for both types of the acoustic tip, a calibration is necessary to determine the frequency-dependent acoustic transfer function from the contact head to the sound transmitter or reflector. Therefore, the test has to be done using a reference transducer of known sensitivity. The transfer function can be estimated by using the model of Kundt's tube with lossy transfer medium.

The materials used for the transfer medium and the contact head depend on the desired test scenario. For airborne transducers, both parts are not necessary. In case of transducers used for medical applications, ultrasound-coupling pads as coupling element and water or silicone are possible transfer mediums. Even a stack of materials as used in a tissue phantom are suitable. In nondestructive testing of rigid materials, the transfer medium can be aluminum or steel. As contact pad, a thin silicon layer can be used similar to the coupling and matching layers used.

6.3 CMUT and Piezo Transducer Combination

CMUTs are plate transducers and therefore have a low impedance in comparison to piezoelectric bulk transducers. Thus, CMUTs offer a higher receive sensitivity, but are not able to generate a very high sound pressure. To overcome this limitation, CMUTs and piezoelectric transducers can be combined to a transmitter with both, high send and receive sensitivity. Figure 6.4 shows two possible configurations. In both, CMUT and piezo transducers are combined to one transducer element.

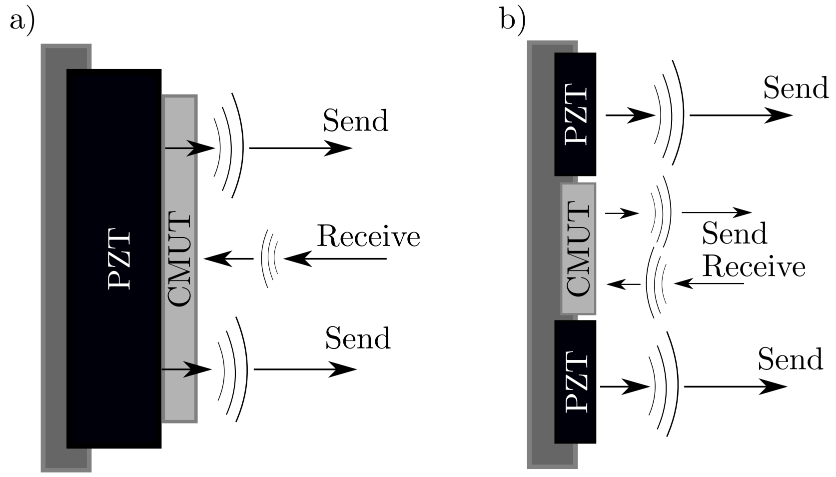

Figure 6.4: CMUT and PZT-based transducer integrated to one transducer element. In a), the CMUT is mounted directly on top of the PZT-element, in b) the CMUT and PZT-element are located next to each other

In figure 6.4a), the CMUT (array) is mounted directly on the piezoelectric element. When the PZT-element is excited by a drive voltage, the full CMUT chip is actuated and forms the radiating surface. As CMUT and piezo work in the same frequency range, the CMUT plate will not forward the acoustic energy, but deflect in the opposite direction. Thus, a big fraction of the energy emitted by the piezoelectric transducer will be reactive energy and not radiated into space. To counteract this effect, the CMUT can be used in pulled-in mode while the piezo is sending a signal and brought back into regular operation to receive the echo signal. Another possibility is to counteract the movement of the plate by a certain electrical drive signal, when the PCZ transducer is actuated.

Figure 6.4 b) shows an array consisting of piezoelectric and CMUT transducers. Again, the PZT-elements are used for sending ultrasonic signals and the CMUT operates as receiver. Depending on the configuration, it can be beneficial to also use the CMUT element as additional sound source. However, the CMUT design should be optimized for high receive sensitivity, because the radiated sound pressure by the CMUT will not contribute remarkably to the total sound pressure created by the piezoelectric element.

6.4 CMUT Transducer Optimized for Acoustic Spectroscopy

Acoustic (attenuation) spectroscopy is a method for analyzing the physical characteristics of a medium by measuring its acoustic damping coefficient α. A promising application is the analysis of machine oil using ultrasonic spectroscopy to detect, air-water emulsion, metal swarf and to monitor the viscosity and mass density of the oil. This can be used for early failure detection or oil quality surveillance.

Especially the scattering of the ultrasonic signal on particles depends mainly on the wavelength λ of the ultrasonic signal [Far51]. If the damping coefficient α rises nonlinearly at a certain frequency, this is an indication for the transition from Rayleigh- to Mie-scattering (figure 6.5). This fact can be used to determine the size and amount of the corresponding particles can be determined by a statistical analysis. For this, the damping coefficient α has to be accessed over a wide frequency range to extract information about particles of various sizes. In recent publications, a frequency range of $1...50\,\mathrm{MHz}$ is used [WSC15]. For a proper analysis of particles of less than $100\,\mu\mathrm{m}$ size, even higher frequencies up to $100\,\mathrm{MHz}$ are necessary [Ric08].

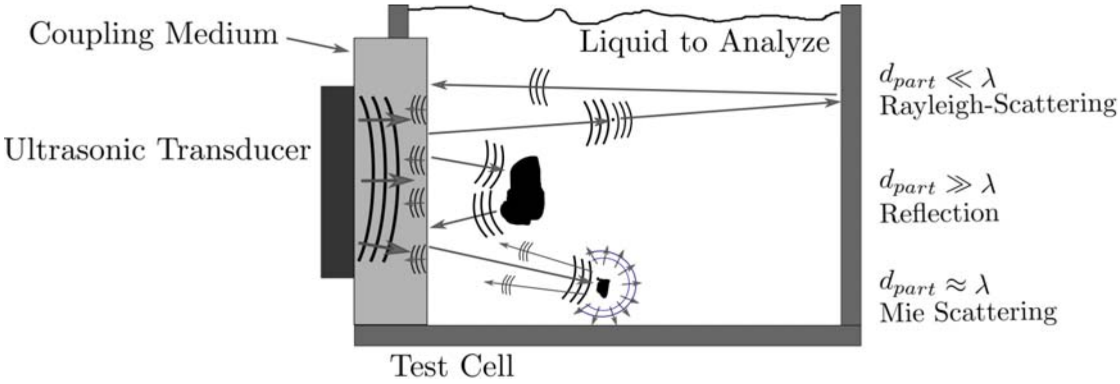

Figure 6.5: Interaction of an ultrasonic signal with particles of different sizes d_{part}.

For measuring the frequency-dependent attenuation $\alpha(f)$, an ultrasonic signal is transmitted into the medium to analyze and is received either by a second transducer (pitch-catch) or by the same transducer (pulse echo). The amplitude loss between sent and received signal indicates the frequency-dependent damping coefficient. For this, two types or transducers can be used. One option is the use of multiband resonant transducers which have certain eigenfrequencies with a high quality factor and allow to analyze a sample at different frequency bins spread in a wide frequency range. The second possibility is the application of wideband transducers (PZT composite or PVDF) with $100\,\%$ to $150\,\%$ fractional acoustic bandwidth [Yon+07].

The CMUT technology allows to design one transducer which involves multiple CMUT designs operating at different center frequencies. The arrangement is comparable to the composition of rings in piezoelectric ultrasonic transducers as proposed in [HH15]. With this ability, wide-band ultrasonic transducers with a bandwidth of more than $50\,\mathrm{MHz}$ are possible. The arrangement as annular array with one CMUT design per ring ensures the focus axial in front of the transducer (figure 6.6) for every frequency.

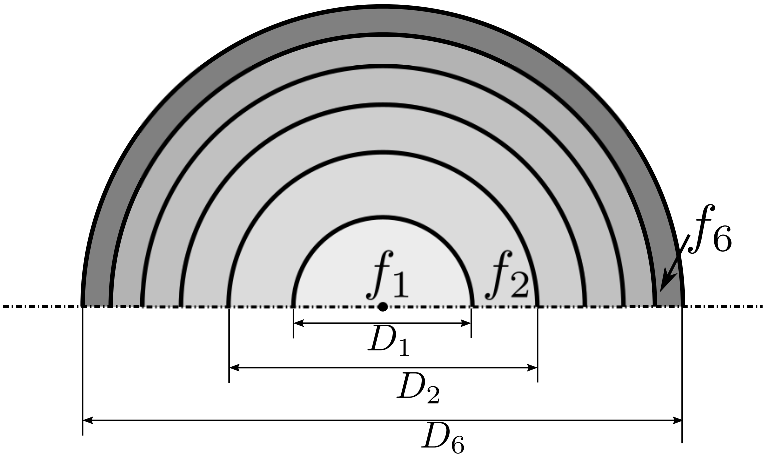

Figure 6.6: Annular array with six array elements. The diameter D_i of each element is adopted in a way, that every element shows the same active area.

Table 6.1 provides a rough estimation of a suitable design for an array with 10 array elements. Every ring has the same active area size. The center element contains the CMUT design with the highest center frequency f_m. The increase the aperture of the high frequency rings may be beneficial for materials with high acoustic damping. This compensates the increased acoustic absorption with rising frequency. For an estimation of a CMUT cell size, a diameter of $100\,\mu\mathrm{m}$ is assumed and all further designs are scaled accordingly $d_a \sim \sqrt{1/f_m}$. However, for the CMUT cell design, also the mechanical impedance and pull-in voltage of the CMUT design has to be taken into account and requires a more detailed analysis.

In conclusion, the generation of a multi-frequency ultrasonic transducers based on CMUT is challenging in both, simulation and fabrication. However, CMUT elements with a diameter from $10\,\mu\mathrm{m}$ to $50\,\mu\mathrm{m}$ have been successfully fabricated within the same wafer at Fraunhofer IPMS. The combination of a CMOS drive/receive circuit offers to send and receive in the full frequency band from $1\,\mathrm{MHz}$ to $100\,\mathrm{MHz}$. This would improve present transducers used for acoustic spectroscopy and would open new applications for this technology.

Table 6.1: Exemplary transducer design for a multi-frequency annular array operating from $1.7\,\mathrm{MHz}$ to $120\,\mathrm{MHz}$ with 15 array elements of equivalent active area

i	D [mm]	d_a [µm]	f_m [MHz]	f_{01} [MHz]	f_{02} [MHz]
1	3.16	13.4	111.0	55.5	166.5
2	4.47	16.8	71.1	35.5	106.6
3	5.48	21.0	45.5	22.7	68.2
4	6.32	26.2	29.1	14.6	43.7
5	7.07	32.8	18.6	9.3	27.9
6	7.75	41.0	11.9	6.0	17.9
7	8.37	51.2	7.6	3.8	11.4
8	8.94	64.0	4.9	2.4	7.3
9	9.49	80.0	3.1	1.6	4.7
10	10.00	100.0	2.0	1.0	3.0

i - Number of array element
D - Outer diameter the of array element
d_a - CMUT cell diameter, $d_a \sim \sqrt{1/f_m}$
f_m - Center frequency of CMUTs
f_{01} - Lower $-6\,\mathrm{dB}$ cut-off-frequency
f_{02} - Upper $-6\,\mathrm{dB}$ cut-off-frequency

Chapter 7

Conclusion and Perspectives

7.1 Summary of Results

CMUTs are promising to overcome drawbacks of current ultrasonic transducers as they offer, for example, a high receive sensitivity and the monolithical integration with CMOS integrated circuits, CMUTs are lead-free and can be fabricated cost-efficiently even in large array structures. However, deficits in the simulation, characterization and test of the acoustic characteristics of CMUT have been identified as weak points in the current product development process.

In this work, novel solutions for the acoustic simulation, design optimization, electro-acoustic characterization and end-of-line test of CMUTs have been achieved. Additionally, approaches for improving the performance of CMUTs using mechanically interconnected cells or combinations with piezo-based transducers are introduced. A special CMUT transducer design is developed optimized for acoustic spectroscopy and a novel wafer-level acoustic test-device are proposed.

7.1.1 Acoustic Simulation and Design Optimization

Chapter 3 shows a novel CMUT simulation model usable for design optimization of CMUT cells. It comprises the static and dynamic characteristics of CMUT cells and takes even fabrication effects such as (tensile in-plane) stress or the clamping stiffness of the CMUT flexure plate into account. Methodologies are derived to extract these parameters from deflection measurements and implement them into the hybrid simulation model or educe them for further analysis. The used structure-fluid coupling algorithm of the model accelerates simulation time in comparison to existing solutions.

An evolutionary optimization algorithm is proven to be appropriate for finding a CMUT design based on application-close specifications. In an exemplary optimization run, a CMUT cell design for acoustical imaging in tissue is generated.

7.1.2 Acoustic Characterization

Acoustic measurement procedures were presented to characterize CMUT transducers. A pitch-catch setup based on a reflector with an integrated hydrophone has been developed, which is capable of accurately measuring the send- and receive sensitivity of a CMUT cell design. Based on a drive signal with rectangular pulse shape, the send- and receive sensitivity have been measured as function of both, the frequency and the drive voltage. It has been demonstrated, that a high DC voltage and an additional AC pulse with the same polarization creates the highest sound pressure amplitude. In receive operation, the sensitivity of a CMUT and a hydrophone are comparable. With increasing DC bias voltage, the center frequency of the CMUT decreases, whereas the bandwidth did not change remarkably for the used design.

To reduce the expense for the acoustic characterization, electrical impedance measurements have been used. For extracting mechanical and acoustic parameters out of the resulting impedance curve, a novel nonlinear analytic model was developed. This approach advances the linear Butterworth-van-Dyke equivalent circuit representation, as it allows a real physical representation of the CMUT cell. The performance evaluation of different CMUT designs based on the gain-bandwidth product showed, that the efficiency of a CMUT (in air) increases with decreasing plate thickness.

7.1.3 End-of-Line Quality Assurance

In a mass production environment, the end-of-line quality assurance is necessary to evaluate CMUTs prior delivery and to monitor the fabrication process. An impedance measurement procedure was presented to access the characteristics of CMUTs on wafer level. However, the extraction of lumped parameters from the measured impedance curve did not result in a reliable quality indicator. Therefore, a novel methodology based on a coherence criterion was derived. It allows to access the quality of single array elements, single sensor chips and full wafers of MEMS device arrays.

7.2 Outlook

Based on the result of this work, solutions for critical steps in the current production process of CMUTs are achieved. However, the implementation of the presented methodologies and models in a generic product development process chain is still an issue. The results of this work may, also be used to further improve the design, fabrication and test of CMUTs.

The hybrid simulation model developed in this work is evaluated for the acoustic characterization and optimization of individual CMUT cells. The model is capable to be expanded to multiple cells operating in parallel and to include the corresponding sound field simulation. However, the efficiency and low computing time has to be preserved for running optimization loops in an acceptable time. Therefore, also a multistage optimization can be used by first calculating only the cell design and to find the best configuration of multiple cells in an array in a second step.

The analysis of the send- and receive characteristics of CMUTs indicates a very low send sensitivity, whereas the receive sensitivity is comparable to that one of a hydrophone. To enhance both, the send- and receive sensitivity, the use of mechanically interconnected cells is a promising approach. For that, the hybrid simulation model can be adopted by implementing a second plate coupled to the original CMUT cell. Another possibility is the combination of a piezoelectric transducer and a CMUT transducer element.

Similar to the presented wafer-level impedance test, the measurement of the sound pressure is possible on wafer level using an acoustic tip as shown in section 6.2. Then, the methodologies shown in sections 4.4 and 4.5 can be transferred to this novel characterization device. This overcomes limitations of current CMUT acoustic characterization setups in terms of usability, reproducibility and measurement speed. The combination of both, the electrical impedance check and the acoustic wafer level test offers a full characterization and not only a quality indication.

The wafer level quality test itself can be extended by including process parameters and extract statistical parameters from the impedance curve. Based on signal processing techniques such as neuronal networks, a process monitoring can be implemented and process drifts identified in a very early stage. Also, the information of, for example, the resonance frequency distribution over one wafer can be an indication for the quality of the individual fabrication processes.

CMUTs offer a high acoustic bandwidth and the ability to build multifrequency transducers. This makes CMUTs a promising candidate for acoustic spectroscopy. However, this would require drive- and receive-electronics that can operate in the full desired frequency range (up to 50...$100\,\mathrm{MHz}$).

Bibliography

[Agi09] Agilent-Technologies. *Agilent Impedance Measurement Handbook - A guide to measurement technology and techniques*. 4th ed. 2009.

[Ahr01] Ahrens, O. “Mikrosystemtechnische Sensoren in Relativ Bewegten Systemen für die Industrielle Anwendung”. PhD thesis. University of Bremen, 2001.

[AKO14] Atalar, A., Köymen, H., and Oğuz, H. K. “Rayleigh-Bloch waves in CMUT arrays”. In: *IEEE Transactions on Ultrasonics, Ferroelectrics and Frequency Control* 61.12 (2014), pp. 2139–2148.

[Ayd+14] Aydogdu, E., Ozgurluk, A., Atalar, A., and Koymen, H. “Parametric Nonlinear Lumped Element Model for Circular CMUTs in Collapsed Mode”. In: *IEEE Transactions on Ultrasonics, Ferroelectrics, and Frequency Control* 61.1 (2014), pp. 173–181.

[Azh10] Azhari, H. *Basics of Biomedical Ultrasound for Engineers*. Hoboken, NJ, USA: John Wiley & Sons, Inc, 2010. ISBN: 9780470561478.

[Bay+01] Bayram, B., Yaralioglu, G. G., Ergun, A. S., and Khuri-Yakub, B. T. “Influence of the Electrode Size and Location on the Performance of a CMUT [US transducer]”. In: *IEEE International Ultrasonics Symposium*. 2001, pp. 949–952.

[Bhu+13] Bhuyan, A., Choe, J. W., Lee, B. C., Wygant, I. O., Nikoozadeh, A., Oralkan, Ö., and Khuri-Yakub, B. T. “Integrated Circuits for Volumetric Ultrasound Imaging with 2-D CMUT Arrays”. In: *IEEE Transactions on Biomedical Circuits and Systems* 7.6 (2013), pp. 796–804.

[CCP03] Caronti, A., Carotenuto, R., and Pappalardo, M. “Electromechanical coupling factor of capacitive micromachined ultrasonic transducers”. In: *The Journal of the Acoustical Society of America* 113.1 (2003), p. 279.

[Chr+14] Christiansen, T. L., Rasmussen, M. F., Jensen, J. A., and Thomsen, E. V. “Row-Column Addressed 2-D CMUT Arrays with Integrated Apodization”. In: *IEEE International Ultrasonics Symposium*. 2014, pp. 600–603.

[Chr+15] Christiansen, T. L., Rasmussen, M. F., Bagge, J. P., Moesner, L. N., Jensen, J. A., and Thomsen, E. V. "3-D Imaging Using Row-Column-Addressed Arrays With Integrated Apodization - Part II: Transducer Fabrication and Experimental Results". In: *IEEE Transactions on Ultrasonics, Ferroelectrics, and Frequency Control* 62.5 (2015), pp. 959–971.

[CP23] Constantin, C. and Paul, L. "Production of submarine signals and the location of submarine objects". US1471547 A (US). 1923.

[CTP05] Certon, D., Teston, F., and Patat, F. "A Finite Difference Model For cMUT Devices". In: *IEEE Transactions on Ultrasonics, Ferroelectrics and Frequency Control* 52.12 (2005), pp. 2199–2210.

[Els+15] Elsäßer, L., Friedrichs, M., Klemm, M., and Unamuno, A. "Stress Controlled CMUT Fabrication Based on a CMOS Compatible Sacrificial Release Process". In: *Symposium on Design, Test, Integration and Packaging of MEMS/MOEMS (DTIP)*. 2015, pp. 1–4.

[Far51] Faran, J. J. "Sound Scattering by Solid Cylinders and Spheres". In: *The Journal of the Acoustical Society of America* 23.4 (1951), p. 405.

[FG09] Ferreira, A. J. M and Gladwell, G. M. L. *MATLAB Codes for Finite Element Analysis: Solids and Structures*. Vol. 157. Dordrecht: Springer Netherlands, 2009. ISBN: 978-1-4020-9199-5.

[GG06] Gevatter, H.-J. and Grünhaupt, U. *Handbuch der Mess- und Automatisierungstechnik in der Produktion*. 2nd ed. VDI-book. Berlin, Heidelberg: Springer-Verlag Berlin Heidelberg, 2006. ISBN: 3540348239.

[Gur+14] Gurun, G., Tekes, C., Zahorian, J., Xu, T., Satir, S., Karaman, M., Hasler, J., and Degertekin, F. L. "Single-chip CMUT-on-CMOS front-end system for real-time volumetric IVUS and ICE imaging". In: *IEEE Transactions on Ultrasonics, Ferroelectrics, and Frequency Control* 61.2 (2014), pp. 239–250.

[HH15] Heuer, H. and Herzog, T. "Ultraschallwandler zur Anregung und/oder zur Detektion von Ultraschall unterschiedlicher Frequenzen". Pat. DE102012003495A1, EP2631015A2 (Fraunhofer IKTS). Apr. 2015.

[Hit09] Hitachi, Ltd. *Interim Business Report for the 94th Term 2009.4.1 to 2009.9.30*. Ed. by Hitachi Medical Corporation. https://www.hitachi-medical.co.jp/english/ir/pdf/e-ir_94middle.pdf. Accessed: 06. Aug 2015. 2009.

[Hit13] Hitachi Medical Systems America. *US-Preirus Price List 5.13*. https://www.hitachi-medical.co.jp/english/ir/pdf/e-ir_94middle.pdf. Accessed: 23. Mar 2016. 2013.

[HK94] Haller and Khuri-Yakub. “A Surface Micromachined Electrostatic Ultrasonic Air Transducer”. In: *IEEE International Ultrasonics Symposium*. 1994, 1241–1244 vol.2.

[HK96] Haller, M. I. and Khuri Yakub, B. T. “A Surface Micromachined Electrostatic Ultrasonic Air Transducer”. In: *IEEE Transactions on Ultrasonics, Ferroelectrics, and Frequency Control* 43.1 (1996), pp. 1–6.

[Hof+13] Hoffmann, M., Unger, A., Ho, M.-C., Kwan Kyu Park, Khuri-Yakub, B. T., and Kupnik, M. “Volumetric Characterization of Ultrasonic Transducers for Gas Flow Metering”. In: *IEEE International Ultrasonics Symposium*. 2013, pp. 1315–1318.

[Kim+12] Kim, B.-H., Kim, Y., Lee, S., Cho, K., and Song, J. “Design and Test of a Fully Controllable 64×128 2-D CMUT Array Integrated with Reconfigurable Frontend ASICs for Volumetric Ultrasound Imaging”. In: *IEEE International Ultrasonics Symposium*. 2012, pp. 77–80.

[Kle+15a] Klemm, M., Unamuno, A., Elsäßer, L., and Jeroch, W. “Performance Assessment of CMUT Arrays Based on Electrical Impedance Test Results”. In: *Journal of Microelectromechanical Systems* 24.6 (2015), pp. 1848–1855.

[Kle+15b] Klemm[a], M., Kupnik[b], M., Elsäßer[a], L., Unamuno[a], A., and Unger[b], A. “Schallwandlerarray mit gekoppelten Wandlern”. German patent request 102015212153.4 ([a]Fraunhofer IPMS , [b]BTU Cottbus-Senftenberg,). June 2015.

[Köy+07] Köymen, H., Senlik, M. N., Atalar, A., Aydoğdu, e., and Olçum, S. “Parametric Linear Modeling of Circular cMUT Membranes in Vacuum”. In: *IEEE Transactions on Ultrasonics, Ferroelectrics and Frequency Control* 54.6 (2007), pp. 1229–1239.

[Köy+12] Köymen, H., Atalar, A., Aydoğdu, E., Kocabaş, C., Oğuz, H. K., Olçum, S., Ozgurluk, A., and Unlügedik, A. “An Improved Lumped Element Nonlinear Circuit Model for a Circular CMUT Cell”. In: *IEEE Transactions on Ultrasonics, Ferroelectrics and Frequency Control* 59.8 (2012), pp. 1791–1799.

[KU14] Klemm, M. and Unamuno, A. “Simulation Model for CMUT with Rapid Structure Fluid Interaction in Time Domain”. In: *IEEE International Ultrasonics Symposium*. IEEE, 2014, pp. 293–296. ISBN: 978-1-4799-7049-0.

[KU15] Klemm, M. and Unamuno, A. “Vorrichtung, Verfahren und System zum Prüfen eines Schallwandlers”. German patent request 102015206225.2 (Fraunhofer IPMS). Apr. 2015.

[Lei+14] Lei, A., Diederichsen, S. E., La Cour, M. F., Stuart, M. B., Christiansen, T. L., Jensen, J. A., and Thomsen, E. V. “Dimensional Scaling for Optimized CMUT Operations”. In: *IEEE International Ultrasonics Symposium*. 2014, pp. 2595–2598.

[Lei69] Leissa, A. W. *Vibration of plates*. Woodbury, New York: Acoustical Society of America, 1969. ISBN: 1-56396-294-2.

[Lei73] Leissa, A. W. “The free vibration of rectangular plates”. In: *Journal of Sound and Vibration* 31.3 (1973), pp. 257–293.

[Loh05] Lohfink, A. *Untersuchung und Optimierung der Akustischen Eigenschaften Kapazitiver Mikromechanischer Ultraschallwandler am Beispiel der Medizinischen Diagnostik*. Berlin: Logos-Verlag, 2005. ISBN: 3-8325-1064-8.

[Mas15] Masaya Watanabe. *Presentation: Healthcare Business Strategy*. http://www.hitachi.com/IR-e/library/presentation/streaming/150611e-HC.html. Accessed: 06. Aug 2015. Hitachi Ltd. Hitachi IR Day 2015, 11. Jun 2015.

[Mas58] Mason, W. P. *Electromechanical Transducers and Wave Filters*. 2. The Bell Telephone Laboratories series. Princeton, NJ: Van Nostrand, 1958.

[Mös07] Möser, M. *Technische Akustik*. 7th ed. VDI-Buch. Berlin and Heidelberg: Springer, 2007. ISBN: 3-540-71386-7.

[Olc+07] Olcum, S., Atalar, A., Koymen, H., Oguz, K., and Senlik, M. N. “P4M-3 Experimental Characterization of Capacitive Micromachined Ultrasonic Transducers”. In: *IEEE International Ultrasonics Symposium*. 2007, pp. 2131–2134.

[Olc+10] Olcum, S., Yamaner, F. Y., Bozkurt, A., Koymen, H., and Atalar, A. “An Equivalent Circuit for Collapse Operation Mode of CMUTs”. In: *IEEE International Ultrasonics Symposium*. 2010, pp. 443–446.

[Oña13] Oñate, E. *Structural Analysis with the Finite Element Method Linear Statics: Volume 2. Beams, Plates and Shells*. Lecture Notes on Numerical Methods in Engineering and Sciences. Dordrecht: Springer Netherlands, 2013. ISBN: 1402087438.

[Par+11] Park, K. K., Lee, H., Kupnik, M., Oralkan, Ö., Ramseyer, J.-P., Lang, H. P., Hegner, M., Gerber, C., and Khuri-Yakub, B. T. “Capacitive Micromachined Ultrasonic Transducer (CMUT) as a Chemical Sensor for DMMP Detection”. In: *Sensors and Actuators B: Chemical* 160.1 (2011), pp. 1120–1127.

[Plo06] Ploytec GmbH. *Semiautomatic MEMS Test: Application Note VIB-M-04*. Ed. by Ploytec GmbH. 2006.

[Ras+15] Rasmussen, M. F., Christiansen, T. L., Thomsen, E. V., and Jensen, J. A. "3-D Imaging Using Row-Column-Addressed Arrays With Integrated Apodization - Part I: Apodization Design and Line Element Beamforming". In: *IEEE Transactions on Ultrasonics, Ferroelectrics, and Frequency Control* 62.5 (2015), pp. 947–958.

[Rhy78] Rhyne, T. L. "An Improved Interpretation of Mason's Model for Piezoelectric Plate Transducers". In: *IEEE Transactions on Sonics and Ultrasonics* 25.2 (1978), pp. 98–103.

[Ric08] Richter, A. "Ultraschalldämpfungsspektroskopie grobdisperser Systeme". PhD thesis. Dresden, Technical University, Faculty Of Mechanical Science and Engineering, 2008.

[Roy+83] Royer, M., Holmen, J. O., Wurm, M. A., Aadland, O. S., and Glenn, M. "ZnO on Si Integrated Acoustic Sensor". In: *Sensors and Actuators* 4 (1983), pp. 357–362.

[Sav+15] Savoia, A., Mazzanti, A., Sautto, M., and Quaglia, F. "Second - Harmonic Reduction in CMUTs Using Unipolar Pulsers". In: *IEEE International Ultrasonics Symposium*. Vol. 62. 2015, pp. 1–4.

[SD14] Satir, S. and Degertekin, F. L. "A Computationally Efficient Nonlinear System Model for CMUT Arrays". In: *IEEE International Ultrasonics Symposium*. 2014, pp. 313–316.

[Sen+09] Senegond, N., Certon, D., Bernard, J.-E., and Teston, F. "Characterization of cMUT by Dynamic Holography Microscopy". In: *IEEE International Ultrasonics Symposium*. 2009, pp. 2205–2208.

[SZD13] Satir, S., Zahorian, J., and Degertekin, F. L. "A Large-Signal Model for CMUT Arrays with Arbitrary Membrane Geometry Operating in Non-Collapsed Mode". In: *IEEE Transactions on Ultrasonics, Ferroelectrics and Frequency Control* 60.11 (2013), pp. 2426–2439.

[Tes+06] Teston, F., Meynier, C., Jeanne, E., Felix, N., and Certon, D. "P2P-8 Characterization Standard of CMUT Devices Based on Electrical Impedance Measurements". In: *IEEE International Ultrasonics Symposium*. 2006, pp. 1963–1966.

[VK01] Ventsel, E. and Krauthammer, T. *Thin Plates and Shells: Theory, Analysis, and Applications*. New York: Marcel Dekker, 2001. ISBN: 0-8247-0575-0.

[WKK08] Wygant, I. O., Kupnik, M., and Khuri Yakub, B. T. "Analytically Calculating Membrane Displacement and the Equivalent Circuit Model of a Circular CMUT Cell". In: *IEEE International Ultrasonics Symposium*. 2008, pp. 2111–2114. ISBN: 978-1-4244-2428-3.

[WSC15] Wang, X., Su, M. X., and Cai, X. S. “Effects of Material Viscosity on Particle Sizing by Ultrasonic Attenuation Spectroscopy”. In: *Procedia Engineering* 102 (2015), pp. 256–264.

[Yar+03] Yaralioglu, G. G., Ergun, A. S., Bayram, B., Haeggstrom, E., and Khuri Yakub, “Calculation and measurement of electromechanical coupling coefficient of capacitive micromachined ultrasonic transducers”. In: *IEEE Transactions on Ultrasonics, Ferroelectrics and Frequency Control* 50.4 (2003), pp. 449–456.

[Yon+03] Yongli, H., Ergun, A. S., Haggstrom, E., Badi, M. H., and Khuri-Yakub, B. T. “Fabricating Capacitive Micromachined Ultrasonic Transducers with Wafer-Bonding technology”. In: *Journal of Microelectromechanical Systems* 12.2 (2003), pp. 128–137.

[Yon+07] Yoneda, A., Aizawa, Y., Rahman, M. M., and Sakai, S. “High Frequency Resonant Ultrasound Spectroscopy to 50 MHz: Experimental Developments and Analytical Refinement”. In: *Japanese Journal of Applied Physics* 46.12 (2007), pp. 7898–7903.

Appendix A:

CMUT Simulation

Table A.1: Material constants used for simulation

MATERIAL	PARAMETER	VALUE
TiAl	Young's modulus	$E = 112\,\mathrm{GPa}$
	Mass density	$\varrho = 3700\,\mathrm{kg/m^3}$
	Poisson's ratio	$\nu = 0.25$
Al_2O_3	Young's modulus	$E = 295\,\mathrm{GPa}$
	Mass density	$\varrho = 3000\,\mathrm{kg/m^3}$
	Poisson's ratio	$\nu = 0.25$
	Relative permittivity	$\varepsilon_r = 9.3$
SiO_2	Relative permittivity	$\varepsilon_r = 4.0$
H_2O	Mass density	$\varrho = 1000\,\mathrm{kg/m^3}$
	Speed of sound	$c = 1480\,\mathrm{m/s}$
	Sound damping coefficient	$d = 0.002\,\mathrm{dB/(MHz\,cm)}$
Air	Mass density	$\varrho = 1.2\,\mathrm{kg/m^3}$
	Speed of sound	$c = 343\,\mathrm{m/s}$

The following listing shows the Matlab implementation of the differential equation for the hybrid CMUT simulation model as described in section 3.1.3

```matlab
function [wdot,wddot,dp]=OdeFunction(dt,Ap,w,wdot,p,U,ForceFunction,
  M,D,K,c,rho,fixedDOF)

% calculate force vector from surface pressure and applied voltage
% depending on recent plate deflection.
F=ForceFunction(U,w,p);

% solve equation of movement
BF= K*w+D*wdot;
wddot=diag(M).\(F-BF);
wddot(fixedDOF)=0;

% integration for Runge Kutta
wdot=wdot+wddot*dt;

% calculate change of surface sound pressure
dp=Ap.*rho*c.*wddot(1:3:end)*dt;
% sign changed due to coordinate system conventions
% wddot(1:3:end) -> only surface-normal component
end
```

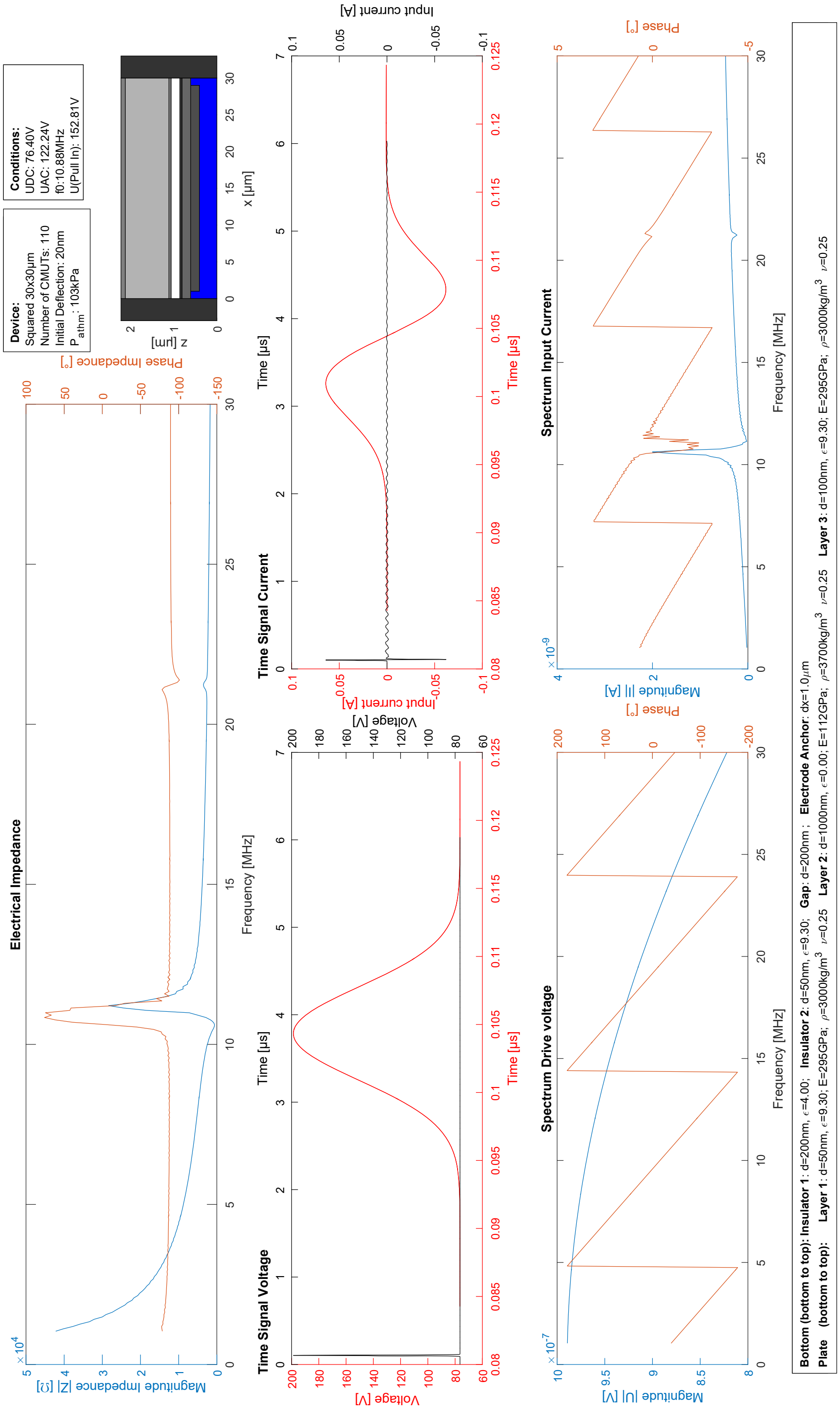

Device:
Squared 30x30µm
Number of CMUTs: 110
Initial Deflection: 20nm
P_{athm}: 103kPa

Conditions:
UDC: 76.40V
UAC: 122.24V
f0:10.88MHz
U(Pull In): 152.81V

Bottom (bottom to top): Insulator 1: d=200nm, ϵ=4.00;   **Insulator 2**: d=50nm, ϵ=9.30;   **Gap**: d=200nm ;   **Electrode Anchor**: dx=1.0μm
Plate   (bottom to top):   **Layer 1**: d=50nm, ϵ=9.30; E=295GPa; ρ=3000kg/m^3 ν=0.25   **Layer 2**: d=1000nm, ϵ=0.00; E=112GPa; ρ=3700kg/m^3 ν=0.25   **Layer 3**: d=100nm, ϵ=9.30; E=295GPa; ρ=3000kg/m^3 ν=0.25

Figure A.1: Simulation result (screenshot of the impedance analysis algorithm) calculated by the hybrid simulation model (see figure 5.3)

Table A.2: Designs variants of CMUTs used for the comparison of resonance frequencies between measurement and simulation for the hybrid CMUT model. (figure 3.20).

Design	CMUT	Measurement	Simulation		Parameters	
Nr.	Shape	$f_{0,air}$	$f_{0,air}$	f_0	U_{DC} [V]	w_0 [nm]
1	50 µm □	5.6 ± 0.1	4.8	7.5	40	30
1	40 µm □	7.8 ± 0.1	7.7	11.7	40	17
1	30 µm □	13.4 ± 0.3	13.5	20.7	40	9
2	50 µm □	6.8 ± 0.2	6.8	10.1	40	13
2	40 µm □	10.3 ± 0.2	10.4	15.6	40	8
2	30 µm □	16.9 ± 0.7	18.0	27.4	40	5
3	50 µm □	6.5 ± 0.1	5.7	8.8	10	20
3	40 µm □	10.1 ± 0.4	9.11	13.7	20	15
3	30 µm □	16.1 ± 0.6	15.9	24	40	10
3	20 µm □	31.2 ± 0.6	34.6	52	40	4
3	20 µm ○	38.6 ± 0.6	42.8	63.8	40	4

Designs:

1: $d_{out,Al_2O_3} = 100\,\mathrm{nm}$, $d_{core,TiAl} = 1\,\mu\mathrm{m}$, $d_{in,Al_2O_3} = 50\,\mathrm{nm}$, $d_{gap} = 200\,\mathrm{nm}$
2: $d_{out,Al_2O_3} = 100\,\mathrm{nm}$, $d_{core,TiAl} = 1.5\,\mu\mathrm{m}$, $d_{in,Al_2O_3} = 50\,\mathrm{nm}$, $d_{gap} = 200\,\mathrm{nm}$
3: $d_{out,Al_2O_3} = 50\,\mathrm{nm}$, $d_{core,TiAl} = 1.5\,\mu\mathrm{m}$, $d_{in,Al_2O_3} = 25\,\mathrm{nm}$, $d_{gap} = 100\,\mathrm{nm}$

Table A.3: Parameter set for optimization of CMUT design performance section 3.4

DESIGN PARAMETER TO OPTIMIZE (GENES)		RANGE
Plate dimension	d_a	15 µm - 40 µm
Plate core thickness	$d_{core,TiAl}$	0.2 µm - 2.0 µm
Gap height	d_g	20 nm - 300 nm

DESIGN PARAMETER (CONSTANT)		VALUE
Plate shape	-	squared
Plate material	-	Al_2O_3 / TiAl / Al_2O_3
Al_2O_3 inside	d_{in,Al_2O_3}	50 nm
Al_2O_3 outside	d_{out,Al_2O_3}	100 nm
Insulation layer	d_{SiO_2}	200 nm
Tensile in-plane stress	σ_T	250 MPa

OPERATION CONDITIONS		VALUE
Atmospheric pressure	p_0	103 kPa
Surrounding fluid	-	Water
Bias voltage	U_{DC}	$\min\{0.7 \cdot U_{DC};100\,\mathrm{V}\}$
AC voltage pulse-Shape	-	Rectangular
AC voltage amplitude	U_{AC}	$\min\{0.6 \cdot U_{DC};30\,\mathrm{V}\}$
AC voltage rise/fall time	$t_r = t_f$	1 ns
AC voltage pulse width	t_{PW}	8 ns
Receive sound pressure pulse-shape	-	Gaussian
Receive sound pressure wave-shape	-	Plane wave
Receive sound pressure amplitude	p_{rec}	100 kPa
Receive sound pressure pulse width	t_{PW}	20 ns

HARD FITNESS INDICATORS		RANGE
Center frequency	f_m	5 MHz-20 MHz
Pull-in voltage	U_{PI}	40 V - 500 V
Send-Receive-Sensitivity	H_{sr}	$\frac{\mathrm{d}^2}{\mathrm{d}f^2}\lvert H_{s,r}(f_{O1} \leq f \leq f_{O2})\rvert \leq 0$

SOFT FITNESS INDICATORS		VALUE
Send-Receive sensitivity	FI_1	$\min\left\{\frac{\lvert\underline{I}_r(f_{O1})\rvert}{1}, \frac{\lvert\underline{I}_r(f_{O2})\rvert}{4}\right\}$
CMUT cell area	FI_2	$(d_a+2\,\mu\mathrm{m})^{-2}$
Total Fitness	FI	$FI_1 \cdot FI_2$

Appendix B:

CMUT Device Characterization

B.1 Acoustic Measurements in Immersion

Table B.1: Setup components for acoustic measurements of packaged CMUTs (chapter 4)

FUNCTION	MANUFACTURER, DEVICE	SERIAL NUMBER
Oscilloscope	LeCroy WaveRunner Zi66	LCRY3106N59433
DC Source	Keithley K236	549848
DC Source	Keithley K236	515837
Power Amplifier	E&I 325LA	245
Receive Amplifier	Cividec C1[1]	C2HV0132
Signal Generator	Agilent 33250A	MY40030014
Translation Stage	Physik Instrumente	Type PI M-403.8DG
Hydrophone Preamplifier	Precision Acoustics	PA13058
Hydrophone DC Coupler	Precision Acoustics	DCPS358
Hydrophone Needle	Precision Acoustics $0.50\,\mathrm{mm}$	2208

---

[1] Customized version with frequency range from $35\,\mathrm{kHz}$ to $2\,\mathrm{GHz}$.

Table B.2: Characteristics of rectangular pulse shape used for CMUT transmit characterization

SIGNAL GENERATOR				POWER AMPLIFIER			
U_{max} [mV]	t_{PW} [ns]	t_r [ns]	t_f [ns]	U_{max} [V]	t_{PW} [ns]	t_r [ns]	t_f [ns]
203.0	28.3	12.8	18.9	-110.2	30.4	21.8	19.4
169.6	28.3	12.9	18.9	-94.9	30.4	21.5	19.0
140.0	28.2	12.8	18.7	-79.4	30.5	21.7	18.5
110.9	28.3	12.8	18.8	-63.4	30.5	21.3	18.1
82.0	28.2	12.8	18.8	-47.5	30.4	21.2	18.0
54.7	28.2	12.9	18.9	-31.7	30.4	21.3	17.9
27.7	28.2	12.8	18.6	-16.0	30.4	21.4	18.0
-32.5	28.4	12.7	18.7	16.7	32.4	21.9	21.6
-64.5	28.4	12.8	18.7	33.1	32.2	21.7	21.3
-97.9	28.5	12.8	18.4	49.8	32.2	21.9	21.3
-134.5	28.4	12.9	18.7	66.7	32.5	21.9	21.3
-172.9	28.5	12.9	18.6	83.2	32.6	22.0	21.7
-218.1	28.5	12.9	18.6	99.6	32.7	22.6	21.2
-285.5	28.5	12.9	18.7	115.8	33.1	22.8	21.2

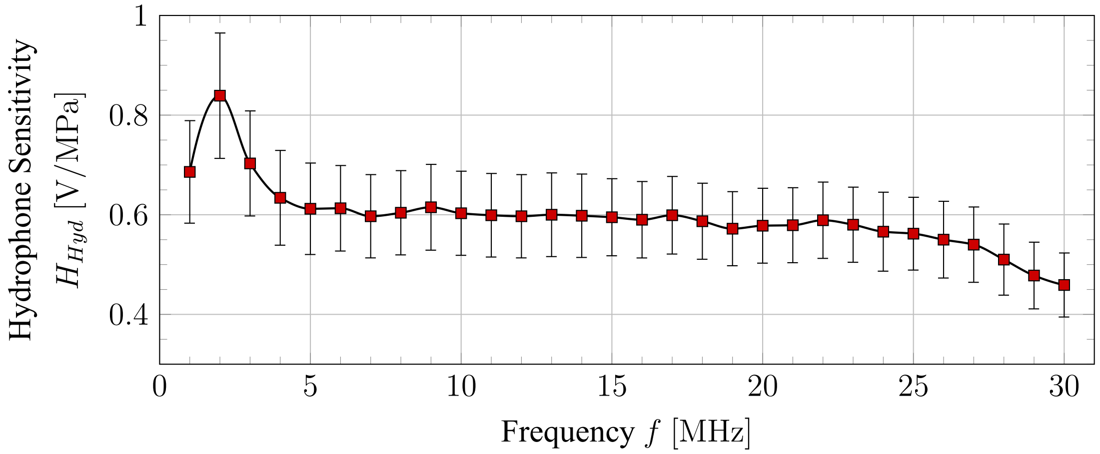

Figure B.1: Hydrophone sensitivity $U_{Hyd}(f)$ according to calibration sheet (marks), calibration uncertainty (2σ) and cubic interpolation (line).

Table B.3: CMUT design parameters for static deflection simulation (section a))

DESIGN PARAMETER		DESIGN #1	DESIGN #2
Plate dimension	d_a	40 µm	40 µm
Plate shape	-	squared	squared
Al_2O_3 inside	d_{in,Al_2O_3}	50 nm	50 nm
TiAl plate	$d_{core,TiAl}$	0.5 µm	1.5 µm
Al_2O_3 outside	d_{out,Al_2O_3}	100 nm	100 nm
Gap height	d_g	-	200 nm
Insulation layer	d_{SiO_2}	-	200 nm
Atmospheric pressure	p_0	103 kPa	103 kPa

Table B.4: CMUT Design for experimental acoustic characterization (see chapter 4)

DESIGN PARAMETER		DESIGN
Plate dimension	d_a	30 µm
Plate shape	-	squared
Al_2O_3 inside	d_{in,Al_2O_3}	50 nm
TiAl plate	$d_{core,TiAl}$	1.5 µm
Al_2O_3 outside	d_{out,Al_2O_3}	100 nm
Gap height	d_g	200 nm
Insulation layer	d_{SiO_2}	200 nm

B.2 Impedance Measurements on CMUT

Table B.5: Components of setup for impedance measurement of packaged CMUTs

FUNCTION	DEVICE	SERIAL NUMBER
Impedance Analyzer	Wayne Kerr 65120B	1497790
DC Source	Keithley 2400	4015500
Bias Tee	Self-built [Agi09, Figure 5-46]	

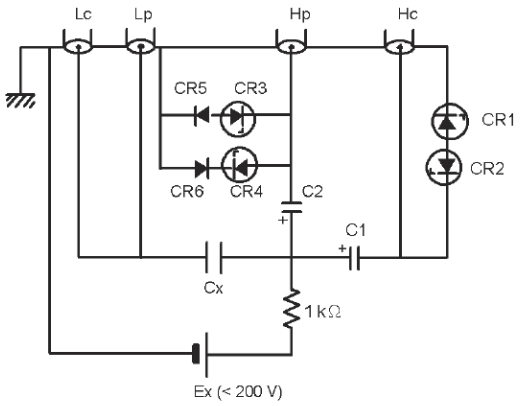

where Cx: Sample capacitor
Ex: External DC bias voltage source
C1: Blocking capacitor
Capacitance value ≥ $\frac{1}{10\pi f}$
(f: measurement frequency (Hz))
DC withstand voltage: > Ex
C2: Blocking capacitor
Capacitance value: 1 μF
DC withstand voltage: Ex

CR1, CR2: Diode-zener, 47 V, 5% 1 W
CR3, CR4: Diode-zener, 3.3 V, 5% 1 W
CR5, CR6: Diode-power, 200 V, 1 A

Figure B.2: Bias tee for impedance measurements as shown in [Agi09, Figure 5-46]

Table B.6: CMUT design for analysis of the analytical impedance model (see section 5.2)

DESIGN PARAMETER		DESIGN #1	DESIGN #2	DESIGN #3
Plate dimension	d_a	40 µm	50 µm	40 µm
Plate shape	-	squared	squared	squared
Al_2O_3 inside	d_{in,Al_2O_3}	50 nm	50 nm	50 nm
TiAl plate	$d_{core,TiAl}$	1.5 µm	1.5 µm	2.0 µm
Al_2O_3 outside	d_{out,Al_2O_3}	100 nm	100 nm	100 nm
Gap height	d_g	200 nm	200 nm	200 nm
Insulation layer	d_{SiO_2}	200 nm	200 nm	200 nm

Table B.7: Design parameters of a wafer as used in section 5.3.3

Thickness:	TiAl plated$d_{core,TiAl}$	$1\,\mu m$		
	Al_2O_3 inside d_{in,Al_2O_3}	$50\,nm$		
	Al_2O_3 outside d_{out,Al_2O_3}	$100\,nm$		
Design variant	Geometry	Diameter	Resonance frequency	Pull-in voltage
#1	square	$50\,\mu m$	$5.6\,MHz$	$35\,V$
#2	circular	$50\,\mu m$	$6.4\,MHz$	$40\,V$
#3	square	$40\,\mu m$	$7.8\,MHz$	$56\,V$
#4	circular	$40\,\mu m$	$8.9\,MHz$	$57\,V$
#5	square	$30\,\mu m$	$13.2\,MHz$	$91\,V$
#6	circular	$30\,\mu m$	$15.1\,MHz$	$99\,V$
#7	square	$40\,\mu m$	$7.8\,MHz$	$55\,V$
#8	square	$40\,\mu m$	$7.9\,MHz$	$54\,V$
#9	square	$40\,\mu m$	$7.9\,MHz$	$54\,V$

Appendix C:

Publications

C.1 Scientific Publications

1. **KLEMM, M.**, and UNAMUNO, A.
   “Fast Nonlinear CMUT Simulation Model for Pull-In and Dynamic Fluid Coupled Deflection Analysis”
   In: *13th International Workshop on Micromachined Ultrasonic Transducers (MUT).* Copenhagen, Denmark. 2014

2. UNAMUNO, A., **KLEMM, M.**, and GRÜGER, H.
   “Realization of CMUT based Ultrasonic Sensorsystems”
   In: *Smart Systems Integration (SSI)* Vienna, Austria. 2014, pp. 587–90. ISBN: 978-3-86359-201-1

3. **KLEMM, M.**, and UNAMUNO, A.
   “Simulation Model for CMUT with Rapid Structure Fluid Interaction in Time Domain”
   In: *IEEE International Ultrasonics Symposium.* Chicago, USA. 2014, pp. 293–296, ISSN: 1051-0117

4. ELSÄSSER, L., FRIEDRICHS, M., **KLEMM, M.**, and UNAMUNO, A.
   “Stress Controlled CMUT Fabrication based on a CMOS Compatible Sacrificial Release Process”
   In: *Symposium on Design, Test, Integration and Packaging of MEMS/MOEMS (DTIP).* (Montpellier,France). 2015, pp. 1–4, ISBN: 978-1-4799-8627-9

5. **KLEMM, M.** UNAMUNO, A., ELSÄSSER, L., and JEROCH, W.
   "Performance Assessment of CMUT Arrays based on Electrical Impedance Test Results"
   In: *Journal of Microelectromechanical Systems (IEEE)* , vol. 24, no. 6, pp. 1848-1855, Dec. 2015.

6. **KLEMM, M.**, and UNAMUNO, A.
   "Wafer Level Impedance Measurement and Data Analysis for CMUTs"
   In: *14th International Workshop on Micromachined Ultrasonic Transducers (MUT).* Dresden, Germany. 2015

7. **KLEMM, M.**
   "Elektroakustische Modellierung von CMUT basierend auf Netzwerkmodellen und Finite-Elemente-Methoden"
   In: *Nichtelektrische Netzwerke: Wie die Systemtheorie hilft, die Welt zu verstehen.* Dresdner Beiträge zur Sensorik. vol. 60. TUD-press, 2015, pp. 199–209. ISBN : 978-3-95908-025-5

8. AMELUNG, J. **KLEMM, M.**, ELSÄSSER, L., KIRCHER, M., et al.
   "Back-End-Of-Line Integration Technology of Capacitive Micromachined Ultrasonic Transducers (CMUT)"
   In: *Smart Systems Integration (SSI).* Munich, Germany. 2016, ISBN : 978- 3-95735-040-4

C.2 Patent Applications

1. **KLEMM, M.**, KUPNIK, M., UNAMUNO, A., and UNGER, A.
   “Schallwandlerarray mit gekoppelten Wandlern”
   International Patent Request PCT/EP2016/055091, March 2016
   German Patent Request 10 2015 204 583.8, March 2015

2. **KLEMM, M.**, and UNAMUNO, A.
   “Vorrichtung, Verfahren und System zum Prüfen eines Schallwandlers”
   German Patent Request 102015206225.2, April 2015

3. **KLEMM, M.**, and UNAMUNO, A.
   “Akustische Wandlervorrichtung mit einem Piezo-Schallwandler und einem MUT-Schallwandler, Verfahren zum Betrieb derselben, akustisches System, akustische Koppelstruktur und Verfahren zum Herstellen einer akustischen Koppelstruktur”
   International Patent Request PCT/EP2016/061296, May 2016
   German Patent Request 10 2015 209 485.5, May 2015

4. **KLEMM, M.**, and UNAMUNO, A.
   “Druckvorrichtung zum Drucken einer dreidimensionalen Struktur”
   German Patent Request 10 2015 212 153.4, June 2015

DRESDNER BEITRÄGE ZUR SENSORIK BAND **66**

Ultrasonic transducers are used in many fields of daily life, e.g. as parking aids or medical devices. To enable their usage also for mass applications small and low-cost transducers with high performance are required. Capacitive, micromachined ultrasonic transducers (CMUT) offer the potential, for instance, to integrate compact ultrasonic sensor systems into mobile phones or as disposable transducer for diverse medical applications.

This work is aimed at providing fundamentals for the future commercialization of CMUTs. It introduces novel methods for the acoustic simulation and characterization of CMUTs, which are still critical steps in the product development process. They allow an easy CMUT cell design for given application requirements. Based on a novel electromechanical model for CMUT elements, the device properties can be determined by impedance measurement already. Finally, an end-of-line test based on the electrical impedance of CMUTs demonstrates their potential for efficient mass production.

TUDpress

9 783959 081009